PLASMA-ENHANCED ATOMIC LAYER DEPOSITION OF BORON CARBIDE FOR INTERCONNECT APPLICATIONS

A THESIS IN

Physics

Presented to the Faculty of the University
of Missouri-Kansas City in partial fulfillment of
the requirements for the degree

MASTER OF SCIENCE

By

LAUREN MIKAL DORSETT

B.A., Austin College, 2012

Kansas City, Missouri
2018

© 2018

LAUREN MIKAL DORSETT

ALL RIGHTS RESERVED

AN ABSTRACT IN PLASMA-ENHANCED ATOMIC

LAYER DEPOSITION OF BORON CARBIDE FOR

INTERCONNECT APPLICATIONS

Lauren Mikal Dorsett, Candidate for the Master of Science Degree

University of Missouri-Kansas City, 2018

ABSTRACT

As the semiconductor industry endeavors to scale integrated circuit dimensions—decreasing layer thicknesses while increasing the aspect ratio of fillable features—the need for novel interconnect materials with highly specialized properties continues to rise. Meeting the requirements for the numerous types of materials needed, including low-k dielectrics, etch stops, metal diffusion barriers, hardmasks, spacer layers, and other pattern-assist layers, with traditional silicon-based materials is becoming increasingly challenging. As an alternative to silicon, amorphous hydrogenated boron carbide (a-BC:H), grown through plasma-enhanced chemical vapor deposition (PECVD), has been demonstrated to possess excellent dielectric properties, combined with very high Young's modulus, electrical properties rivaling those of SiOC:H variants, very good chemical stability, and unique and useful etch chemistry. However, a problem with PECVD growth that will limit its long-term utility is its inability to scale while maintaining uniform, conformal coatings for very thin films.

To combat the issues arising from PECVD grown boron carbide, a plasma-enhanced molecular-layer-deposition-based process for the growth of BC films on metal (copper) substrates using solid carborane precursors was proposed. This thesis describes the design and construction of a reactor chamber capable of this hypothesized film growth as well as the characterization of those preliminary depositions. Monolayer carborane growths on copper substrates were demonstrated with characterization including *in situ* spectroscopic ellipsometry, as well as *ex situ* contact angle analysis and X-ray photoelectron spectroscopy. The surface of the monolayer was then plasma treated and preliminary multi-layer growths were tested.

APPROVAL PAGE

The faculty listed below, appointed by the Dean of the College of Arts and Sciences, have examined a thesis titled “Plasma-Enhanced Atomic Layer Deposition of Boron Carbide for Interconnect Applications,” presented by Lauren Mikal Dorsett, candidate for the Master of Science degree, and certify that in their opinion it is worthy of acceptance.

Supervisory Committee

Michelle M. Paquette, Ph.D., Committee Chair
Department of Physics and Astronomy

Anthony N. Caruso, Ph.D.
Department of Physics and Astronomy

Paul Rulis, Ph.D.
Department of Physics and Astronomy

CONTENTS

ABSTRACT iii

ILLUSTRATIONS viii

TABLES xiii

ABBREVIATIONS xiv

CHAPTER

1 BACKGROUND 1

1.1 Goals of Thesis 1

1.2 Semiconductor Trends 1

1.2.1 Moore's Law 1

1.2.2 Interconnect Challenges 2

1.2.3 Patterning Requirements 7

1.3 Boron Carbide 9

1.4 Need for ALD 12

1.4.1 PVD, CVD and PECVD 12

1.4.2 What is ALD? 14

1.4.3 What is MLD? 16

1.4.4 What is PEALD? 18

1.4.5 ALD of BC 22

1.5 Thesis Roadmap 24

2 EXPERIMENTAL 25

2.1 Reactor Design 25

2.1.1 General Overview 25
2.1.2 Substrate Holder/Heater 27
2.1.3 Sample Transfer 28
2.1.4 Flow Design and Control 29
2.1.5 Plasma Generation 35
2.1.6 Heating 36
2.1.7 Film Characterization 41
3 RESULTS & DISCUSSION 47
3.1 Introduction 47
3.2 Experimental Details 49
3.2.1 Substrate Preparation 49
3.1.2 Chamber Preparation 50
3.2 Self-Assembled Monolayer Growth 51
3.2.1 9-Thiol-m-carborane on Copper 51
3.2.2 1,2-Dithiol-o-carborane on Copper 54
3.3 SAM and Plasma 59
3.4 Multi-layer PEMLD 63
3.5 Multi-layer, Multi-cycle PEMLD 67
4 CONCLUSION AND FUTURE WORK 74
REFERENCES 77
VITA 93

ILLUSTRATIONS

Figure Page

1. MLI system with metal/dielectric diffusion barriers, etch stop, metal conductor, and insulating dielectric interlayer. 2

2. Diagram showing the metal and insulating layers contributing to the RC delay. 3

3. During the copper dual damascene interconnect fabrication process, the via patterning (a), via and trench patterning (b), barrier layer deposition (c), copper deposition with chemical/mechanical removal of excess material (d), and capping layer deposition (e) are used to make an interconnect. 5

4. Stages of self-aligned quadruple patterning. From left to right: patterning of the first core (pink) on mandrel (teal); SiO_2 deposition (blue); etching of first spacers; etching of mandrel to produce second core (purple); second SiO_2 deposition; etching of the second spacers and second core layer. 8

5. PVD step coverage (a) compared with the ideal conformal step coverage from CVD (b). 13

6. ALD process flow. 15

7. Illustration of properties of ALD. 15

8. ALD window depicting the dependence of growth rate on deposition temperature. 16

9. (a) ALD vs (b) MLD self-limiting reactions and growth 17

10. (a) Two-dimensional MLD linear chains. (b) Types of growth defects that cause lowered growth rates in organic and inorganic–organic films. (c) Three-dimensional MLD structure. 18

11. Difference in (a) ALD and (b) PEALD growth 19

12. Various PEALD reactor configurations: (a) radical-enhanced ALD, (b) direct plasma-enhanced ALD, (c) remote plasma ALD, and (d) direct plasma reactor with mesh. 20

13. (a) Icosahedral geometry of BC and (b) scanning tunneling microscope images of thiol-carborane SAM.. 23

14. Top-down view of PEMLD chamber with XPS and evaporation chamber configuration. The evaporation chamber has a 6″ door on the top for loading samples........ 26

15. Reactor schematic showing major components (note: not all components are shown). 26

16. Top and side view of the substrate holder/heater with sample puck design and dimensions. 27

17. Top-down view of the sample puck transfer between the PEMLD transfer arm fork (left) and evaporation/load-lock/XPS transfer arm fork (right). 28

18. The PEMLD transfer arm picking up the sample puck from the substrate heater/holder and transferring to the load-lock chamber. 29

19. Swagelok two-way ALD diaphragm valve with flow design (a) and actual Swagelok two-way ALD valve (b). 30

20. Precursor, plasma, and purge gas delivery........ 31

21. (a) The top flange of the chamber shown as a whole, (b) cross-sectional view of the showerhead, (c) top and bottom view of the showerhead. 32

22. (a) Starting configuration and (b) final configuration for pressure and leak testing of the chamber. 34

23. (a) Capacitively coupled plasma configuration, (b) plasma component configuration of home-built reactor. 36
24. Heating zones 1-4. 38
25. Heating zones 5-8. 38
26. Heating zones 9-10. 39
27. Upstream gas line configuration. 39
28. Heating zones 11-14. 40
29. Graphical user interface for PEMLD heating. 41
30. In Situ Ellipsometry Design. 42
31. Ellipsometry design with beam path. 42
32. FS-1 Ellipsometer attached to the chamber ports. 43
33. Surfaces with (a) high and (b) low contact angle. (c) UMKC home-built contact angle system. 46
34. 9-thiol-m-carborane (a) and 1,2-dithiol-o-carborane (b). 47
35. Amide condensation reaction. 48
36. 1-COOH-o-carborane. 48
37. Silicon coupon attached to puck prior to evaporation. 49
38. XPS survey scan of sample A11: 60 s dose of 9-thiol-m-carborane on copper at 0.01 Torr, ambient temperature. 52
39. XPS C 1s spectrum of sample A11: 60 s dose of 9-thiol-m-carborane on copper at 0.01 Torr, substrate temperature-ambient, precursor temperature-175°C. 53
40. Theorized 1,2-dithiol-o-carborane formation of SAM on copper substrate. 55

41. Full process of self-saturative 1,2-dithiol-o-carborane growth on copper substrate. The left y-axis represents the ellipsometry raw S parameter data at the four wavelengths (red, yellow, green and blue), whereas the right represents the modeled thickness (black). The modeled thickness uses a pseudo-copper substrate layer with a Cauchy growth layer. The ampoule was heated to 175 ºC and chamber pressure raised to 0.01 Torr before the ampoule was closed. The total dose time was 60 minutes with the substrate temperature maintained at 125 ºC. 56

42. Rapid growth region of self-saturative 1,2-dithiol-o-carborane on copper substrate. 57

43. XPS characterization data for sample A13: 60 s dose, 0.01 Torr, substrate temperature-ambient, precursor temperature-175 ºC, 1,2-dithiol-o-carborane on copper. 58

44. Contact angle measurements comparing levels of oxidation and SAM growth on copper. 59

45. Hypothesized nitrogen plasma surface modifications of 1,2-dithiol-o-carborane. 60

46. Nitrogen plasma dose on 1,2-dithiol-o-carborane film F000. Plasma conditions: power=50 W, N_2 flow=65 sccm, 1 min dose 61

47. XPS characterization of 1,2-dithiol-o-carborane film with nitrogen plasma treatment, A26. Plasma conditions: power=10 W, N_2 flow=100 sccm, 1 min dose 62

48.(a) Contact angle for pre- and (b) post-plasma 1,2-dithiol-o-carborane film. 63

49. Hypothesized multi-layer growth using 1-COOH-o-carborane on plasma-treated 1,2-dithiol-o-carborane film. 64

50. PEMLD process flow for multi-layer growth F003. 65

51. In situ ellipsometry raw data for multi-layer growth F003.1,2-dithiol-o-carborane dose at 12 min for 1 min at 440 mTorr and precursor temperature-175 ºC, substrate temperature-175°C. Nitrogen plasma dose at 26 min for 1 min at 200 mTorr, 72 sccm and 50 W. 1-COOH-o-carborane dose at 40 min for 1 min at 102 mTorr and precursor temperature-175 ºC. 65

52. XPS characterization of sample F003 which had layers: copper, 1,2-dithiol-o-carborane, nitrogen plasma and 1-COOH-o-carborane. 66

53. Multi-layer, multi-cycle growth of F006. 68

54. Raw in situ ellipsometry data for F006 multi-layer, multi-cycle growth. 70

55. In situ ellipsometry raw data for F006 with wavelengths separated to allow easier viewing.. 71

56. XPS characterization of sample F006 which had layers: copper, 1,2-dithiol-o-carborane and five PEMLD (plasma/1-COOH-o-carborane) cycles performed. . 72

57. F006 sample post-growth showing evident film on substrate. 73

TABLES

Table Page

1. Low-k ILD requirements ... 6

2. Low-k dielectric properties for a-BC:H in comparison with state of the art ILD and DB/ES. ... 11

3. Table relating the beam path length to beam size at the detector and on sample and average intensity.. ... 44

4. Ellipsometric comparison between the FS-1 and J.A. Woollam Alpha-SE. ... 45

5. XPS raw data from survey scans showing binding energy (eV) and atomic percentages (%) of elements. ... 54

6. XPS ratio of elements calculated from atomic percentages. Boron is first set to 10, representing the 10 boron atoms of the icosahedral carborane precursor, then the other element ratios are calculated. C_B is approximated by subtracting the C_H peak area from the total C peak area. ... 54

7. XPS ratio of elements calculated from the atomic percentages for sample A13. ... 58

8. XPS binding energies (eV) and atomic percentages (%) of elements for sample A26. 63

9. XPS binding energy (eV) and atomic percentages (%) of elements for sample F003. 67

10. F006 detailed process flow for multi-layer-multi-cycle growth. ... 69

11. XPS binding energy (eV) and atomic percentages (%) of elements for sample F006. ... 73

ABBREVIATIONS

2-D	two-dimensional
3-D	three-dimensional
a-BC:H	amorphous hydrogenated boron carbide
ALD	atomic layer deposition
AOI	angle of incidence
BC	boron carbide
C	capacitance
CCL	copper capping layer
CCP	capacitively coupled plasma
CTE	coefficient of thermal expansion
CVD	chemical vapor deposition
DB	diffusion barrier
E	Young's modulus
ES	etch stop
GUI	graphical user interface
IC	integrated circuit
ITRS	International Technology Roadmap for Semiconductors
ILD	interlayer dielectric
k	dielectric permittivity constant
L_S	length of interconnect
MFC	mass flow controller
MLD	molecular layer deposition

MLI	multi-level interconnect
ρ	resistivity
PEALD	plasma enhanced atomic layer deposition
PEMLD	plasma enhanced molecular layer deposition
PECVD	plasma enhanced chemical vapor deposition
PID	proportional, integral, derivative
PVD	physical vapor deposition
QCM	quartz crystal microbalance
REALD	radical enhanced atomic layer deposition
R	resistance
RC	resistive-capacitive
RF	radio frequency, 13.56 MHz
SAM	self-assembled monolayer
SCCM	standard cubic centimeters per minute
SE	spectroscopic ellipsometry
SRS-RGA	Stanford Research System - Residual Gas Analyzer
TBV	throttling butterfly valve
TDDB	time-dependent dielectric breakdown
XPS	x-ray photoelectron spectroscopy
VDC	volts direct current

CHAPTER 1

BACKGROUND

1.1 Goals of Thesis

Boron carbide (BC) is a material finding new applications in the world of semiconductor technology due to its electrical, mechanical, thermal, and chemical stability, as well as other useful properties such as diffusion resistance, low dielectric constant, high electrical resistivity, and etch selectivity. The thin-film deposition technique of atomic layer deposition (ALD) is gaining increasing interest for ultrathin films, because it can deposit on demanding surfaces such as high aspect ratio structures and is able to conformally deposit ultrathin films.

In this thesis, the plasma-enhanced atomic layer deposition (PEALD) of BC from carborane precursors is studied. The main focus of this work is the fabrication of a reactor chamber suitable to this process and preliminary findings suggesting BC growth.

1.2 Semiconductor Trends

1.2.1 Moore's Law

In April 1965, Intel co-founder Gordon Moore proposed in *Electronics* magazine that the number of transistors on a square inch of silicon would double approximately every year.[1] Moore's prediction held true through 1975 when he and his colleague David House extended the doubling prediction to 18–24 months.[2] This trend would come to be known as Moore's Law and is used in the semiconductor industry for research and development targets.

1.2.2 Interconnect Challenges

The semiconductor industry has come across many challenges in pacing with Moore's Law, the most obvious of which is caused by scaling and feature crowding: when the minimum feature size of an integrated circuit (IC) decreases, the functional density of the chip increases. Because the IC is made from many junctions called interconnects which only live on the surface of an IC, the area occupied by the interconnection lines extends more rapidly than the area needed to accommodate the active devices. As such when dealing with two-dimensional ICs, the minimum chip area becomes interconnect-limited.[3,4] To aid in these spatial limitations, multi-level interconnect (MLI) systems made from three-dimensional networks of interconnects were developed in the late-eighties/early-nineties. Figure 1 shows an example of an MLI system where the area needed by the interconnect lines is shared among two or more levels.

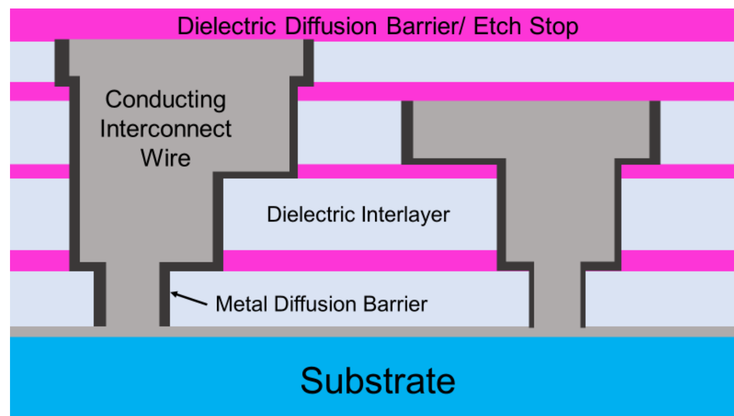

Figure 1. MLI system with metal/dielectric diffusion barriers, etch stop, metal conductor, and insulating dielectric interlayer.

The advancement of MLIs helped allow Moore's Law to continue to predict the capabilities of integrated circuits; however, as the semiconductor industry left micro-electronic technology and entered the nano-scale era, new challenges arising from scaling required major changes in semiconductor fabrication.

In the late-nineties, one of the primary problems in scaling ICs was the physical limitations of the materials being used. With the increased number of transistors in the two-dimensional (2-D) plane, the interconnect length between those transistors' gates was also decreasing. Figure 2 shows how an increase in the length (L_S) of the interconnect increases the resistance (R) as well as the capacitance (C). To get the total resistive-capacitive (RC) time delay within the IC, the total overall length of interconnects is considered. To mitigate the physical limitations, IC were transitioned from 2-D to three-dimensional (3-D) transistor layouts. Although this helped reduced RC time delay, this was only a short-term solution.

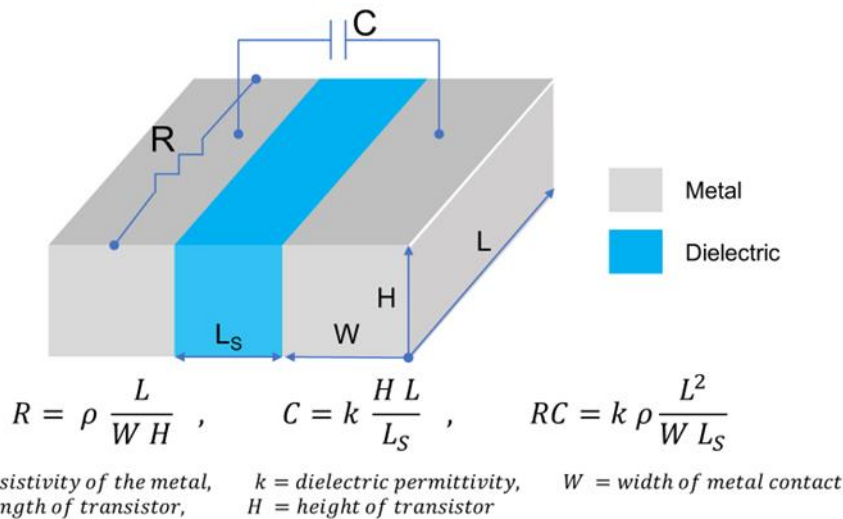

Figure 2. Diagram showing the metal and insulating layers contributing to the RC delay.

Over the past two decades, RC delay reduction necessitated a change in the interconnect materials. First, the traditionally aluminum metal interconnects were replaced by copper. The switch was motivated by the need to lower the resistivity (ρ) of the metal: copper has a resistivity of 1.68×10^{-8} Ω·m compared to aluminum at 2.65×10^{-8} Ω·m.[5] Other attractive properties of copper that led to its selection included its relatively low cost, high availability, electromigration resistance, and higher melting point relative to aluminum.[6] Second, IBM introduced a unique processing technique known as the damascene process. Damascene is an additive process where the dielectric material is first deposited then etched to form vias/trenches according to a defined photoresist pattern. Vias (also known as vertical interconnect accesses) and trenches are used to either connect layers or isolate features from each other depending on the application in the device. A barrier layer is then deposited into the vias/trenches, followed by copper, which is then flattened by chemical mechanical planarization. The dual damascene process, which soon followed, is characterized by patterning the vias and trenches in such a way that the metal deposition fills both at the same time. Figure 3 shows an interconnect created using a copper dual damascene process.

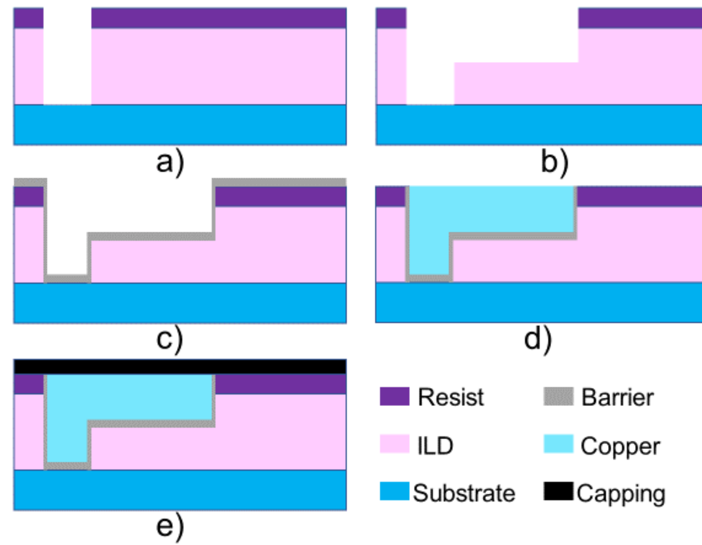

Figure 3. During the copper dual damascene interconnect fabrication process, the via patterning (a), via and trench patterning (b), barrier layer deposition (c), copper deposition with chemical/mechanical removal of excess material (d), and capping layer deposition (e) are used to make an interconnect.

While the change to copper improved the resistance component in the RC delay, a change in the interlayer dielectrics (ILDs) was still needed to improve the capacitance contribution to the problem. To improve the capacitance contribution to the RC delay, ILDs were transitioning from silicon dioxide (SiO_2)-based materials to dielectrics with lower values of dielectric permittivity.[5] Using a simplified approximation, the metal layers act as a parallel plate capacitive structure and by using a dielectric with a lower dielectric constant (*k*) value the effective electric field between the plates is reduced and the DC leakage current through the capacitor is minimized.

1.2.2.1 Low-k ILD Requirement

In principle, the semiconductor industry is having to replace the currently used materials for ILDs with ones that have a lower *k* value to prevent a disruption in the

scaling trend of ICs. There is not only a need for low-*k* ILDs but also more specialized layers compatible with process integration. These low-*k* materials may need to act as a copper capping layer (CCL), diffusion barrier (DB), and/or etch stop (ES) layer. A CCL prevents copper from out-diffusion while the DB prevents the in-diffusion of moisture and other processing reagents. Other ILD properties such as electrical and mechanical stability as well as thermal compatibility are also important while selecting a new interlayer dielectric material.[5–7] Table 1 show some of the low-*k* ILD requirements for successful integration in devices.

Table 1. Low-k ILD requirements. Adapted from Murarka et al 2003.[6]

Electrical	Mechanical	Thermal
Low leakage current	High Young's modulus	Low thermal shrinkage/ expansion
High dielectric breakdown strength	High hardness	High thermal conductivity
High reliability	Low stress	
	Good adhesion	

Electrically, the new low-*k* ILD would require an extremely low leakage current, high dielectric breakdown strength, and resistance to time-dependent dielectric breakdown (TDDB).[8] An ideal dielectric would be a perfect insulator but in reality, every dielectric has finite resistivity. This finite resistivity allows current to pass through the material when subject to an applied voltage. Reducing the leakage current while maintaining high dielectric strength is important for device reliability when the size of the IC is decreasing.

Mechanically, the ILD provides a reinforcing stability to the various metal layers of the MLI and helps to distribute stresses produced during downstream processing and packaging. However because one of the simplest ways to produce a material with a lower dielectric constant is to increase porosity, mechanical properties such as Young's modulus (E) and hardness can be compromised.[9] King states that dielectrics with $E = 5$–10 GPa are already being integrated into high-volume semiconductor manufacturing and this therefore represents a safe lower limit target. [5]

Other mechanical properties that go into the selection of a low-k ILD are its stress and adhesion properties when grown in relation to the metallization layer.[7] If the ILD and substrate have significantly different coefficients of thermal expansion (CTE), thermal stress on the film can cause cracking in the film from tensile stress or buckling from compressive stress. Typically, it is desirable to have a low-k ILD with a CTE close to that of the metal being used. Adhesion is also important in reducing device failure in the MLIs. It is desired for the adhesion value to be above a 5 J/m^2 threshold when tested with a four-point bend test.

1.2.3 Patterning Requirements

Traditional lithography alone cannot keep up with the increased precision needed in the scaling of 3-D chip structures. Although electron beam lithography is under investigation to make smaller feature sizes, currently multiple patterning schemes with predicted etch selectivity are used to halve and quarter those feature sizes. Because traditional lithography relies on the alignment of multiple masks to pattern complex layers, errors occurring from misalignment become more apparent with structure size

ever decreasing. Self-aligned patterning reduces the edge placement error due to the use of a single mask to pattern multiple features. Self-aligned patterning relies on the selectivity of the materials' chemical etching characteristic. Figure 4 shows a sample self-aligned quadruple patterned stack used for creating fins in N7/N5 devices.[10] More easily aligned patterning techniques, that use self-aligned patterning schemes, have become more desirable as 7 nm manufacturing is expected to be in production in the next few years.[11]

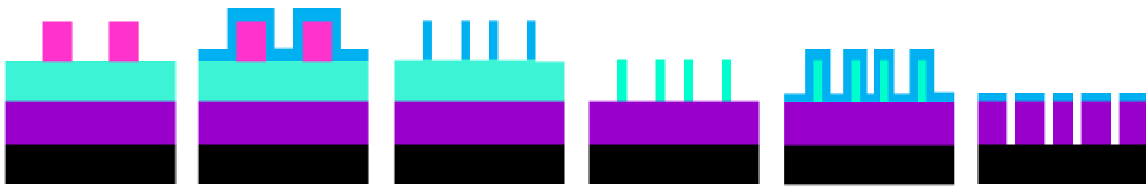

Figure 4. Stages of self-aligned quadruple patterning. From left to right: patterning of the first core (pink) on mandrel (teal); SiO_2 deposition (blue); etching of first spacers; etching of mandrel to produce second core (purple); second SiO_2 deposition; etching of the second spacers and second core layer. Adapted from Altamirano-Sanchez 2016.[10]

Selective deposition has also been investigated for use in self-aligned integration due to its hypothetical ability to fill trenches/vias without depositing across the entire wafer. This would lead to less material needing to be removed post-deposition and would allow structures to be more stable due to less chemical/mechanical polishing being required. Area selective deposition is also being investigated to possibly become a new patterning technique altogether. For example, if the deposition could be selectively dielectric on semiconductor, dielectric on dielectric, dielectric on metal, and metal on dielectric then less lithography would be required, and lithography bottlenecking might be bypassed completely.

1.2.4 Need for New Materials

Traditionally, the semiconductor industry has relied on silicon-based materials for low-*k* ILD and patterning-assist layers. The priority set in place via the International Technology Roadmap for Semiconductors (ITRS)[12] to replace SiO_2 ($k \approx 4.1$) with new lower-*k* materials has led to the transition to SiOC:H (*k* = 2.4—2.7) for ILD use, and SiC:H (*k* = 4.0—7.0) and SiCN:H (*k* = 4.5—5.8) for diffusion barrier and etch stop layers (values provided are current as of 2015).[13] However, it is becoming increasingly difficult to develop silicon variants that meet all the necessary chemical/physical requirements as well as the patterning requirements. Non-silicon-based low-*k* ILD research in recent years has been divided into two main subcategories: organic polymers and amorphous carbon, although more research has gone into the former.[14] There has also been smaller scale research of other material classes, such as boron containing materials. Through previous research in our group, amorphous hydrogenated boron carbide (a-BC:H), grown through plasma-enhanced chemical vapor deposition (PECVD), has been demonstrated to possess excellent dielectric properties, combined with very high Young's modulus, electrical properties rivaling those of SiOC:H variants, very good chemical stability, and unique and useful etch chemistry.[13,15–19]

1.3 Boron Carbide

The most common form of boron carbide (BC) has a complex crystal structure based on icosahedral and three atom linear chain building blocks with carbon atoms substituting for boron atoms throughout. While this form of boron carbide can vary over

a huge range of stable stoichiometries, $B_{4.3}C$ is said to be the most stable. The boron-to-carbon ratio can vary due to partial substitution of the boron and carbon atoms leading to B_{12}(CCC) and B_{11}C(CBC) as primary constituents, with some additional substitutional defects.[20–23]

Prior to the 1990's, dominant forms of BC were produced from sintering and hot-pressing, yielding a dense polycrystalline material not known as a good insulator.[24] Despite not being a good candidate for use as a low-*k* ILD, conventional BC was still rather attractive for industry use due to its high hardness (being the third hardest material, behind only boron nitride and diamond), high stiffness, high melting point, as well as high thermal and chemical stability.[22,23,25,26] BC also possesses high chemical and wear resistance, high modulus of elasticity, and high strength-to-weight ratio. BC has also proven chemically resistant to chemicals at temperatures lower than 600°C.[24] BC is currently being used in extreme condition applications such as scratch and wear resistant coatings[27], personal and vehicle anti-ballistic armor[28], and high pressure water jet nozzles.[29–31]

The 1990's brought new growth techniques for BC—chemical vapor deposition (CVD)[32–35] and plasma-enhanced chemical vapor deposition (PECVD)[36,37]—which, with fine-tuning of growth conditions and reagents/precursors, created a novel form of BC which has high enough resistivity to be considered for use as an ILD.[38] One BC variant grown via PECVD specifically uses the solid-state precursor *ortho*-carborane (o-$C_2B_{10}H_{12}$) with a carrier/plasma gas to grow films. The resulting amorphous hydrogenated boron carbide (a-BC:H) is a stable material that, although not as hard as the dense crystalline material, is still extremely hard.[39,40] a-BC:H is able to have a lower *k*-

value because of the hydrogen incorporation making it less dense than its hot-pressed/sintered counterpart.

Table 2. Low-k dielectric properties for a-BC:H in comparison with state of the art ILD and DB/ES. Table adapted from Nordell et al 2016.

	SiOC:H	SiCN:H	BC:H
Use	ILD	ES/DB	ILD/ES/DB
Dielectric constant (*k*)	2.2–3.2	4.8–5.8	3.3 ± 0.15
Density [g cm^{-3}]	0.9–1.3	1.7–2.2	1.5 ± 0.08
Young's modulus [GPa]	3–15$^{\alpha}$	40–100	126 ± 5
Leakage current at 2 MV cm^{-1} [A cm^{-2}]	10^{-8}–10^{-9}	10^{-7}–10^{-8}	9×10^{-9} ($\pm 6 \times 10^{-9}$)
Breakdown voltage [MV cm^{-1}]	>6	4–6	>5
Adhesion energy [J m^{-2}]	2–5	–	8.6 ± 3.3
Stress [MPa]$^{\alpha}$	$^{\beta}$	$^{\beta}$	– 400 ± 100
Thermal conductivity [W m^{-1} K^{-1}]	0.01–0.4	0.6–0.8	0.49 ± 0.04
Coefficient of thermal expansion [ppm °C^{-1}]	10–20	3–5	20 ± 4
CHF_3 plasma etch rate [Å s^{-1}]	6–15	3–6	3–12
CHF_4/O_2 plasma etch rate [Å s^{-1}]	1–10	40–50	60–180
Reference	[5,41–45]	[5,46,47]	[13]

$^{\alpha}$ – represents the range for the majority of SiOC:H films

$^{\beta}$ – highly variable

Through previous research at UMKC, Nordell *et al* were able to characterize a-BC:H films grown using *ortho*-carborane and compare the mechanical and dielectric properties to state-of-the-art a-SiOC:H as an interlayer dielectric (ILD) and a-SiCN:H as an etch stop/diffusion barrier (ES/DB) (Table 2).[13] Achieving a low-*k* value, while valuable, could not be the singular goal in fine-tuning the growth parameters of BC; the other chemical/physical properties required for integration needed to remain acceptable

as well. As reported in Table 2, most a-BC:H properties are comparable to those of SiOC:H and SiCN:H, while the Young's modulus for a-BC:H is improved upon.

With the density ever decreasing, Nordell *et al* predict a-BC:H films with densities below ~1.3 g cm^{-3} will maintain their mechanical strength required for process integration.[13,15,18,19,48] Han *et al* have also demonstrated BC films as an etch stop and barrier layer for copper dual damascene metallization.[49]

1.4 Need for ALD

1.4.1 PVD, CVD and PECVD

Traditionally, semiconductor films have been deposited by gas phase methods, which can be divided into two main groups: physical vapor deposition (PVD) and chemical vapor deposition (CVD). In PVD, a film is grown by a material being transferred from a source to a substrate by physical means. While chemical reactions can happen during the process, this is not what drives the growth. The two most common PVD processes are ion sputtering and thermal evaporation. One disadvantage in PVD for ILD films is that ILDs need to have good step coverage on the high aspect ratio features. As shown in Figure 5(a), the source material deposits perpendicularly to the substrate surface and is unable to grow on the side walls of the etched feature.

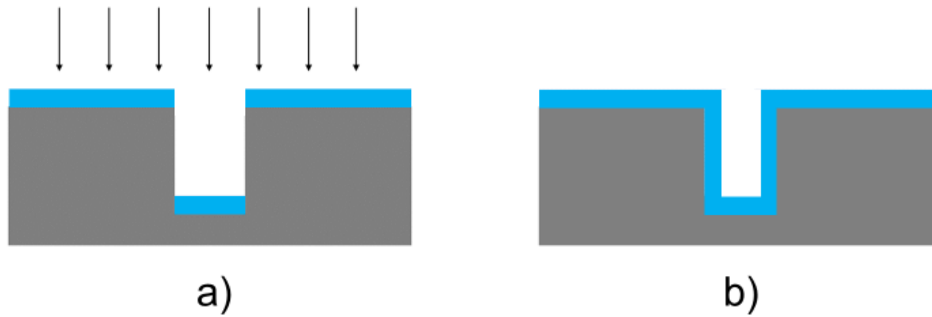

Figure 5. PVD step coverage (a) compared with the ideal conformal step coverage from CVD (b).

In CVD, a gas phase precursor is introduced into the chamber towards a heated substrate and then chemisorbs, reacts, and/or decomposes at the substrate surface to produce the desired material. Depending on the chemical reaction desired, the heated substrate temperature varies but is often quite high; for example, SiO_2 made from silane (SiH_4) and oxygen (using N_2O) requires the substrate to be heated between 750–850°C.[50,51] Figure 5(b) shows how in an ideal CVD process the side walls would have equal chemical reactions and therefore conformal growth on the horizontal and vertical surfaces.

Plasma-enhanced chemical vapor deposition (PECVD) is a deposition process which uses plasma to dissociate, excite, or ionize reactants. PECVD uses similar chemistry as CVD but allows more flexibility of the reaction. This flexibility allows the chemical reactions to happen at a lower temperature than with CVD thus allowing growth of the widest variety of materials, even in more “sensitive” integration schemes. In the case of SiO_2, the deposition temperature is lowered to between 200–350°C.[51] Although the conformality of CVD and PECVD is better than that of PVD (due to their multi-directional growth), PECVD tends to not have as conformal growth due to the plasma not

reacting with the substrate evenly.[52] Even with its lack of conformality, PECVD has become the de-facto method for ILD deposition (and deposition of many IC layers) because of the wide variety of materials available for deposition and tunability of the growth conditions.

Despite its flexibility for growing many types of materials, drawbacks to PECVD in thin-film growth are the lack of precise control in thickness, uniformity, and conformality. Modern nano-scaling requires strict control in all aspects of film growth and has led researchers to investigate novel growth processes. One such process is atomic layer deposition (ALD), which allows film thickness and other deposition qualities to be controlled even better than in CVD due to its self-limiting nature.

1.4.2 What is ALD?

The first ALD research, then known as atomic layer epitaxy, was conducted in the 1960s in the former Soviet Union and in the 1970s in Finland.[53] Belonging to the CVD group, ALD differentiates itself from CVD by self-limiting chemical reactions which regulate its deposition thickness.[54–56] The ALD process consists of substrate exposure to alternating sequential precursor cycles.[53,57–64] Figure 6 shows the steps of traditional ALD, where in each alternating pulse or half-cycle, the precursor reacts with the surface in a self-limiting way. The self-limiting nature of ALD ensures that the reaction stops once all the reactive sites on the substrate have been saturated. The ALD cycle can be performed multiple times to increase the layers of the thin film, depending on the requirement. ALD allows for the deposition of ultra-thin oxide or metal films with

extremely accurate sub-nanometer thickness control. ALD can grow films with high material quality, high uniformity, and excellent conformality (Figure 7).

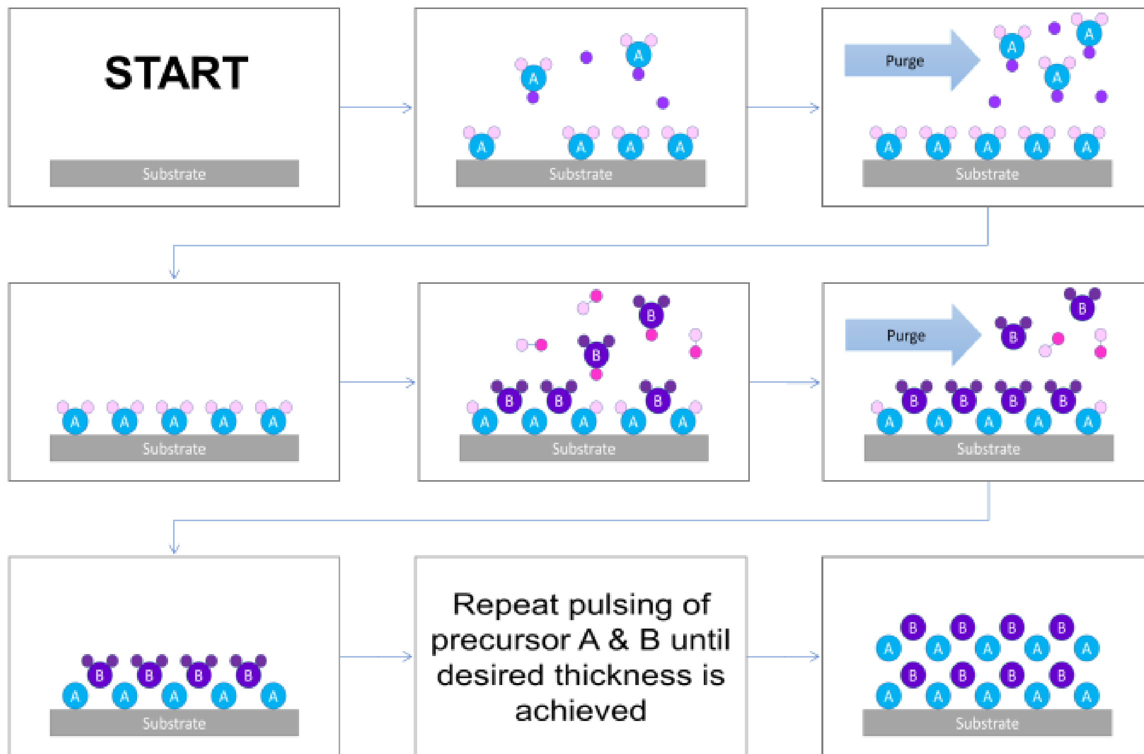

Figure 6. ALD process flow.

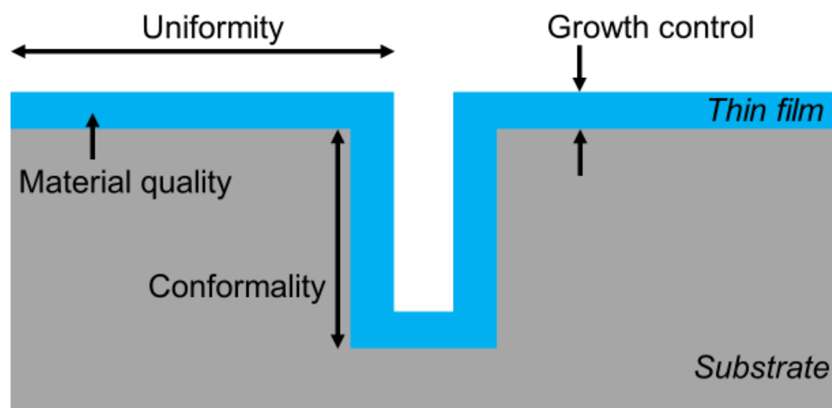

Figure 7. Illustration of properties of ALD. Adapted from Profijt 2012.[57]

Because of the stringent ALD requirement of self-limited surface saturating reactions, much research has gone into the dependence of growth rate on deposition temperature.[59,65] Figure 8 shows the correlation between growth rate and deposition temperature and how it can promote or inhibit growth. Only inside the ALD window is the growth rate saturative but not dependent on temperature.[66,67] Outside of the ALD window, non-saturative growth can occur at high and low growth rates. High growth rates with low deposition temperature can be attributed to precursor condensation, while precursor decomposition may occur at high temperature. Low growth rates can be attributed to incomplete reactions at too low deposition temperature and precursor desorption at too high temperatures.

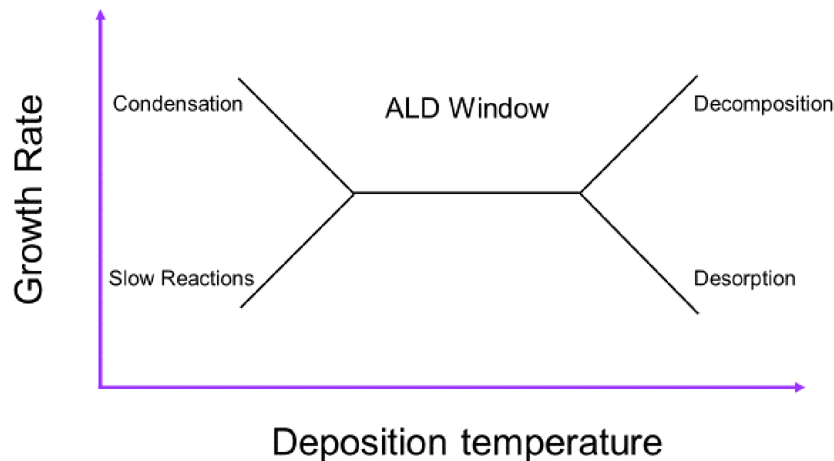

Figure 8. ALD window depicting the dependence of growth rate on deposition temperature.

1.4.3 What is MLD?

Molecular layer deposition (MLD) is closely related to ALD in that it is based on sequential, self-limiting surface reactions; Figure 9 illustrate the difference between ALD and MLD. As the name implies, MLD is based on molecular layers instead of atomic

layers.[68] MLD uses molecular precursors to extend the type of materials which can be grown to organic and hybrid organic–inorganic polymeric materials.[69] MLD was first developed in 1991 by Yoshimura; however, MLD as compared to ALD is still in its infancy with just over 100 research papers recorded in totality. Whereas ALD has several hundred review papers summarizing its mechanisms, capabilities, and applications,[59–64,70,71] MLD only has around ten that cover specializations of MLD or newly published processes.[68,69,72–78] These specializations or subcategories of MLD processes can be described or grouped as the growth of two-dimensional (2-D) linear chains and three-dimensional (3-D) hybrid organic–inorganic polymers.

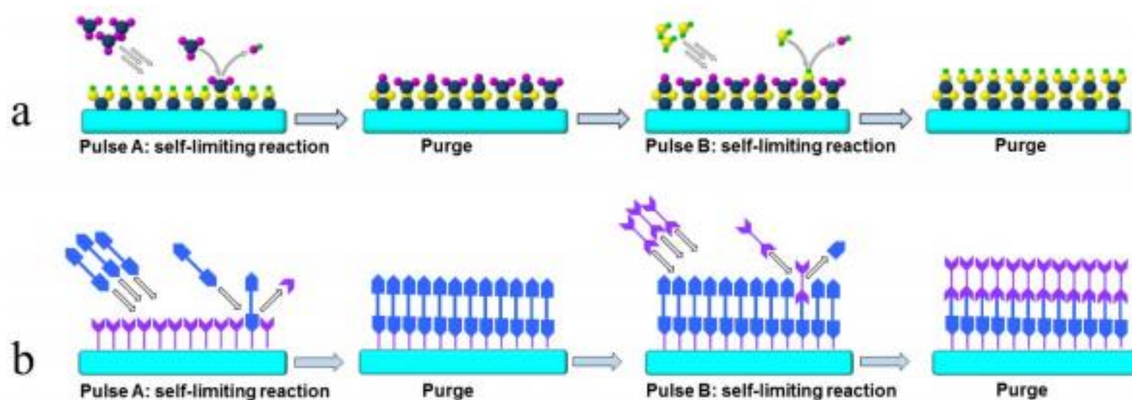

Figure 9. (a) ALD vs (b) MLD self-limiting reactions and growth. Reprinted with permission. Copyright 2011 Journal of Materials Chemistry A.[68]

In the “pure” 2-D MLD, linear chains are grown using bifunctional organic monomer precursors. As shown in Figure 10(a), the MLD chains are based on the “A” and “B” self-saturative half cycle reactions—similar to the ALD process in Figure 6—but grown using organic fragments.[78] 2-D linear chain MLD growth is prone to tilting and reacting twice with the surface, sometimes resulting in lower than expected growth rates,

as illustrated in Figure 10(b). Choosing organic precursors with shorter chains can improve the chances for higher growth rates, but because growth is not always perpendicular to the surface this is not necessarily the case. George *et al* review the difficulties in choosing organic precursors for MLD applications.[67,69,73,78]

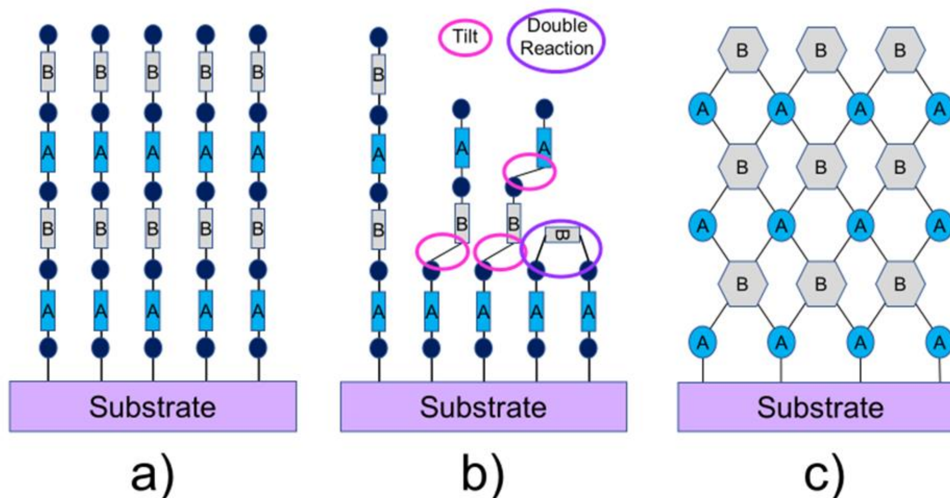

Figure 10. (a) Two-dimensional MLD linear chains. (b) Types of growth defects that cause lowered growth rates in organic and inorganic–organic films. (c) Three-dimensional MLD structure.

The 3-D film shown in Figure 10(c) is grown using both inorganic atomic (ALD-type) and organic molecular (MLD-type) precursors. This type of 3-D film demonstrates increased stability, compared with 2-D films, due to the bonding between layers. In this ALD/MLD hybridization, ALD (“A”) and MLD (“B”) precursors alternate as layers to create the hybrid organic–inorganic films.

1.4.4 What is PEALD?

Plasma-enhanced atomic layer deposition (PEALD) is to ALD as PECVD is to CVD. There are two distinct plasma processes that have been studied for PEALD. In the

first and most common case, a plasma is used to exploit the creation of reactive species that substitute for the second half cycle of traditional thermal ALD processing (Figure 11).[53] In the second case, the plasma creates surface reactive sites to which can bind reactants in the second half cycle.[79,80] PEALD employs the use of a plasma to extend the temperature range in which ALD growth can occur and allows for accessing previously inaccessible chemistries.

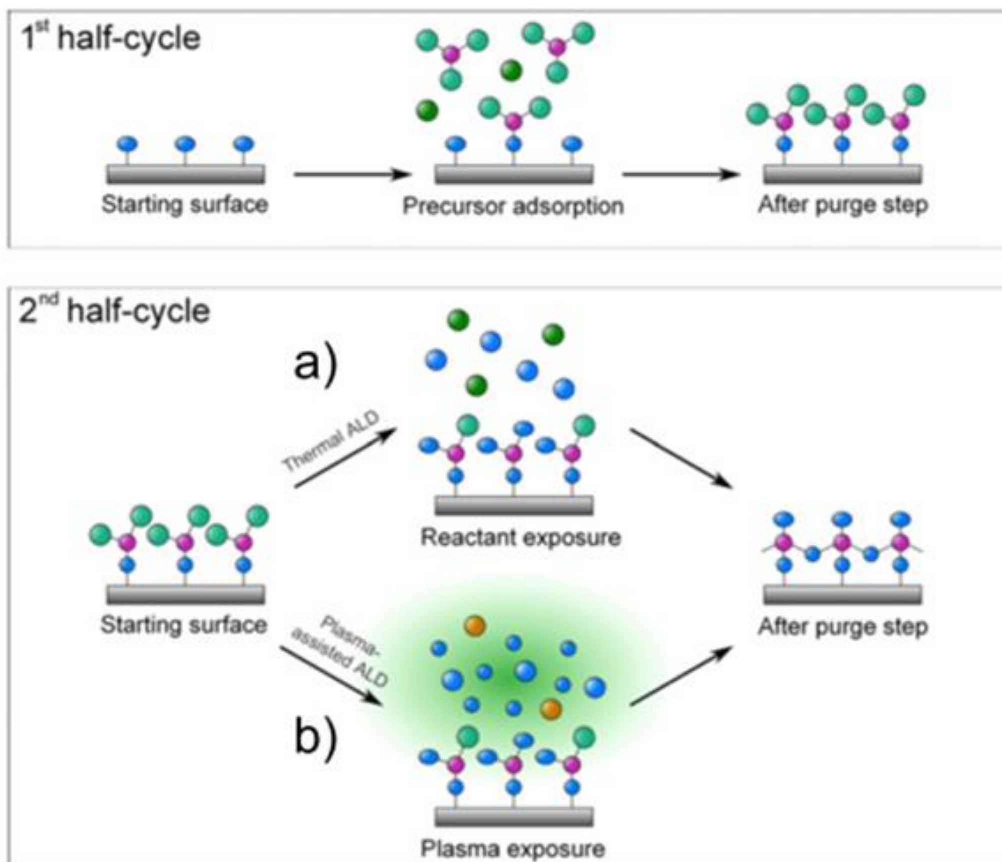

Figure 11. Difference in (a) ALD and (b) PEALD growth. Reprinted with permission. Copyright 2011 Journal of Vacuum Science.[53]

To produce a plasma, an electric field is applied to a gas. Subsequently, electrons are accelerated and reactive species such as radicals, ions, and photons are created upon

collisions between electrons and neutral gas species. There exist various reactor chamber configurations that allow different parts of the plasma to be used for different growth techniques. Figure 12 shows several PEALD reactor configurations: (a) radical-enhanced ALD, (b) direct plasma-enhanced ALD, (c) remote plasma ALD, and (d) direct plasma reactor with mesh.

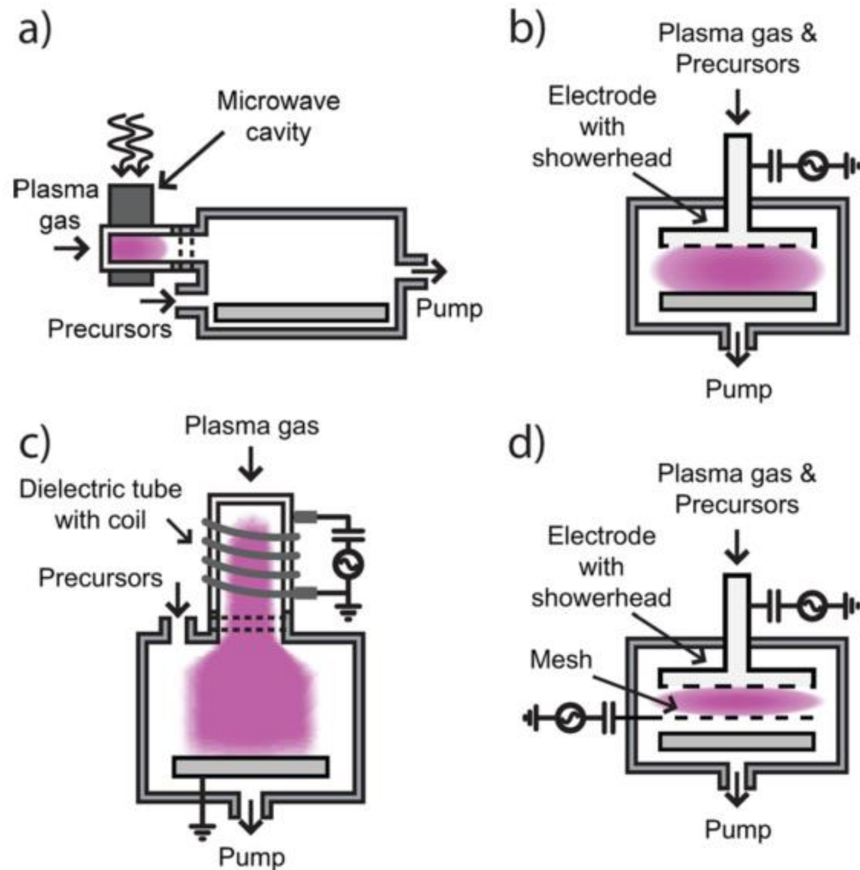

Figure 12. Various PEALD reactor configurations: (a) radical-enhanced ALD, (b) direct plasma-enhanced ALD, (c) remote plasma ALD, and (d) direct plasma reactor with mesh. Reprinted with permission. Copyright 2007 American Vacuum Society.[81]

Radical-Enhanced ALD Reactor (REALD)

The reactor configuration in Figure 12(a) is typically used when a plasma source is added onto an existing ALD reactor and is frequently some distance away from the

reaction chamber. This distance can be an advantage and disadvantage to REALD. The advantage is that because of the distance, only radicals (not electrons or ions from the plasma discharge) are able to reach the substrate, causing less defects on the substrate surface. However, because radicals absorb to all the system's surfaces, extra care must be taken in the selection of materials for deposition as well as the system distance from plasma source to substrate placement.[53,66] This reduces the chemistries available for film growth and can make this plasma configuration undesirable.

Direct PEALD Reactor

In the reactor configuration in Figure 12(b), the plasma gas and precursors flow into the reaction chamber through a showerhead or in from the side of the chamber. The plasma in this case is created through capacitively coupled parallel plate electrodes with the substrate mounted directly on one of the electrodes. Because of this, the surface interacts with the electrons, ions, and radicals aiding in the PEALD growth.[82–93] In principle, this enables uniform deposition over the full wafer area with short plasma exposure steps. Of course, direct PEALD reactors have their own advantages and disadvantages. The obvious advantage is the proximity of the substrate to the plasma which allows for more plasma species to interact with the surface and be distributed evenly. On the other hand, the high energy reactive species can also damage the surface so tuning the plasma parameters is necessary. The plasma sheath can be tuned to protect the substrate from damaging high energy species. Figure 12(d) illustrates a direct PEALD reactor variation that has employed a mesh to decrease the number of destructive electrons and ions reaching the substrate.

Remote PEALD Reactor

The reactor configuration in Figure 12(c) is an example of a remote PEALD reactor. Remote PEALD is similar to REALD but the plasma is still present above the deposition surface and in the case in Figure 12(c), is an inductively coupled plasma. With REALD the plasma can be either capacitively coupled or inductively coupled. An advantage to using remote PEALD is that the plasma and substrate conditions can be varied independently. With direct PEALD this is more difficult to achieve due to the substrate temperature affecting the gas temperature. The gas temperature is important because it affects the density of the gas phase species which can enable or prohibit plasma generation.[53,94]

1.4.5 ALD of BC

Suppose BC was capable of being grown via ALD. Example atomic precursors might include BCl_3 and CH_4. It is not clear that the complex icosahedral geometry of BC (Figure 13a) could be reproduced with such precursors using traditional ALD or that a self-limiting chemistry scheme exists. However, the use of molecular carborane derivatives, which have already been established as a successful precursor in the PECVD growth of BC films could enable layer-by-layer MLD growth with appropriate coupling chemistry. The molecular carborane derivatives, containing 12 symmetric reactive sites and capable of cross-linking, would provide more stable growth (and therefore films) and potentially 3-D growth versus the traditional bifunctional organic molecular precursors used in MLD.

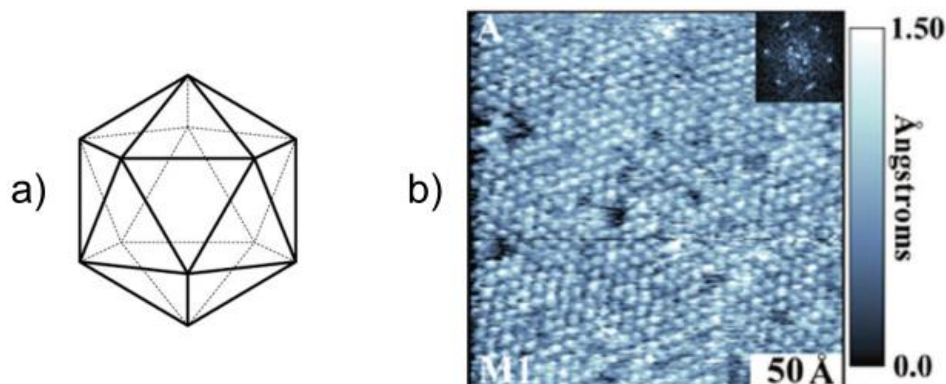

Figure 13. (a) Icosahedral geometry of BC and (b) scanning tunneling microscope images of thiol-carborane SAM. Reprinted with permission. Copyright 2009 American Chemical Society.[95]

The carborane derivatives could conceivably be deposited layer-by-layer using established self-assembled monolayer (SAM) chemistry followed by plasma-assisted grafting (or surface excitation)[79], and plasma cross-linking polymerization. One strategy for the first layer would be using thiol-carborane derivatives on metal substrates. Thiol-carborane based self-assembled monolayers (SAMs) can be grown on gold, silver, and copper substrates (Figure 13b).[95–99] Referring back to Figure 9 and Figure 11, these SAMs would serve as the "B" layer of the MLD process, and by using a plasma as the "A" step we predict the cross-linking and creation of reactive sites for additional carborane layer depositions. There are many commercially available carborane derivatives and established surface pre-treatments that could conceivably allow for other MLD chemistries to be possible.[55,58] We predict that plasma will effectively create reactive species on these materials and with the fine tuning of plasma/precursor conditions, BC growth via plasma-enhanced molecular layer deposition (PEMLD) will be possible.

1.5 Thesis Roadmap

Through the next two chapters, the design of the reactor chamber as well as the deposition and characterization of the PEMLD films will be discussed. Within Chapter 2, the general design for sample transfer, flow, plasma generation, and heating are described. Chapter 3 goes into the results for the thiol-carborane SAM chemistry as well as multi-layer, multi-cycle experimentation. Many dosage tests were conducted to determine successful SAM chemistries before multi-cycles could be achieved. Once the precursor dosing parameters were determined, the plasma doses and multi-layer, multi-cycle chemistry testing was performed.

CHAPTER 2

EXPERIMENTAL

2.1 Reactor Design

2.1.1 General Overview

In order to produce PEMLD films, a reactor chamber suitable for growth first needed to be built. Part of the challenge in the design and fabrication of the chamber was incorporating previously used chamber components and making use of existing equipment in the most effective way. One of the preferred design specifications was to attach the chamber to a pre-existing X-ray photoelectron spectroscopy (XPS) system and resistive evaporation chamber. The benefit of having the PEMLD chamber attached to this existing system was the ability to perform *in situ* pre-PEMLD copper substrate deposition and post-growth XPS characterization. Figure 14 shows how the PEMLD chamber was integrated with the XPS system. The decision to have the PEMLD chamber perpendicular to the XPS system was made due to laboratory spatial constraints and the cost factors involved with purchasing and installing a longer transfer arm.

The reactor was designed to be a direct plasma PEMLD reactor with gas and precursor flow through a showerhead (details forthcoming). Figure 15 shows a general overview of the PEMLD reactor. Most of the components used have the ability of being controlled both manually and remotely through a graphical user interface. The automated control will not be covered in detail here.

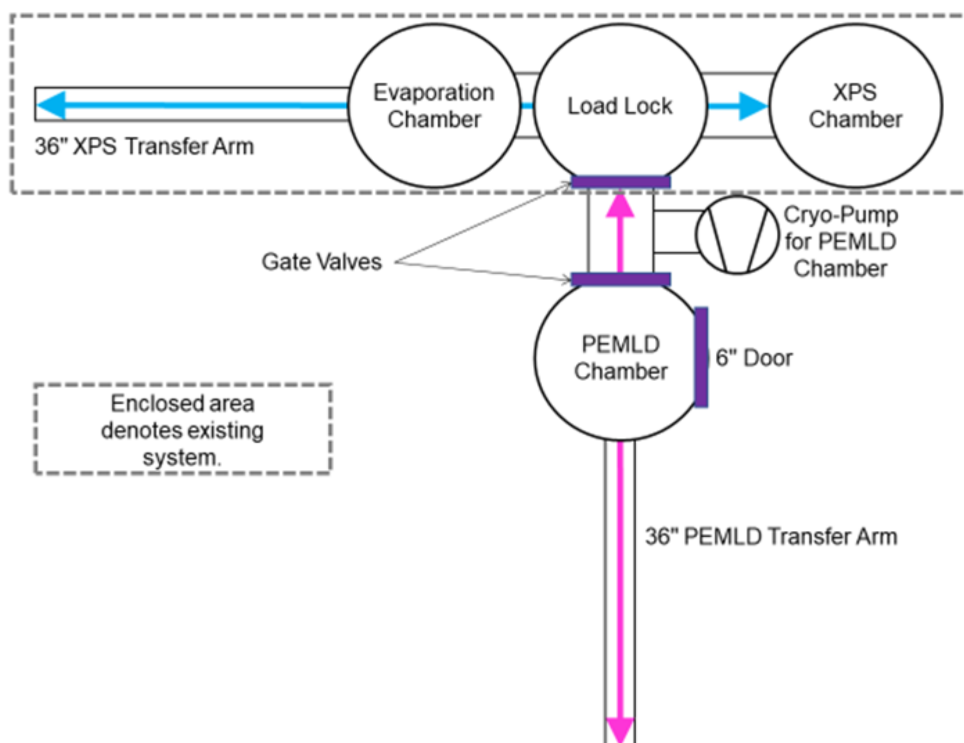

Figure 14. Top-down view of PEMLD chamber with XPS and evaporation chamber configuration. The evaporation chamber has a 6" door on the top for loading samples.

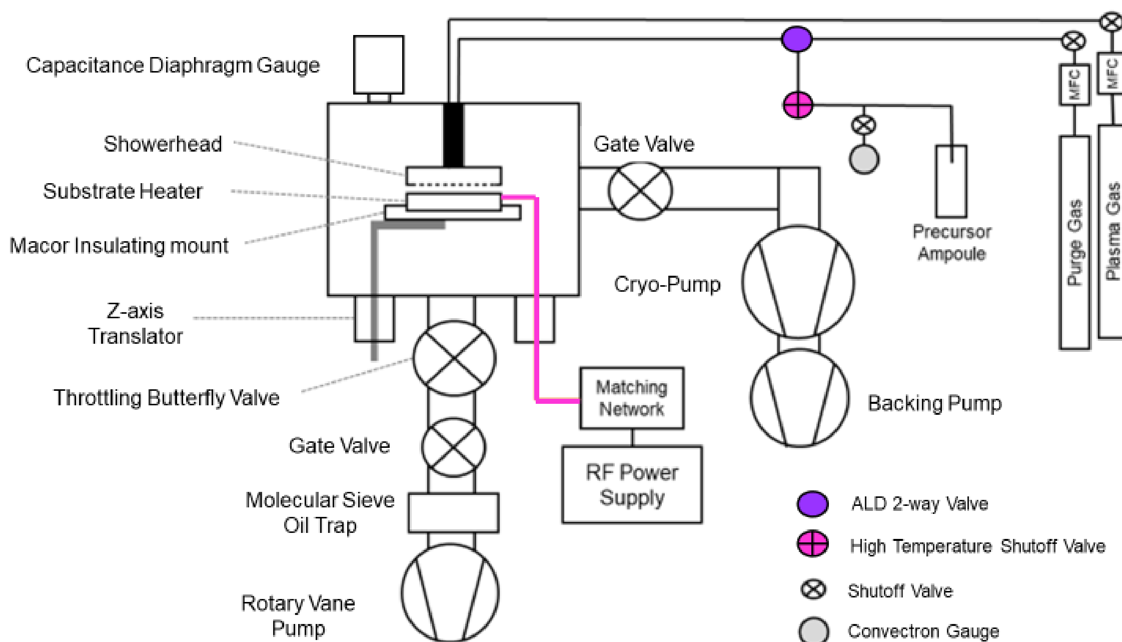

Figure 15. Reactor schematic showing major components (note: not all components are shown).

2.1.2 Substrate Holder/Heater

The substrate holder/heater was designed out of copper due to this metal's high conductivity, allowing even heating of the substrate. Two heater cartridges from O.E.M. Heaters, capable of heating to 500°C, were placed between two ½" copper plates and held in place through friction (Figure 16). To allow secure pick-up and drop-off of the sample between transfers, a 1/8" recession was made in the center of the sample holder. The recession size corresponds with the sample puck currently used in the XPS system. Due to size constraints from the chamber transfer tubing, door, and heater size, the maximum sample size that can be accommodated is a 3" wafer.

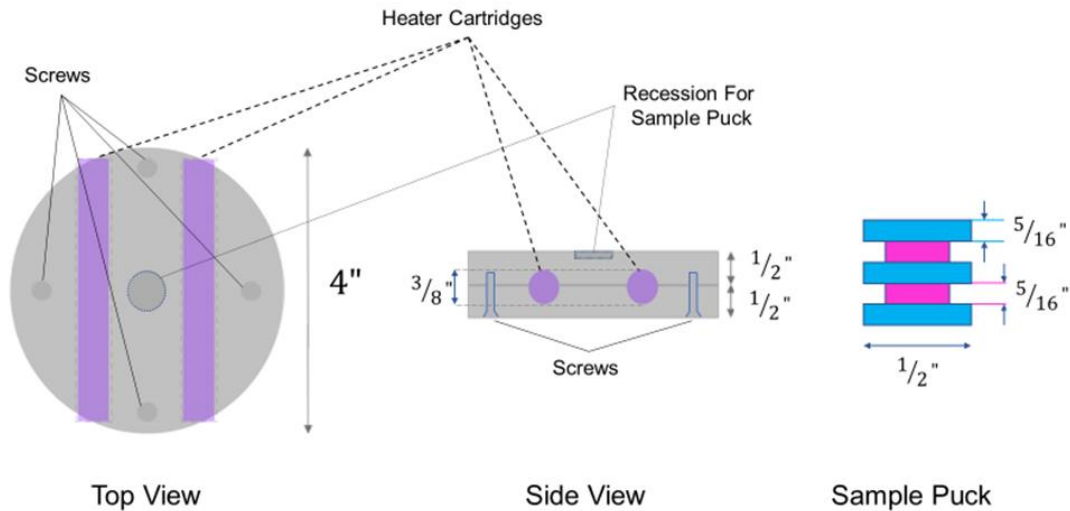

Figure 16. Top and side view of the substrate holder/heater with sample puck design and dimensions.

The substrate holder/heater was chosen to be the powered electrode—due to grounding complications arising in the showerhead—and because of this the cartridge heaters were powered without grounding. The substrate holder/heater was also designed to have the ability to be moved in the z-axis direction to accommodate sample transfer

and ellipsometry alignment (details forthcoming). The z-translator made by Nor-Cal Products was designed with a 2" stroke. Another consideration with plasma generation was insulating the substrate heater/holder from the z-translator to prevent grounding. A 6" × 5" × ½" thick piece of Macor (a glass-mica ceramic) was machined to hold the substrate heater/holder and reduce plasma arcing.

2.1.3 Sample Transfer

To accommodate the transfer of the sample puck between the load-lock chamber and PEMLD chamber, a 36" stroke magnetic linear/rotary transfer arm from Nor-Cal Products was purchased and installed as shown in Figure 14. The two transfer arm forks would meet in the load-lock chamber and transfer the sample from one to the other. Figure 17 shows the top-down view of the transfer between the PEMLD transfer arm fork and the evaporation/load-lock/XPS transfer arm fork.

Figure 17. Top-down view of the sample puck transfer between the PEMLD transfer arm fork (left) and evaporation/load-lock/XPS transfer arm fork (right).

The loading and unloading of the sample puck on the substrate heater/holder is shown in Figure 18. In this figure, the transfer arm comes in from the side (1) to a position capable for “pick-up” (2). The “pick-up” occurs when the substrate heater/holder is lowered via the z-translator (3). Then the transfer arm and sample puck are clear to be transferred to the load-lock chamber (4). The “drop-off,” for sample loading on the substrate heater, is done in the reverse order.

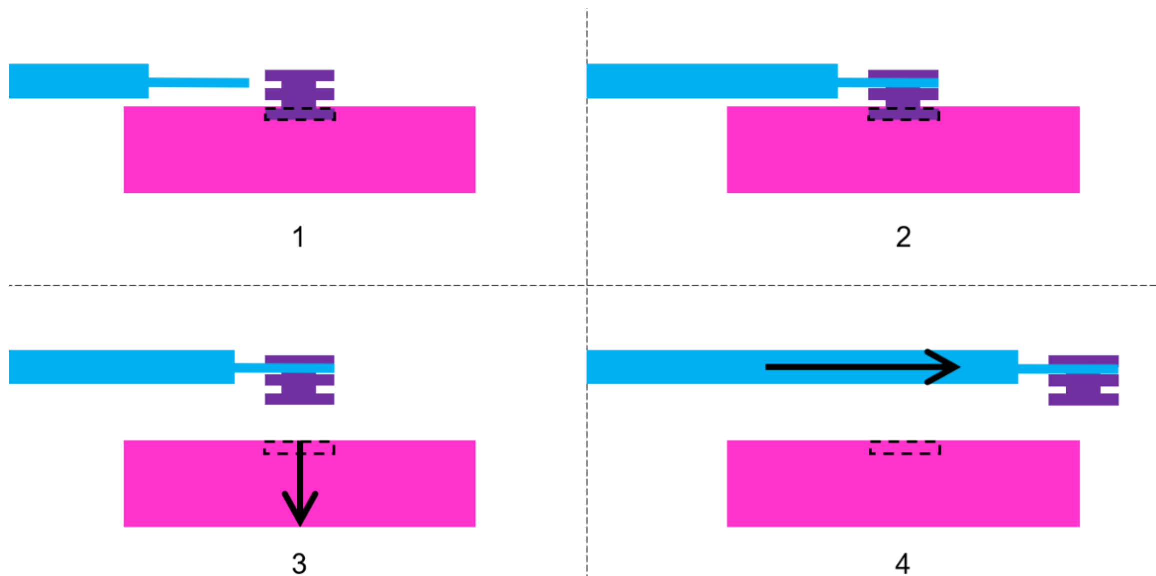

Figure 18. The PEMLD transfer arm picking up the sample puck from the substrate heater/holder and transferring to the load-lock chamber.

2.1.4 Flow Design and Control

Precursor, Plasma, and Purge Gas Control

The flow control for the precursor, plasma, and purge gas was designed to allow for either manual or automated control. A two-valve monoblock Swagelok ALD Diaphragm Valve (Figure 19) was used for precursor and purge gas flow into the chamber. The ALD valve was chosen because of its ultra-high cycle life, rapid actuation speed, and ability to be heated to 120°C while in operation. The purge gas was designed

to flow behind the precursor to both purge the lines upstream from the reactor chamber and be available as a plasma process gas. Research grade (99.9997%) nitrogen was chosen as the purge gas.

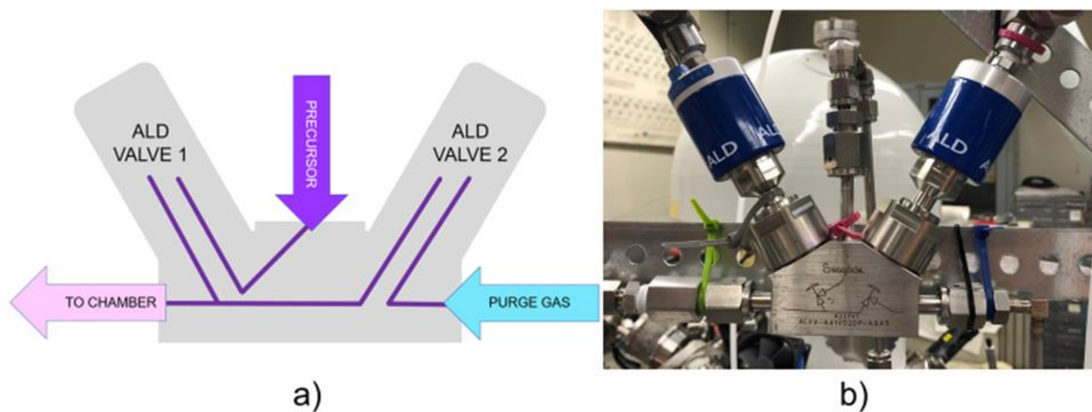

Figure 19. Swagelok two-way ALD diaphragm valve with flow design (a) and actual Swagelok two-way ALD valve (b).

The ALD valves were controlled manually through a light switch assembly. Each light switch was wired to a solenoid valve attached to the air inlet port of the ALD valve. The ALD valves were automated through an electronic actuated-positioning sensor which is an accessory option for the ALD valve at the factory. A 10–30 VDC is applied to the normally closed pneumatically actuated valve to open the valve. The flow of purge gas was controlled through an MKS 179C, 100 standard cubic centimeters (SCCM) mass flow controller (MFC). To prevent a possible buildup of purge gas, the MFC would be turned on only after the ALD valve was opened and turned off before the ALD valve was closed. The plasma gas was plumbed into the showerhead using the second gas feedthrough and controlled with its own MFC. The flow rates for both MFC's were

controlled using a voltage between 0 and 5 VDC, which corresponds to a predetermined flow rate. The MFCs were calibrated with a mass flow meter to ensure correct flow.

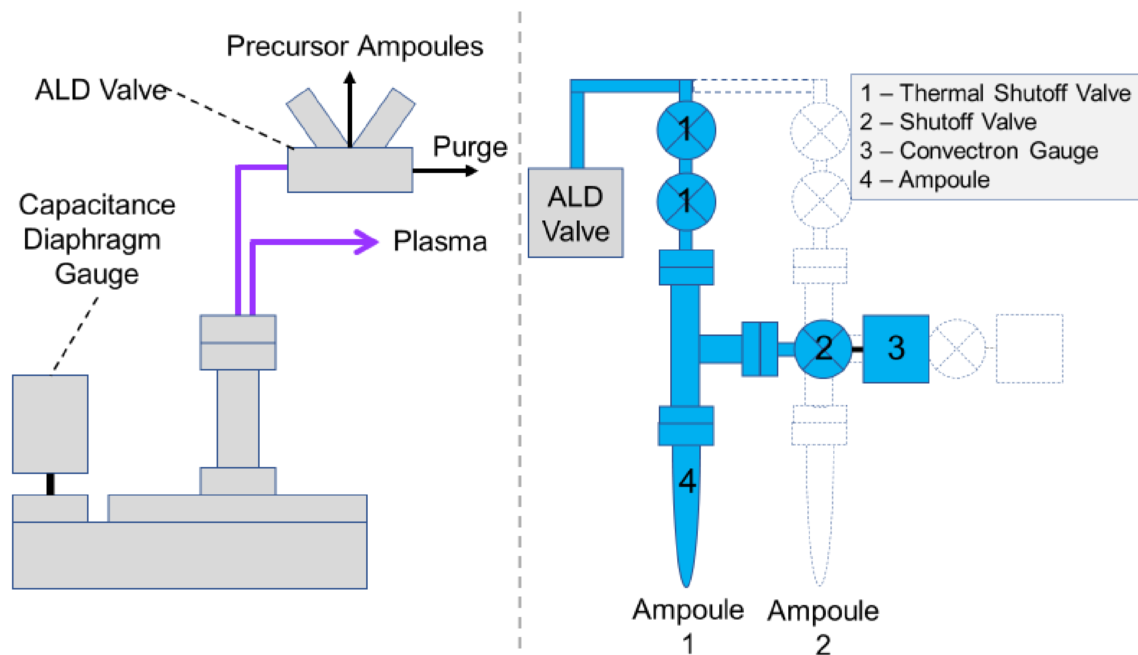

Figure 20. Precursor, plasma, and purge gas delivery.

To handle solid precursors, glass ampoules were installed such that when the solid precursor is sublimed, the vapor can be directed to the chamber through the ALD valve, shown in Figure 20. To prevent contamination of the precursor during sample loading and to prevent the need for the chamber to be vented, two Swagelok high temperature thermal shutoff valves were connected between the ALD valve and ampoule. This allows the section between the thermal valve and the ampoule to be taken into a glovebox for sample loading. To determine the amount of precursor needed in each growth cycle, a corresponding vapor pressure curve is referenced, and the ampoule is then heated to the temperature required for the desired vapor pressure. A convectron gauge was installed to

verify that pressure is reached. The convectron gauge was mounted with a shutoff valve of its own to help prevent condensation of the precursor on the gauge.

The top flange, in which the showerhead, electrical, and gas feedthroughs are attached, was designed to come out as one solid piece in case of service or repair (Figure 21(a)). The showerhead was custom-made in the UMKC Physics machine shop. It was designed to have Teflon® gas diffusion inserts that could be removed and cleaned as needed. Figure 21(b) shows a side view of the showerhead with the Teflon® inserts, the gas lines, and mounts. Figure 21(c) shows how the gas lines and mounts attach to the showerhead in a top view and how the gas exits the showerhead in a bottom view.

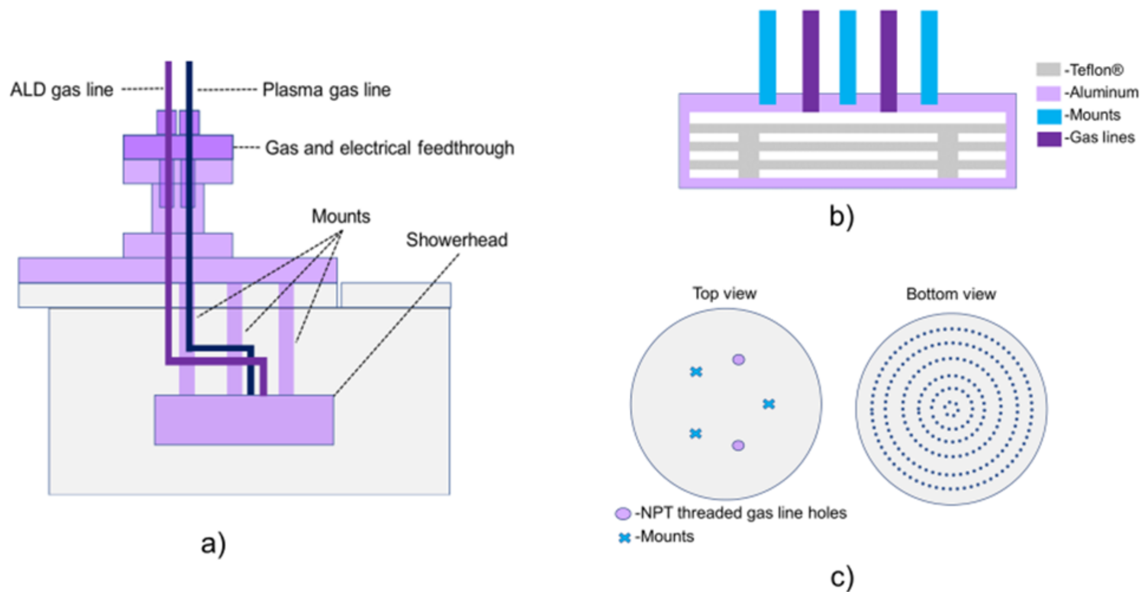

Figure 21. (a) The top flange of the chamber shown as a whole, (b) cross-sectional view of the showerhead, (c) top and bottom view of the showerhead.

Pressure Control

An NW-63 Intellisys throttling butterfly valve (TBV) was chosen for pressure control during growth cycles. The TBV was mounted between the chamber and rotary vane pump to make use of downstream pressure control—shown in Figure 15. A Welch DuoSeal 1397 vacuum pump was chosen for downstream control due to its higher pumping speed at low pressure (10^{-3} Torr) as compared to other rotary vane pumps, as well as its ability to withstand harsh chemicals. An MKS capacitance diaphragm gauge was mounted at the top of the chamber and relayed pressure information to the valve's on-unit controller, adjusting the valve's position to maintain the desired process pressure. The TBV minimizes the time for the system to achieve the process pressure. This is important because ALD film growth typically takes longer than other types of growth processes so decreasing the cycle time and increasing throughput is critical. A molecular sieve trap was attached in-line with the Welch pump to prevent any backstream flow of pump oil.

Ultra-high vacuum pumping—done with a CTI Cryogenic 4F pump (Figure 15)—and bake-outs were performed before and after each growth.

To ensure that there were no leaks, several leak-checks and pressure tests were performed on the chamber. A Stanford Research System – Residual Gas Analyzer (SRS-RGA) was used as a helium leak detector for the system. The chamber started with blanks on all of its flanges except for the pressure gauges (dual convectron/ion gauge), Welch pump plumbing, and SRS-RGA. Then after a 24-hour bake-out, one component would be attached and reevaluated with respect to its leak testing performance. Figure 22(a) shows the starting configuration for the pressure and leak testing. The Welch pump was used to

bring the chamber pressure down to the 10^{-3} Torr range where the cryo-pump would take over the pumping and bring the chamber down to base pressure. Both the Welch and cryo-pump were isolated from the chamber with gate valves rated to 10^{-10} Torr; neither was opened while the other was pumping on the chamber. After the pressure test was performed the chamber would be pumped down by the cryo-pump and the leak testing would begin.

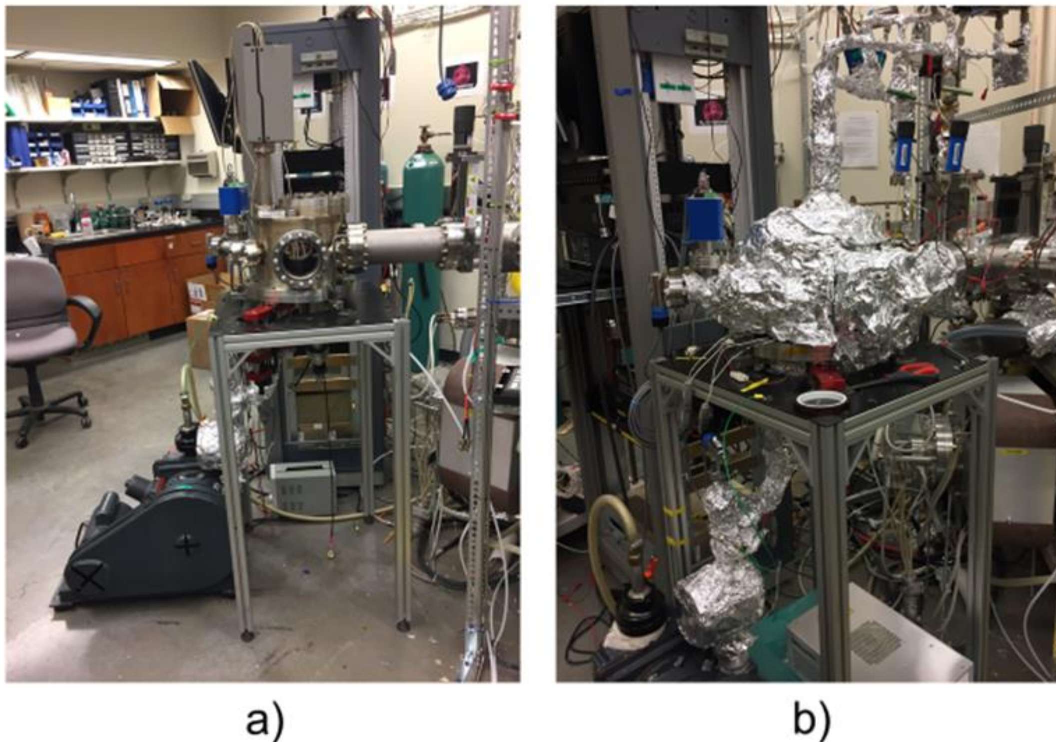

Figure 22. (a) Starting configuration and (b) final configuration for pressure and leak testing of the chamber.

Leak-testing of the chamber helped to pinpoint the leak(s) in the components which could then be switched out or repaired. While the system reached an initial "dirty" (that is, pre-bake-out) base pressure of 2.7×10^{-7} Torr, once all components were attached and baked-out, the system was able to reach a base pressure of 5.0×10^{-9} Torr.

The starting and final configurations of the chamber, with all chamber components attached, is shown in Figure 22.

2.1.5 Plasma Generation

As touched on before, the reactor is a direct PEALD reactor with the showerhead—providing the plasma gas to the reaction chamber—being the grounded electrode and the substrate holder/heater being the powered electrode. The electrode configuration was chosen due to grounding complications that might have made plasma generate inside the showerhead and not between the showerhead and substrate holder/heater. The plasma is created by applying a RF voltage across two parallel metal plates which creates an oscillating electric field. To keep the plasma neutral, sheaths with electric fields perpendicular to their surface form next to the plates (Figure 23(a)). The sheath potential drop prevents fast-moving electrons from escaping faster than the ions, while at the same time, accelerating the ions to bombard the surface. Because the plasma potential oscillates, the two sheaths will be identical but out of phase, therefore the electrode configuration could be chosen arbitrarily.[100,101] Direct PEALD was desired due to the plasma interacting with the surface and functionalizing an otherwise nonreactive surface.

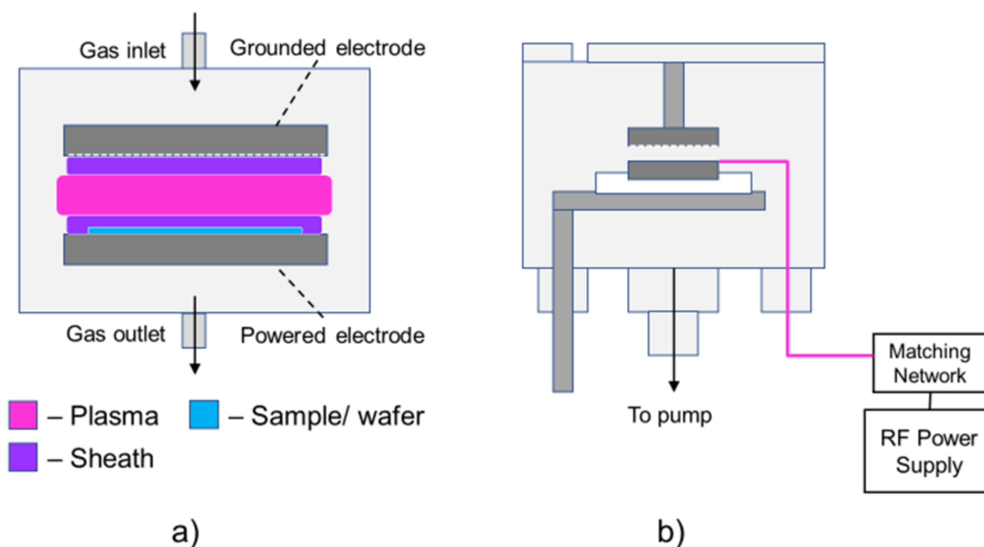

Figure 23. (a) Capacitively coupled plasma configuration, (b) plasma component configuration of home-built reactor.

Figure 23(b) shows the plasma component configuration of the PEMLD reactor. A Comdel CX-1350S RF generator and an ENI Matchwork 5D impedance matching network with auto-tuning were used in plasma generation. A custom-made wiring harness was attached to the matching network and RF power feedthrough. The wiring inside the chamber was attached using Kapton-encased RF-rated copper wiring and then secured to the heater. Along with the advantages of having z-axis translation of the heater/sample holder for transfer, the z-translator allowed for the tuning of sheath thickness and gap distance (from 0.5–2.5").

2.1.6 Heating

Heating is a crucial component in the design of the chamber with many considerations as regards to the type of heating needed, temperature range required, and compatibility with other components. Due to the fact that most ALD reactors tend to be of the hot/warm wall type to prevent/slow down any adsorption/desorption processes on

the walls of the chamber, the chamber walls here needed to be heated. The same consideration for adsorption/desorption is needed for the precursor lines and gas flow. A traditional hot wall reactor is built inside of a furnace with the walls/source lines being the same temperature as the substrate. As an alternative to the chamber being located inside a furnace, warm wall reactors heat the walls below the deposition temperature but high enough to ensure rapid desorption.[60,78,102,103]

The reactor chamber in this work is a warm wall type reactor with the walls and precursor source lines divided into zones for heating. By reducing the size of the zones, the chamber components can be more precisely/accurately controlled. Each zone was wrapped using high-temperature heat-cable capable of temperatures up to 450°C. Quick-check thermocouples were mounted in each zone to monitor and drive the automated heating for each zone. The power to each heat-cable is driven through either manual variable control or proportional, integral, derivative (PID) control. The PID control, which provides continuous variation of output within a control loop feedback mechanism, is driven using a custom automation program.

Heating zones 1–4 are shown in Figure 24 and represent the downstream heating. Heating zones 5–8, shown in Figure 25, show how the chamber walls are heated. The ellipsometry port (2) is heated using a combination of zones 7 and 8, while the ellipsometry port/door (5) is heated by zone 5. Although the ALD transfer arm is considered part of the chamber walls it is not continuously heated due to the limitations this would have on its function. Instead the transfer arm will be baked-out in periodic intervals corresponding with instrument use.

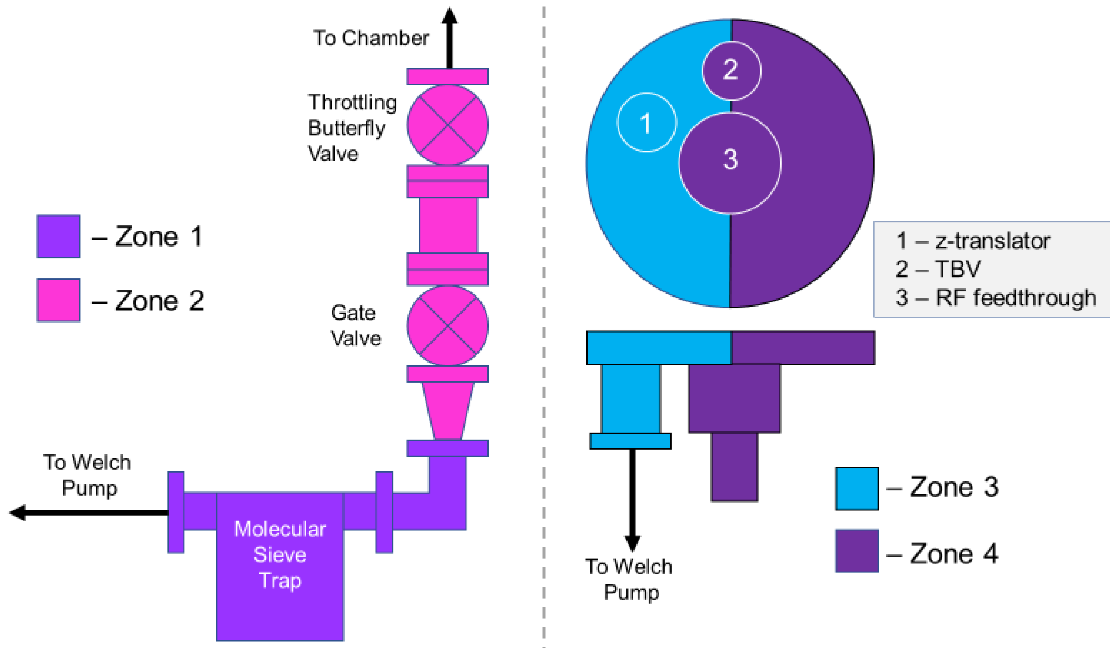

Figure 24. Heating zones 1-4.

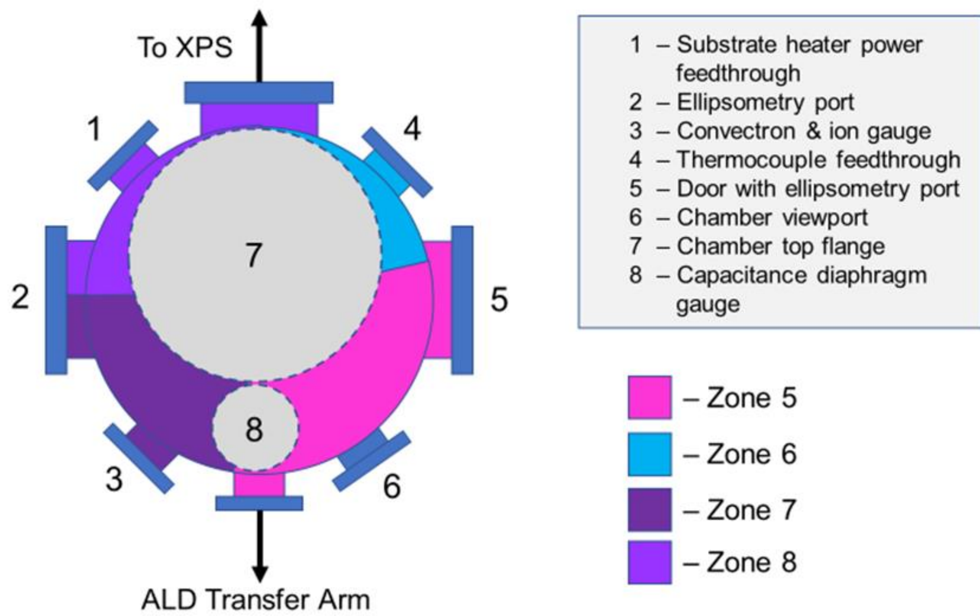

Figure 25. Heating zones 5-8.

Zones 9 and 10, shown in Figure 26, represent the upstream heating pertaining to precursor flow. Although not shown in Figure 26, the purge and plasma gas lines—from

the chamber up to the MFC—are heated by zone 9. As can be seen in Figure 27, the lines can be isolated or baked-out completely from bottle to MFC. When they are not in use the lines are kept under vacuum to reduce contamination.

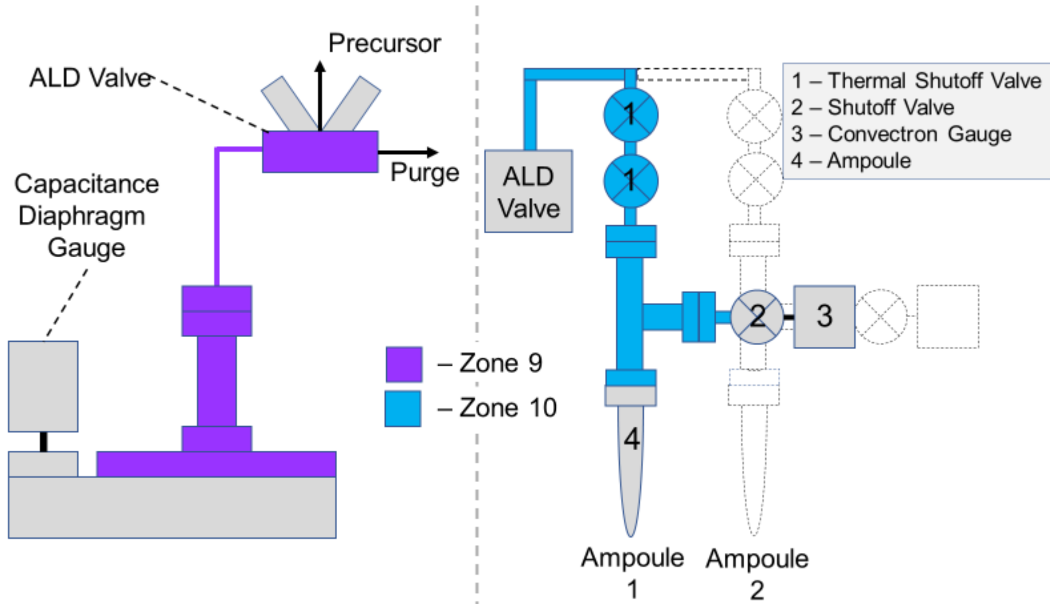

Figure 26. Heating zones 9-10.

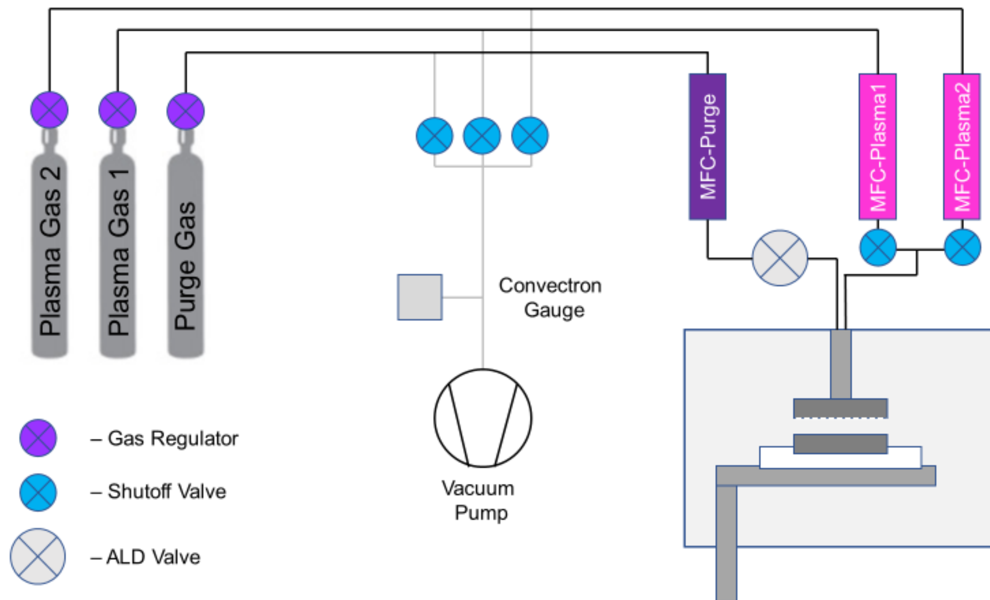

Figure 27. Upstream gas line configuration.

The ampoules that contained the different precursors for PEMLD growth each had their own heating zone; zones 11 and 12 are shown in Figure 28. The glass ampoules were wrapped with highly conductive metal sheets followed by the heat-cable and additional metal sheets to evenly distribute the heat. Each ampoule had its own thermocouple due to precursor heating being especially sensitive.

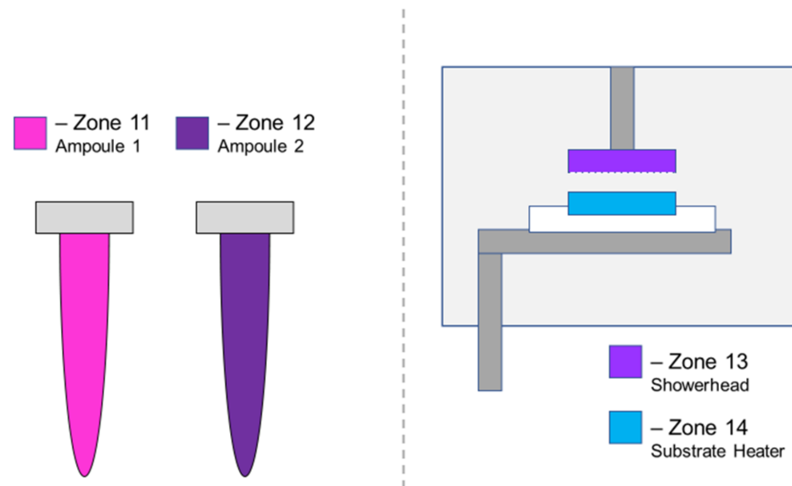

Figure 28. Heating zones 11-14.

To aid in the reduction of precursor build up inside the showerhead, it was wrapped with the heat-cable and insulated with highly conductive wrapping. Zone 13—in Figure 28—corresponds to the showerhead heating. Zone 14 is the substrate heater/holder which uses the cartridge style heaters previously described. The power to zone 13 was routed through the top flange fluid and electrical feedthrough (shown in Figure 21), while power to zone 14 came from the chamber side port 4 shown in Figure 25.

During the growths performed (details forthcoming), custom software was written to control the heating based on a PID feedback loop. Figure 29 shows the GUI heating controls and how it displayed the setpoint and actual temperature feedback.

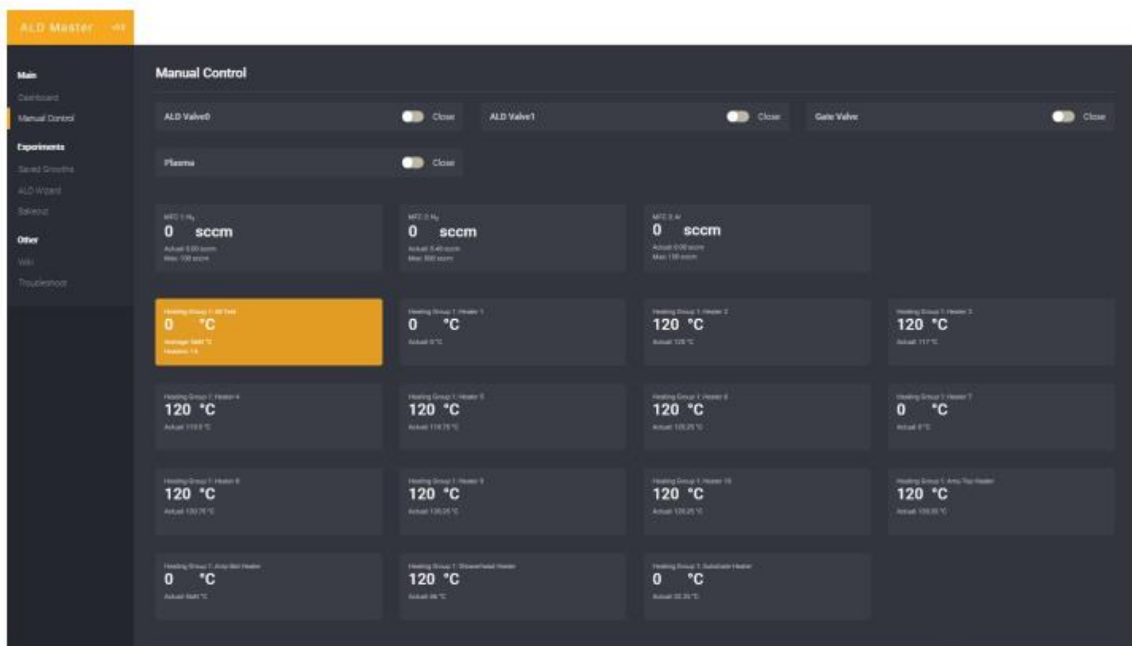

Figure 29. Graphical user interface for PEMLD heating.

2.1.7 Film Characterization

In this work, the PEMLD film growth was studied in the reactor employing *in situ* spectroscopic ellipsometry (SE) and X-ray photoelectron spectroscopy (XPS). The films were also characterized using *ex situ* contact/wetting angle.

Spectroscopic Ellipsometry

Spectroscopic ellipsometry (SE) was used for determining the thickness and optical properties of the thin-films. SE has been helpful in the study of thin-films grown through ALD, MLD and PEALD because of its non-destructive detection of growth and ability to detect changes in nominal film thickness equivalent to 0.01 monolayer (0.001 nm).[60,77,104–110] SE works by detecting the changes in the polarization of light upon reflection from a surface and comparing the data to a model.

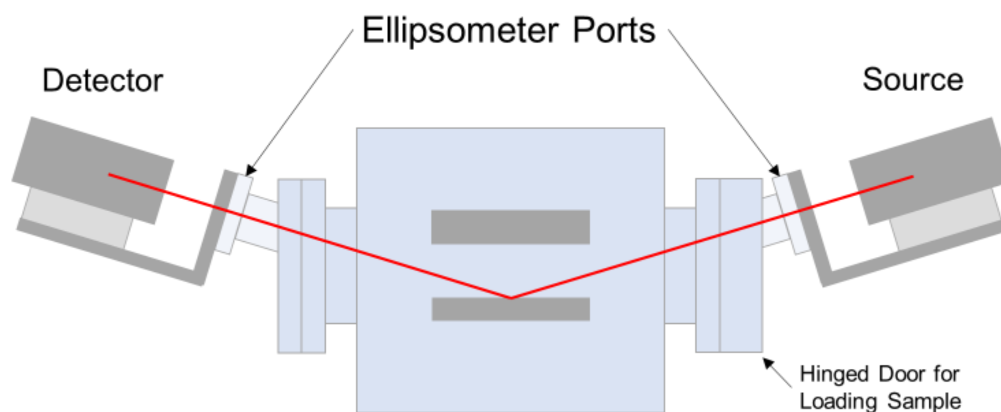

Figure 30. In Situ Ellipsometry Design.

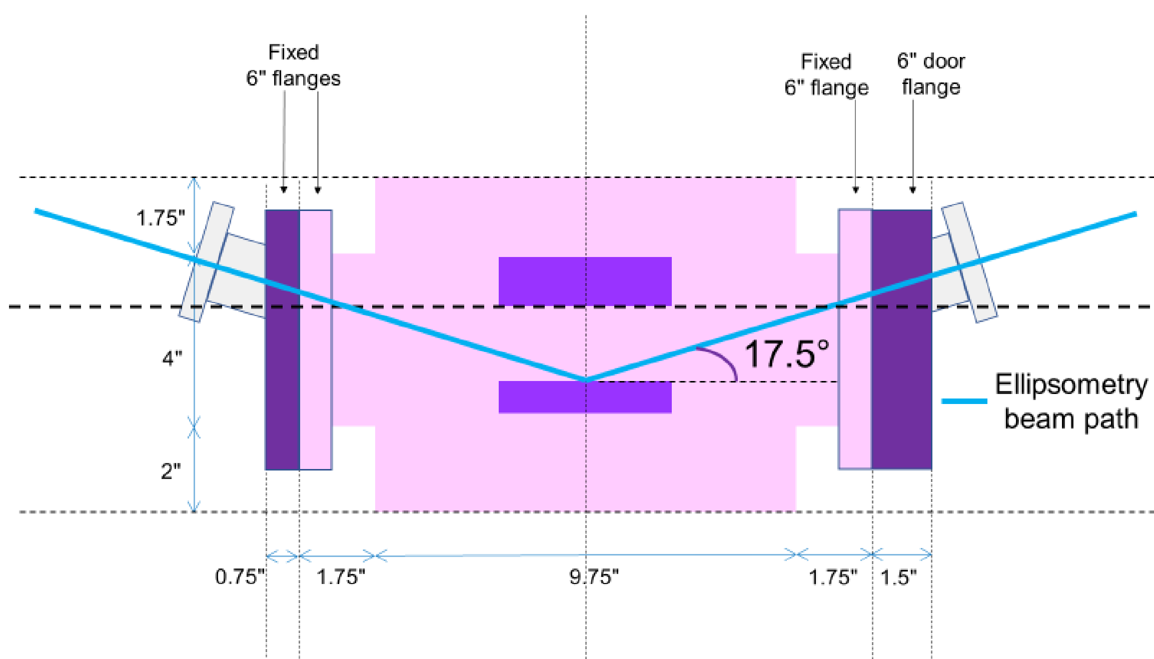

Figure 31. Ellipsometry design with beam path.

For this work, a Film Sense FS-1 Multi-Wavelength Ellipsometer was purchased and attached to the reactor chamber using custom-made ports from the UMKC Physics machinist (Figure 30 and Figure 31). The FS-1 required the ports to be mounted at an angle between 15–30° above the axis parallel to the substrate. This would correspond to

an angle of incidence (AOI) on the substrate of between 60–75º. To avoid the beam's path hitting the showerhead and keep the plate separation distance to a minimum the ports were welded at 17.5°. Because the more ideal 2-3/4" ports were located asymmetrically, the ellipsometer had to be attached to the 6" ports (ports 2 and 5 in Figure 25). Therefore, to maintain sample access, a hinged door was installed. The source was mounted to the hinged door of the chamber while the detector was attached to the opposite 6" port. Figure 32 shows the ellipsometer detector attached to a blank (left) and the ellipsometer source attached to the door (right). To align the beam of the ellipsometer, the substrate heater's z-translator can be moved up and down, and the ellipsometer mounts have a ± 2° tolerance.

Because the beam on the sample is elliptical in shape and the total beam path length varied between around 480–510 mm, larger sample sizes were preferred for accurate reading from the FS-1. Table 3 shows the relationship between beam path length and beam size at the detector and on the sample with the average intensity. The smallest sample size used in this research was 15 × 15mm.

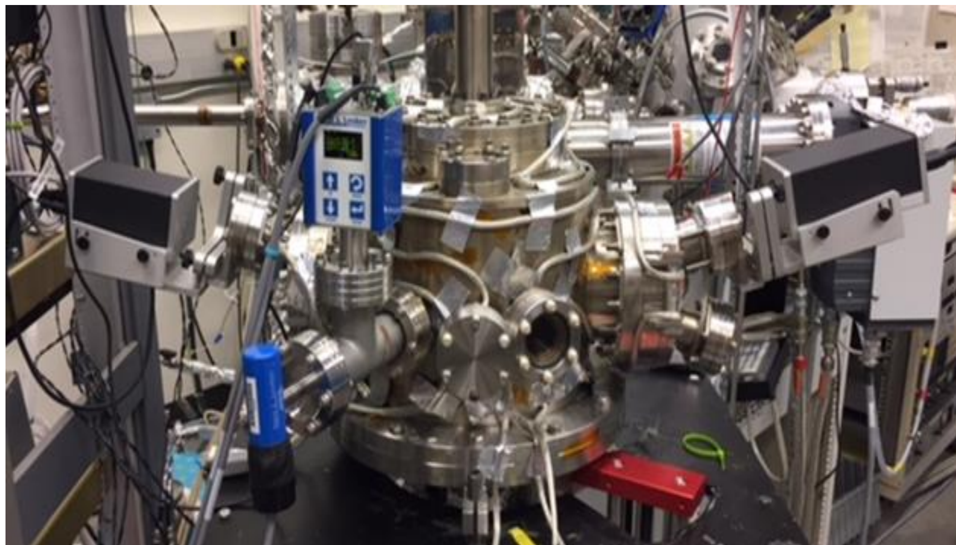

Figure 32. FS-1 Ellipsometer attached to the chamber ports.

Table 3. Table relating the beam path length to beam size at the detector and on sample and average intensity. Adapted from Film Sense FS-1 In Situ Mounting: Description and Specifications.[111]

Total Beam Path Length (mm)	Beam Diameter at Detector (mm)	Beam Size on Sample (mm) for AOI = 70º	Beam Size on Sample (mm) for AOI = 75º	Average Signal Intensity (W/m^2)
150	6	5 × 15	5 × 20	23.87
300	9	6 × 19	6 × 25	12.78
500	12	8 × 23	8 × 31	5.275
750	17	10 × 29	10 × 39	2.56
1000	20	12 × 35	12 × 46	1.37

The FS-1 ellipsometer obtains ellipsometric data at four wavelengths: blue (465 nm), green (525 nm), yellow (580 nm), and red (635 nm). The FS-1 uses the ellipsometric parameters psi (Ψ – relative amplitude change) and delta (Δ – relative phase change). R_p and R_s are the reflectivity for p- and s-polarized light. The p-plane stands parallel to the plane of incidence while the s-plane stands perpendicularly to the plane of incidence.

$$\frac{R_p}{R_s} = \tan(\Psi)e^{i\Delta}$$

Using these parameters, the FS-1 software outputs graphical data for N, C, S, P, and Intensity. These raw data output parameters correspond with the equations below.

$$N = \cos(2\Psi)$$

$$C = \sin(2\Psi)\cos(\Delta)$$

$$S = \sin(2\Psi)\sin(\Delta)$$

$$P = \sqrt{N^2 + C^2 + S^2}$$

Prior to film growth, the ellipsometer was calibrated using the ex situ table-top mount and reference wafer and again in situ with the same reference wafer. Additionally,

the FS-1 was tested against an existing J.A. Woollam Alpha-SE for thickness and index of refraction measurements of thick a-BC:H on silicon The results of the a-BC:H on Si are reported in Table 4.

Table 4. Ellipsometric comparison between the FS-1 and J.A. Woollam Alpha-SE.

Ellipsometer	Thickness (nm)	Index of Refraction
FS-1	1723.2 ± 6.7	1.9958
Other ellipsometer	1768.2 ± 23.1	1.9556

X-ray Photoemission Spectroscopy

X-ray photoemission spectroscopy is an analytical technique used for elemental analysis or chemical characterization. While the PEMLD reactor chamber was designed to attach to the existing XPS system, at the time of experimentation the XPS system was being upgraded and unavailable for *in situ* characterization. Instead the samples were sent to the user facility at the University of Nebraska-Lincoln as well as Intel Corporation for characterization.

Contact Angle Analysis

Contact angle analysis is used to determine the wettability of a surface. High contact angle relates to low surface wettability, meaning a low surface energy and low interfacial tension, Figure 33(a). Low contact angle relates to high wettability, meaning high surface energy and interfacial tension, Figure 33(b). The contact/wetting angle analysis was performed on a home-built system with a 0.2 ml static sessile drop.

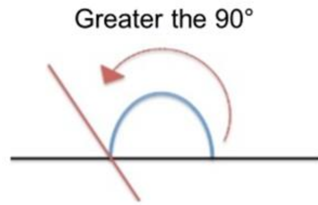

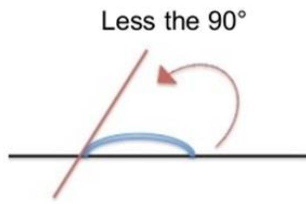

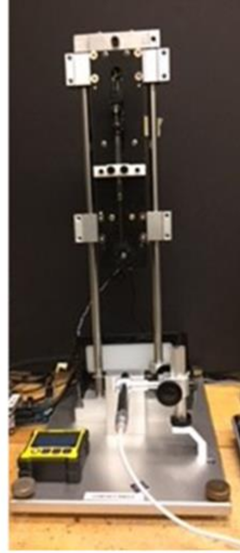

Figure 33. Surfaces with (a) high and (b) low contact angle. (c) UMKC home-built contact angle system.

CHAPTER 3

RESULTS & DISCUSSION

3.1 Introduction

In this chapter, I will discuss the experimentation and results for monolayers and multi-layers grown by plasma-enhanced molecular layer deposition (PEMLD). The first building block in the PEMLD chemistry is the deposition of a monolayer on a suitable substrate. Here, we choose the formation of thiol-carborane self-assembled monolayers (SAMs) on copper. SAM formation can be thought of as the first half cycle of the plasma-enhanced atomic layer deposition (PEALD) cycle, shown in Figure 11. Thiol–metal (typically gold) chemistry is a known methodology for growing SAMs.[61] When the thiol precursor comes into contact with the metal substrate, the more weakly bonded hydrogen atoms from S–H bonds break and form H_2 while the metal and sulfur bond.[112] Thiol-carboranes are known to undergo this same chemistry, and have been shown to form SAMs on metal substrates (copper, gold, and silver). [98,113,114] The thiol-carborane precursors used in this research were 9-thiol-m-carborane and 1,2-dithiol-o-carborane (shown in Figure 34(a) and (b) respectively) chosen for their commercial availability and symmetry. The self-assembly of the carborane precursor on the copper substrate will be discussed in section 3.2.

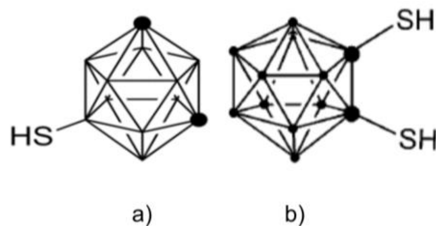

Figure 34. 9-thiol-m-carborane (a) and 1,2-dithiol-o-carborane (b).

Once the SAM has been formed, plasma treatment on the surface is used to create reactive sites. This can be thought of as a process similar to the second half cycle in PEALD, shown in Figure 11(b). We used a nitrogen plasma, which hypothetically would create amine reactive sites to allow for an amide condensation reaction. The second precursor, being a carboxylic acid, would then react with the surface via amide condensation. The amide condensation reaction is shown in Figure 35. 1-COOH-o-carborane was used as the second precursor and is shown in Figure 36. This amide condensation reaction is very similar to the only reported MLD coupling process in which acyl chloride and amine functional groups react to form an amide linkage.[69] We use a carborane-COOH derivative because it is the only amide functional group currently available, even though carborane-COCl is known to exist.

Figure 35. Amide condensation reaction.

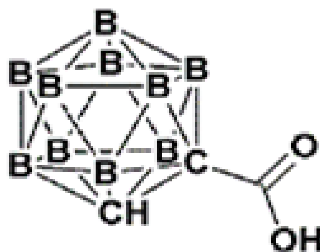

Figure 36. 1-COOH-o-carborane.

To grow subsequent layers, plasma treatment and amide condensation reactions would be cycled. A multi-layer, multi-cycle PEMLD growth scheme with layers of 1,2-dithiol-o-carborane, nitrogen plasma, and 1-COOH-o-carborane is discussed in section 3.5. This multi-layer, multi-cycle scheme is what we propose as a novel plasma-enhanced molecular layer deposition scheme for boron carbide.

With each step on the path towards multi-layer, multi-cycle PEMLD, characterization of the films by means of X-ray photoelectron spectroscopy (XPS), contact angle analysis, and spectroscopic ellipsometry will be discussed.

3.2 Experimental Details

3.2.1 Substrate Preparation

The PEMLD growth was performed on 15 x 15 mm silicon substrates onto which an adhesion layer of evaporated chromium and substrate layer of copper were deposited. Prior to metal evaporation, the silicon substrates were cleaned ultrasonically in acetone for 15 minutes. The substrates were removed from the acetone, allowed to dry, then transferred into a 3:1 piranha (sulfuric acid, H_2SO_4: hydrogen peroxide, H_2O_2) bath for 15 minutes. The substrates were then rinsed with deionized water and dried using Marangoni drying (isopropanol vapor drying with nitrogen carrier gas).

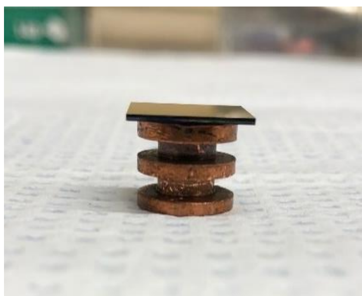

Figure 37. Silicon coupon attached to puck prior to evaporation.

The silicon substrate needed to be attached to a sample puck in order to transfer *in situ* between metal evaporation and the PEMLD chamber. The substrate was attached to the sample puck with double-sided high-temperature tape and loaded into the evaporation chamber load lock (Figure 37). The load lock was then pumped down until a base pressure of less than 5.0×10^{-6} Torr was reached. A 5–10 nm layer of chromium was first deposited onto the surface of the silicon to act as an adhesion layer, followed by 100–125 nm of copper. The deposition rates for the chromium and copper were monitored using a MAXTEK TM-400 thickness monitor and quartz crystal microbalance (QCM), which was positioned above the metal source. Once the deposition rate stabilized, the QCM would be retracted and the substrate would be positioned above the source. The metal exposure time was pre-calculated using the deposition rate and desired thicknesses. Once the copper was evaporated onto the substrate, the puck was transferred to the PEMLD chamber.

3.1.2 Chamber Preparation

To reduce contamination, the chamber was kept under ultra-high vacuum ($<10^{-6}$ Torr) and heated to 125 °C when not in use. Along with the pumping and heating on the chamber for pre-growth bake-out, the precursor ampoules were pre-baked and then loaded in a nitrogen atmosphere within the glove box. Once attached to the chamber, the head-space of the ampoules was pumped down with the Welch and cryo-pump. The precursors were then heated to a predetermined temperature for precursor sublimation. To reduce/possibly eliminate precursor condensation, the ampoule, ampoule-to-chamber plumbing, and showerhead were also heated to this temperature. Once the temperature of

the chamber components stabilized, the sample puck was transferred into the chamber and onto the substrate heater. The sample puck and substrate heater were then heated to the predetermined temperature and allowed to stabilize before the SAM/PEMLD growth was started.

3.2 Self-Assembled Monolayer Growth

3.2.1 9-Thiol-m-carborane on Copper

To determine the self-saturative assembly of the thiol-based carborane derivatives on the copper substrate, the copper substrates were dosed for times of 10 s, 60 s, and 15 min with 9-thiol-m-carborane (samples A07, A11, and A01 respectively). The 9-thiol-m-carborane was sourced from Sigma-Aldrich. In these tests, the substrate was kept at ambient temperature while the precursor was sublimed at 175 °C. The chamber ($< 10^{-5}$ Torr pre-growth) was brought to 0.01 Torr with precursor vapor pressure and left for the dose time before being pumped down.

Evidence of monolayer formation can be analyzed using XPS characterization. The following elemental peaks are consistent with a monolayer formation of the carborane precursor on the copper surface: Cu 2p (~933 eV), O 1s (~531 eV), C 1s (~284 eV), B 1s (~189 eV), and S 2p (~163 eV).

The XPS survey scan of sample A11—60 s dose—can be seen in Figure 38. The Cu 2p peak is seen as expected, however the peak cannot be broken down beyond the copper–metal monolayer formation. The O 1s peak corresponds with oxygen contamination of the copper surface. The C 1s spectrum is composed of two main components labeled C_B and C_H at energies 286.4 ± 0.3 and 284.6 ± 0.3 eV, respectively,

which correlate to carbon atoms from carborane clusters and hydrocarbons from surface contamination and a minor peak at 288.0 ± 0.2 from C–O (Figure 39). The B 1s peak corresponds with the different icosahedral boron chemistries (depending on location in icosahedron) but tend to overlap. The S 2p peak is as expected for thiol-carborane bound to the copper substrate but the analysis was unable to distinguish any bonding details.[98]

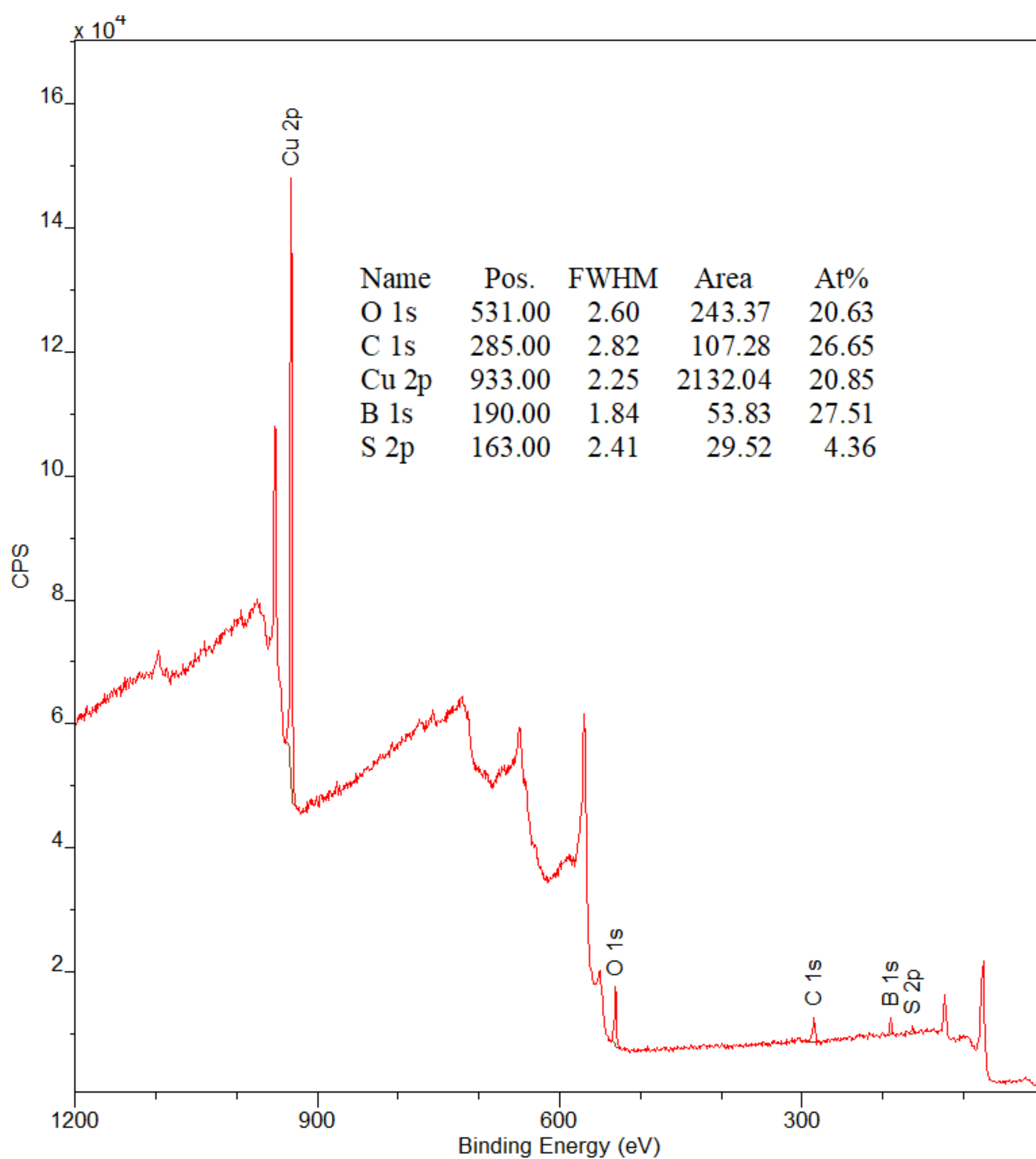

Figure 38. XPS survey scan of sample A11: 60 s dose of 9-thiol-m-carborane on copper at 0.01 Torr, ambient temperature.

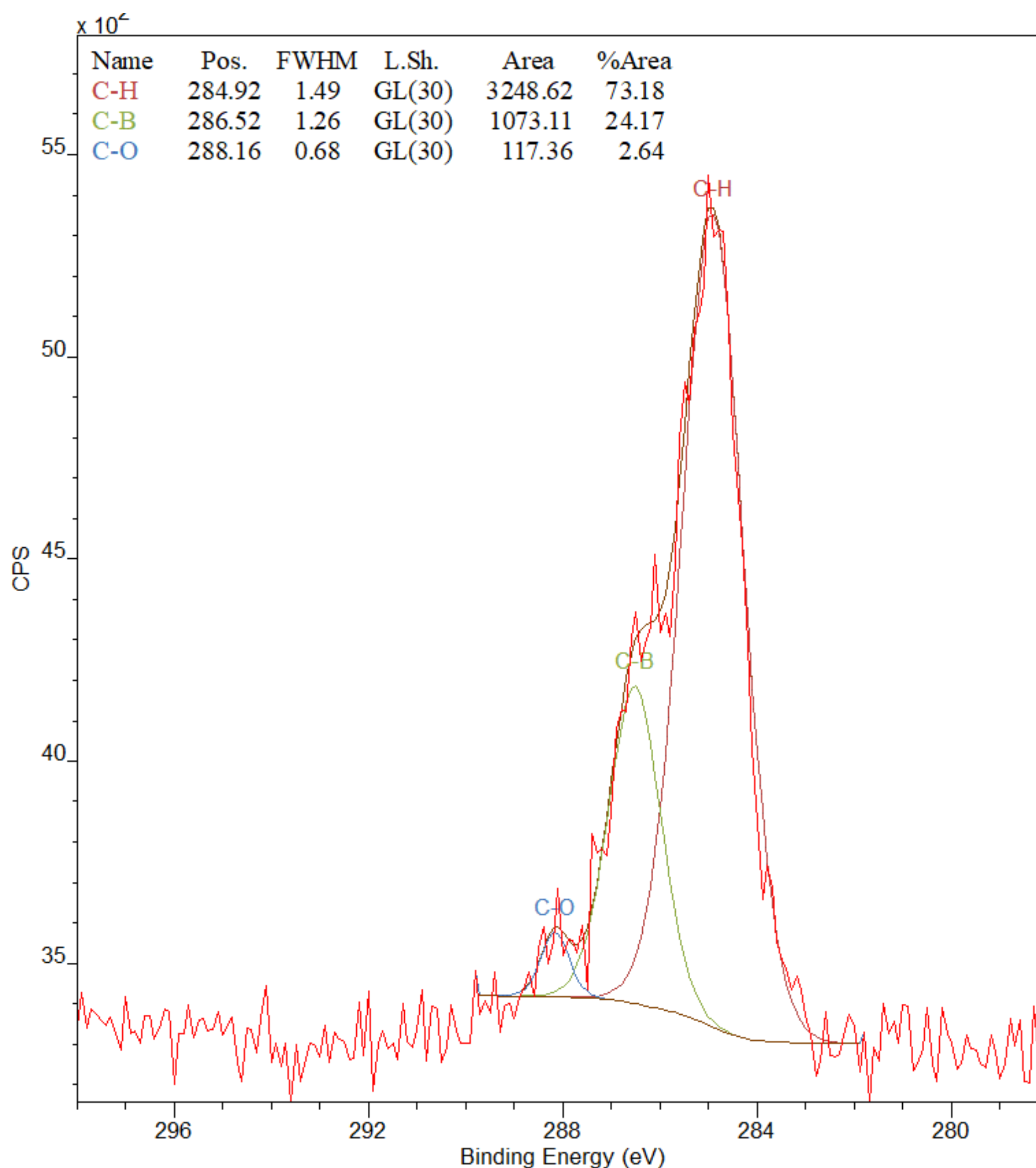

Figure 39. XPS C 1s spectrum of sample A11: 60 s dose of 9-thiol-m-carborane on copper at 0.01 Torr, substrate temperature-ambient, precursor temperature-175°C.

The XPS characterization results for the 10 and 60-second growths highly varied from the 15-minute growth. From the breakdown of the XPS raw data and ratio of elements in Table 5 and Table 6, the dosing tests suggest that for the 10 and 60-second tests the boron to copper ratio is fairly consistent with monolayer formation from the literature (~1–3).[115–117] The B/C_B ratio is also nearest its expected value of 5 for the 60-

second dose. The 15 minutes growth appears to yield more than a monolayer due to there being no discernable sulfur peak and a weaker although still observable Cu peak.

Table 5. XPS raw data from survey scans showing binding energy (eV) and atomic percentages (%) of elements.

Sample	Cu	O	C	B	S
A07, 10 s	932.8 eV 9.11 %	530.5 eV 7.57 %	284.6 eV 35.89 %	189.4 eV 32.48 %	163.0 eV 14.94 %
A11, 60 s	932.6 eV 20.85 %	530.4 eV 20.63 %	285.0 eV 26.65 %	189.8 eV 27.51 %	162.7 eV 4.36 %
A01, 15 min	932.0 eV 9.96 %	530.1 eV 9.76 %	285.2 eV 22.15 %	189.9 eV 60.19 %	α

α – no discernable peak observed

Table 6. XPS ratio of elements calculated from atomic percentages. Boron is first set to 10, representing the 10 boron atoms of the icosahedral carborane precursor, then the other element ratios are calculated. C_B is approximated by subtracting the C_H peak area from the total C peak area.

Sample	B	Cu	O	C_B	S	B/Cu	B/C_B	B/S
A07, 10 s	10	2.8	2.3	2.8	4.6	3.6	3.6	2.2
A11, 60 s	10	7.6	7.5	2.4	1.6	1.3	4.2	6.3
A01, 15 min	10	1.7	1.6	0.9	n/a	5.9	11.1	n/a

3.2.2 1,2-Dithiol-o-carborane on Copper

To further investigate the formation of monolayer SAM's, we used *in situ* ellipsometry. The first reaction studied using the *in situ* ellipsometry was 1,2-dithiol-o-carborane on a copper substrate hypothesized in Figure 40. The 1,2-dithiol-o-carborane was sourced from Sigma- Aldrich. To try and observe monolayer 1,2-dithiol-o-carborane growth, the evaporated copper substrate was transferred to the PEMLD reactor chamber

and into the holder. A baseline reading for the copper was modeled, then with dynamic data acquisition running, the chamber was pumped down and the precursor heated to 175 °C. The precursor ampoule was then opened until the reactor chamber was filled to 0.01 Torr with precursor vapor and then closed. Once the chamber pressure was achieved, the substrate was left exposed to the precursor vapor for 60 minutes. The chamber was then pumped down and monitored for an additional 115 minutes.

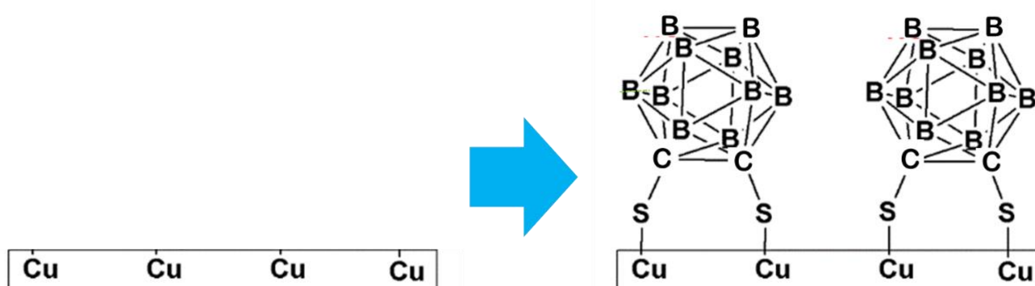

Figure 40. Theorized 1,2-dithiol-o-carborane formation of SAM on copper substrate.

Figure 41 shows the *in situ* ellipsometry "S" parameter raw data and model thickness versus time for the total duration of the 1,2-dithiol-o-carborane growth. The FS-1 software allows growth recipes to be input and used to model thickness during deposition. Prior to growth, the copper substrate is measured and its index of refraction (*n*) and extinction coefficient (*k*) values are used to model the surface. Typically, in spectroscopic ellipsometry, the *n* & *k* values can be used to model a layer's thickness. However, the copper substrate's measured *n* and *k* values do not always match the textbook values for copper, so the substrate is treated as a pseudo-copper substrate layer. The carborane SAM layer is measured as a Cauchy film because its fit is unknown. The raw data suggests a rapid growth regime occurring from the time of dose start to about 3 minutes. Figure 42 shows the rapid growth regime with the calculated thickness from the model layer to be around 3–4 nm. The leveling off from the rapid growth regime and

calculated thickness appear to be consistent with more than a monolayer being formed. This conclusion is consistent with the dosing time tests with samples A07, A11, and A01 which showed the B:Cu ratio increases with time. The growth continues gradually even after the precursor was pumped away and appears to level off at around 90 minutes at 5–6 nm. The additional growth could be the result of more than monolayer formation or from the possible copper etching and subsequent re-reaction cause by the SH groups in the presence of oxygen.[98]

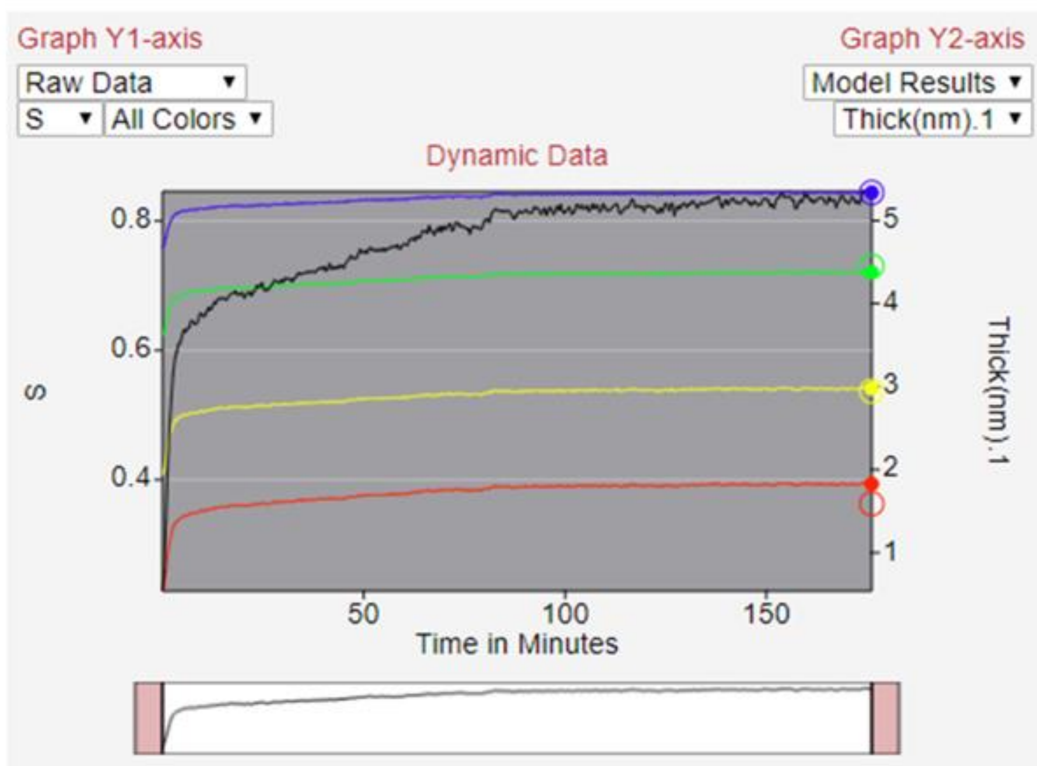

Figure 41. Full process of self-saturative 1,2-dithiol-o-carborane growth on copper substrate. The left y-axis represents the ellipsometry raw S parameter data at the four wavelengths (red, yellow, green and blue), whereas the right represents the modeled thickness (black). The modeled thickness uses a pseudo-copper substrate layer with a Cauchy growth layer. The ampoule was heated to 175 ºC and chamber pressure raised to 0.01 Torr before the ampoule was closed. The total dose time was 60 minutes with the substrate temperature maintained at 125 ºC.

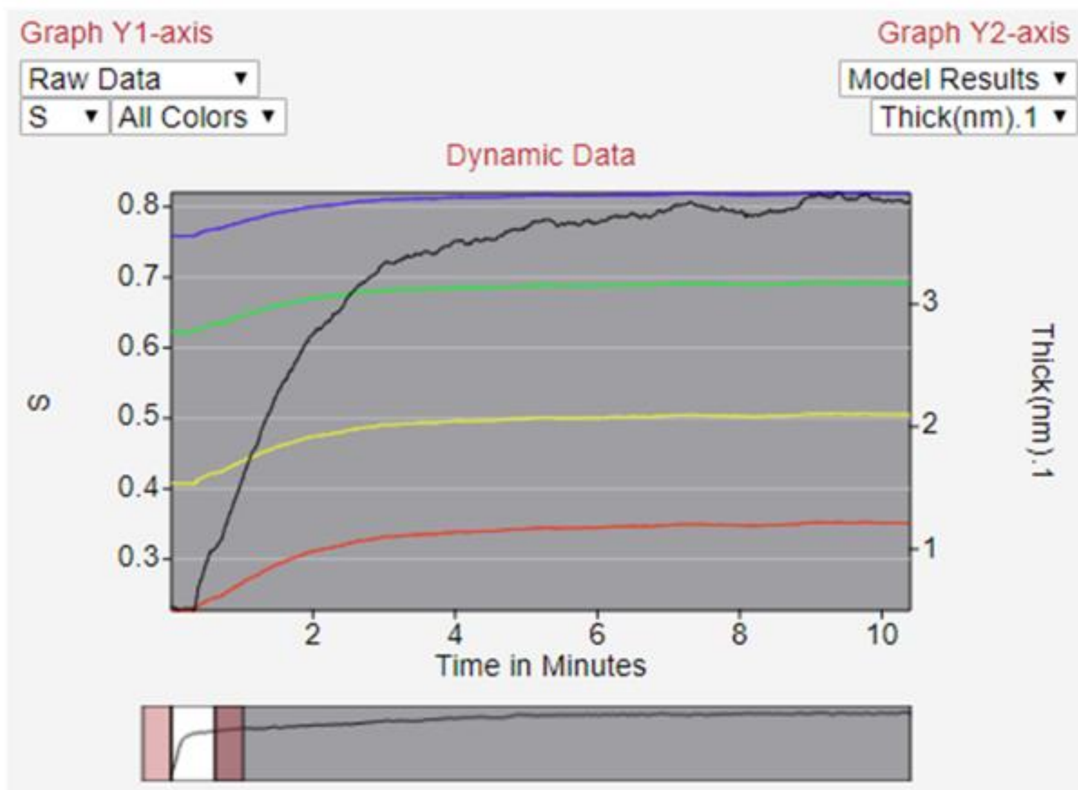

Figure 42. Rapid growth region of self-saturative 1,2-dithiol-o-carborane on copper substrate.

XPS characterization of 1,2-dithiol-o-carborane SAMs was performed, and a scan from sample A13 is shown in Figure 43 with the ratio of elements summarized in Table 7. Sample A13 was a copper sputtered substrate exposed to 1,2-dithiol-o-carborane vapor for 60 s at 0.01 Torr and ambient temperature. The XPS characterization is consistent with the formation of 1,2-dithiol-o-carborane on the copper substrate. The only difference in the characterization of A13 and the 9-thiol-m-carborane films is that with 1,2-dithiol-o-carborane there should be a ~10:2 ratio of boron to sulfur versus 10:1 with 9-thiol-m-carborane. In the case of A13, the boron to sulfur ratio ended up being 10:2.8 close to the expected value 10:2.

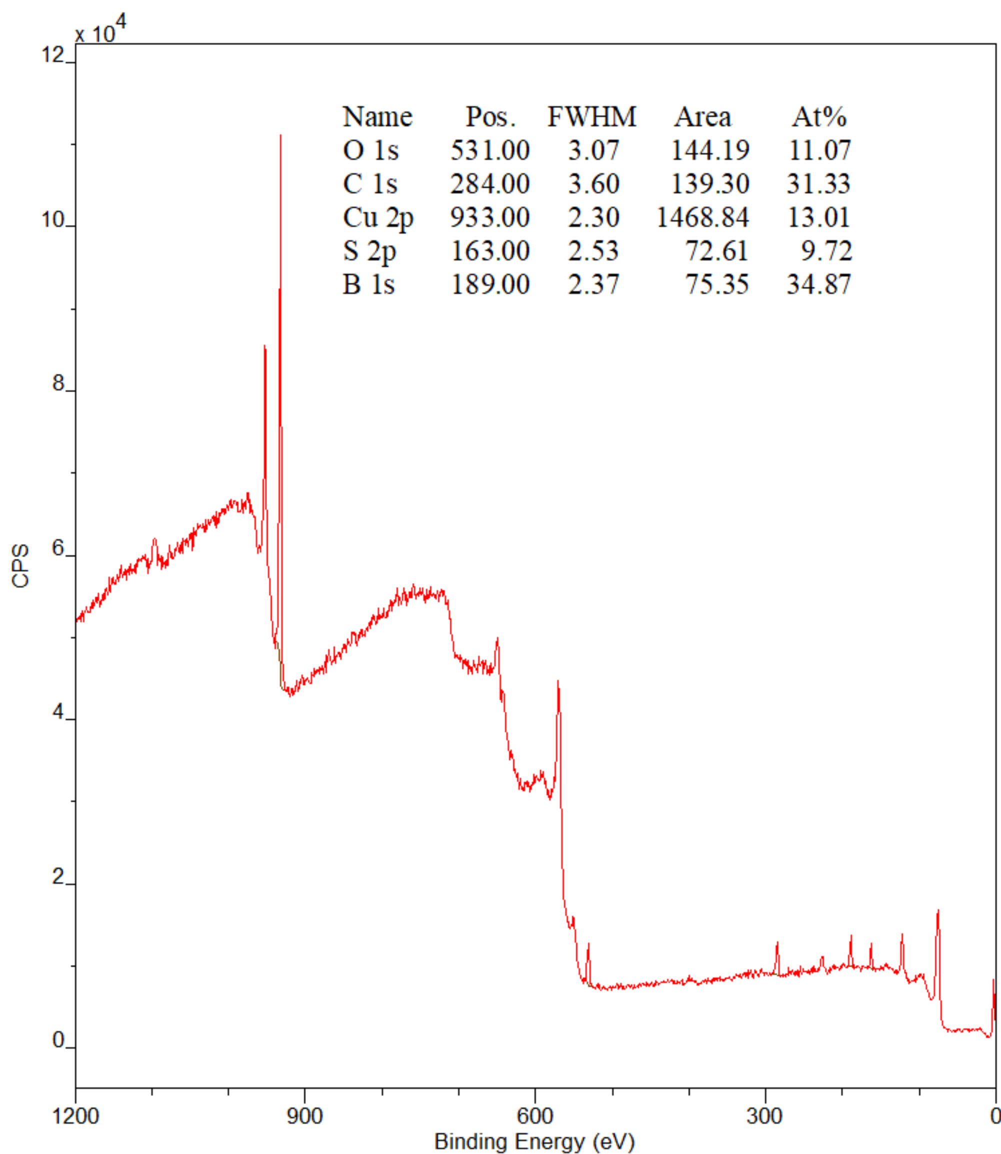

Figure 43. XPS characterization data for sample A13: 60 s dose, 0.01 Torr, substrate temperature-ambient, precursor temperature-175 ºC, 1,2-dithiol-o-carborane on copper.

Table 7. XPS ratio of elements calculated from the atomic percentages for sample A13.

Sample	B	Cu	O	C_B	S	B/Cu	B/C_B	B/S
A13	10	3.7	3.2	2.2	2.8	2.7	4.5	3.6

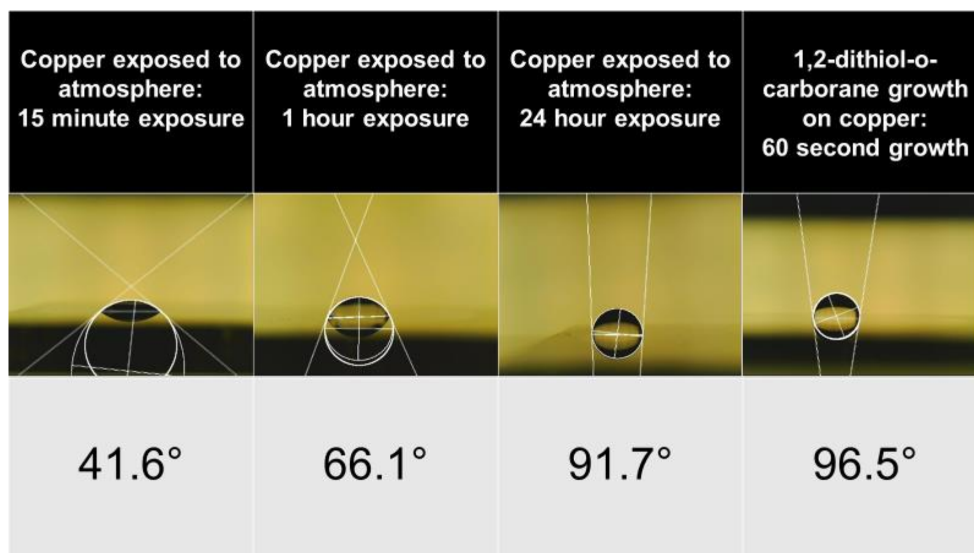

Figure 44. Contact angle measurements comparing levels of oxidation and SAM growth on copper.

Figure 44 shows contact angle data from the 60 s dose of 1,2-dithiol-o-carborane compared with contact angle data from copper at different stages of oxidation. The contact angle measurement for the 1,2-dithiol-o-carborane film was taken immediately post deposition. The SAM growth displayed different contact angle data measurements when compared with both copper and oxidized copper. This suggests a surface change and is consistent with film formation with a 60 s dose.

3.3 SAM and Plasma

Once the formation of the 1,2-dithiol-o-carborane SAM was achieved, the next step for the PEMLD process is the plasma surface modifications of the carborane surface to create reactive sites. The choice of the plasma gas affects the type of precursor that can react for the next layer. Because we desire to use amide coupling chemistry—a carboxylic acid derivative bonding to an amine—nitrogen was chosen as the plasma gas

to functionalize the surface with NH_2 groups. Hypothesized plasma surface modifications are shown in Figure 45.

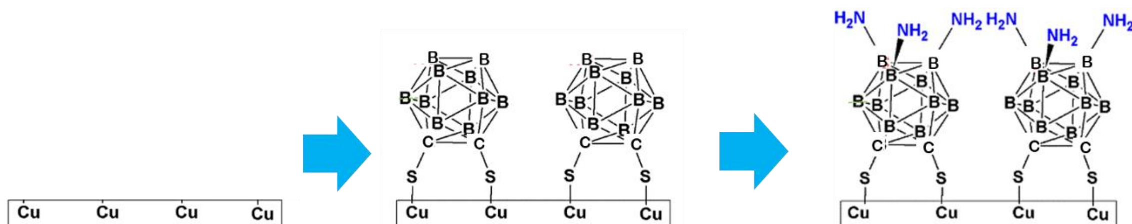

Figure 45. Hypothesized nitrogen plasma surface modifications of 1,2-dithiol-o-carborane.

In situ ellipsometry was used to observe SAM formation and plasma surface modification (sample F000). An initial dose of 1,2-dithiol-o-carborane was exposed to copper for 1 min at 0.01 Torr. Post-SAM formation, the sample F000 was plasma treated to create reactive sites on its surface. To achieve a dynamic plasma, the chamber was brought to 200 mTorr with nitrogen flowing at 65 sccm with the Welch pump pumping on the chamber. Once the pressure stabilized, ellipsometry data collection was started and a plasma was generated at 50 W. The plasma dose was initiated at 2 min, 15 seconds with a duration of one minute. Figure 46 shows the ellipsometry data from the nitrogen plasma step on the 1,2-dithiol-o-carborane film (F000).

XPS data from a similarly grown and plasma treated sample (A26)—Figure 47—shows the presence of nitrogen on the surface. The XPS atomic percentages of elements from A26 can be found in Table 8. The boron to nitrogen ratio of 10:3 indicates close to 3 nitrogen atoms per icosahedron and suggests a high surface saturation of nitrogen groups. The boron to copper ratio of 9.9 is higher compared to the 1–3 range found in the literature and in previous samples. The boron to sulfur range at 9.8 was also higher than

the expected 5. This suggests the possibility of unintentional carborane bonding in the presence of the plasma due to residual carborane precursor in the chamber at the time of the plasma.

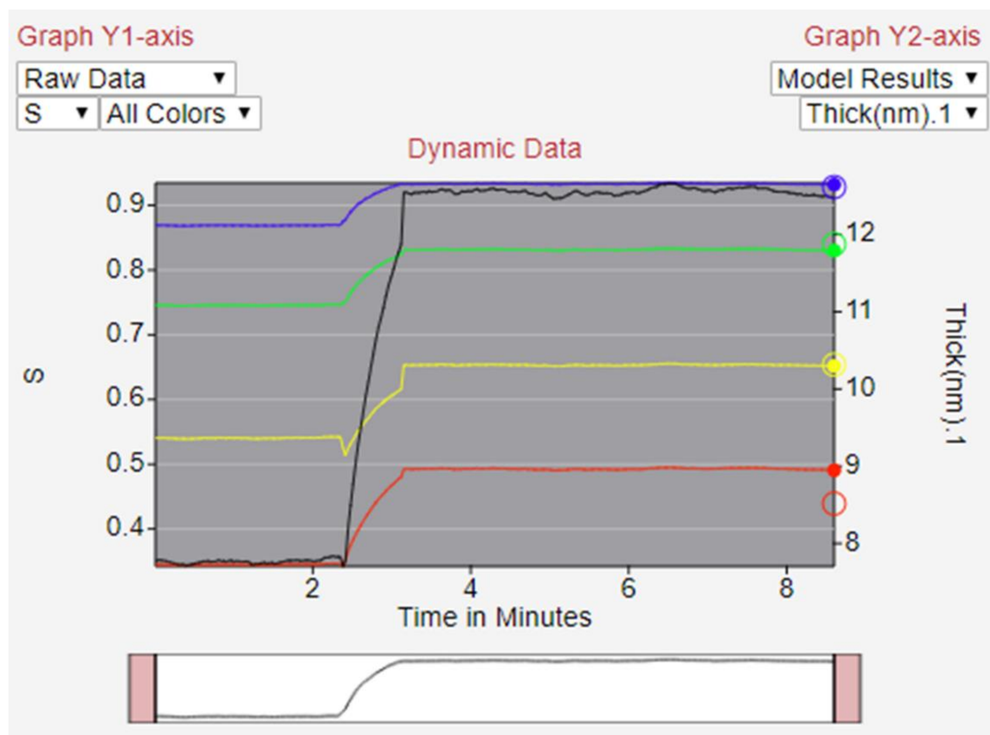

Figure 46. Nitrogen plasma dose on 1,2-dithiol-o-carborane film F000. Plasma conditions: power=50 W, N_2 flow=65 sccm, 1 min dose.

Contact angle measurements also suggest surface modification from the plasma. Figure 48 shows the pre-plasma contact angle for the SAM surface to be ~96.5° and that for the post-plasma treatment film to be less than 10°. This change in the surface from hydrophilic to hydrophobic indicates that the nitrogen plasma is in fact modifying the surface. The contact angle post-plasma treatment is also quite different from the contact angle for bare copper at 41.6°, shown in Figure 44. The XPS data which suggests a still intact carborane film with the addition of nitrogen surface species and ellipsometry data

with a quantitative change in surface properties suggests the plasma does in fact modify the surface chemistry.

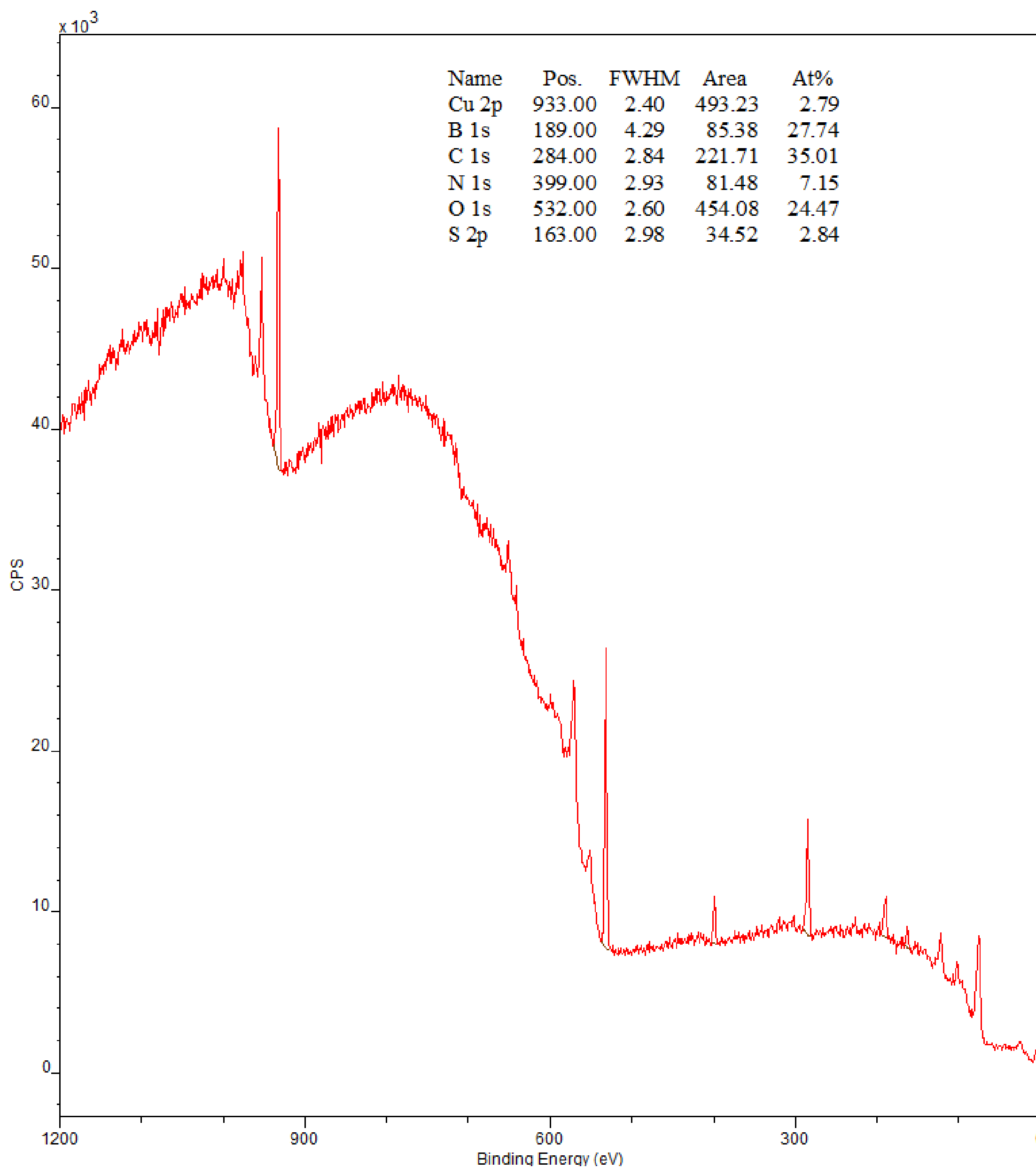

Figure 47. XPS characterization of 1,2-dithiol-o-carborane film with nitrogen plasma treatment, A26. Plasma conditions: power=10 W, N_2 flow=100 sccm, 1 min dose.

Table 8. XPS binding energies (eV), atomic percentages (%), and ratio of elements for sample A26.

Sample	Cu	O	N	C_B	B	S	B/Cu	B/C_B	B/S
A26	932.9	531.8	399.3	286.3	189.3	162.8	-	-	-
	2.79	24.47	7.15	8.75	27.74	2.84	-	-	-
	1.0	8.8	2.6	3.2	10	1.0	10	3.1	10

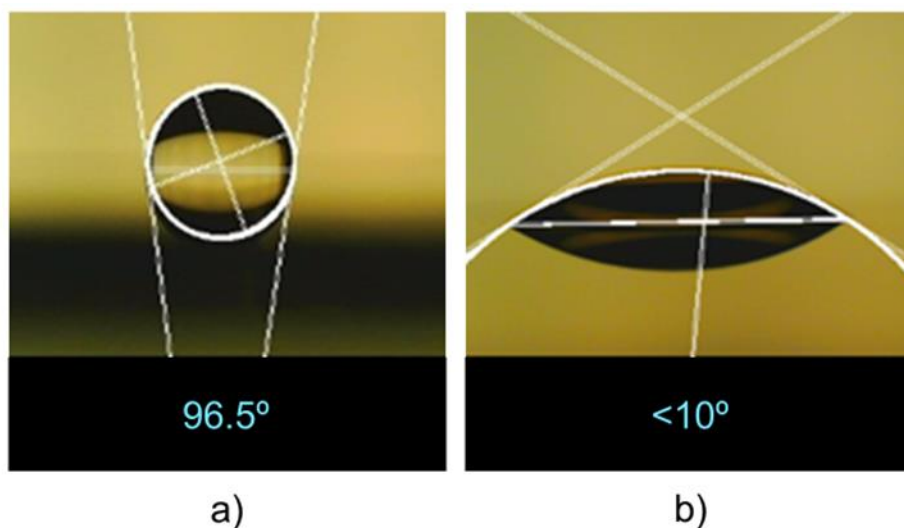

Figure 48.(a) Contact angle for pre- and (b) post-N_2-plasma 1,2-dithiol-o-carborane film.

3.4 Multi-Layer PEMLD

The purpose of the surface modification of the SAM was to enable the possibility of amide condensation via carboxylic acid (1-COOH-o-carborane). The 1-COOH-o-carborane was sourced from Twelfth Vertex. Figure 49 shows the hypothesized amide condensation for the multi-layer growth using PEMLD.

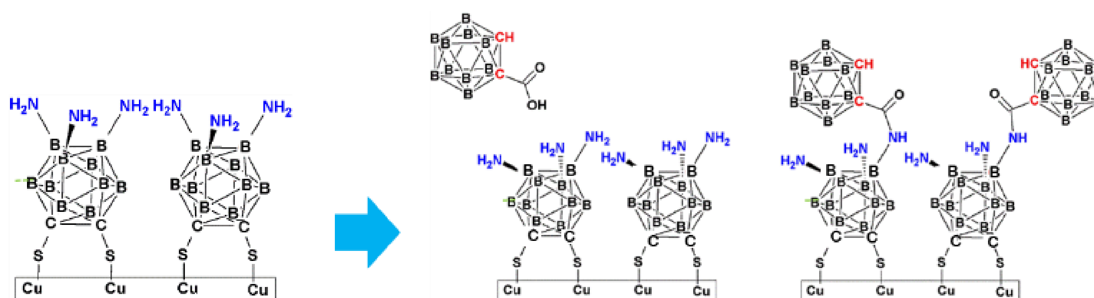

Figure 49. Hypothesized multi-layer growth using 1-COOH-o-carborane on plasma-treated 1,2-dithiol-o-carborane film.

Figure 50 shows the timing for the precursor doses, plasma generation, and pumping cycles for the sample (F003). Ampoule 1 corresponds with the 1,2-dithiol-o-carborane precursor source, while ampoule 2 was filled with the 1-COOH-o-carborane derivative. Prior to growth, the chamber was pumped down to $< 10^{-6}$ Torr. Ampoule 1 was then opened to the chamber until the chamber pressure rose to 0.440 Torr. The sample was left exposed for 1 minute. The chamber was then pumped down, purged, and treated with a nitrogen plasma. The plasma dose conditions were a dose of 1 minute at 50 W with a chamber pressure of 0.2 Torr which corresponded with a nitrogen flow rate of 72 sccm. The chamber was then pumped down to $< 10^{-6}$ Torr. Ampoule 2 was then opened to the chamber until the chamber pressure reached 0.102 Torr and the sample was left exposed for 1 minute.

Figure 51 shows the raw data from the *in situ* ellipsometry for the F003 growth. The SAM formation and plasma exposure are clearly seen at the 12- and 26-minute marks, while there is no clear amide condensation (introduced at 40 minutes).

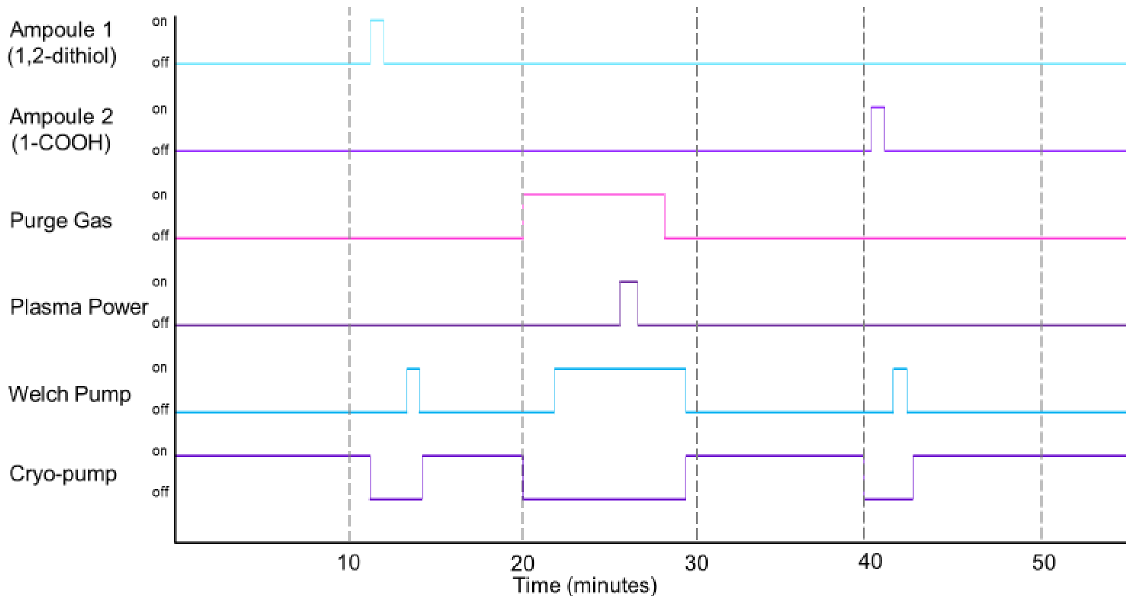

Figure 50. PEMLD process flow for multi-layer growth F003.

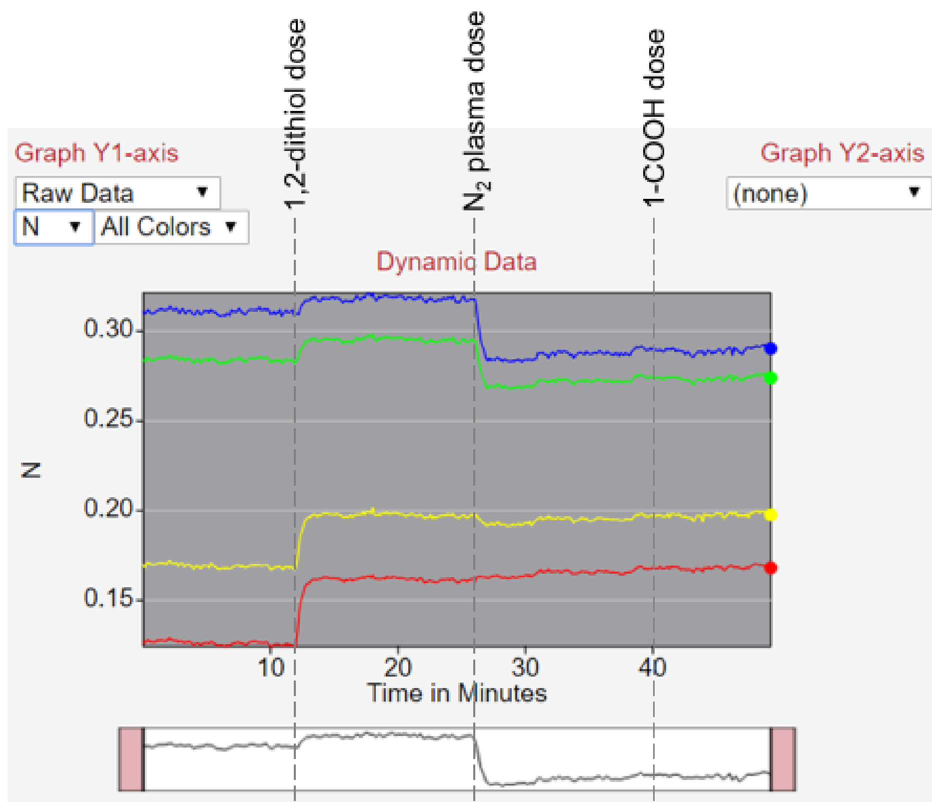

Figure 51. In situ ellipsometry raw data for multi-layer growth F003.1,2-dithiol-o-carborane dose at 12 min for 1 min at 440 mTorr and precursor temperature-175 ºC, substrate temperature-175°C. Nitrogen plasma dose at 26 min for 1 min at 200 mTorr, 72 sccm and 50 W. 1-COOH-o-carborane dose at 40 min for 1 min at 102 mTorr and precursor temperature-175 ºC.

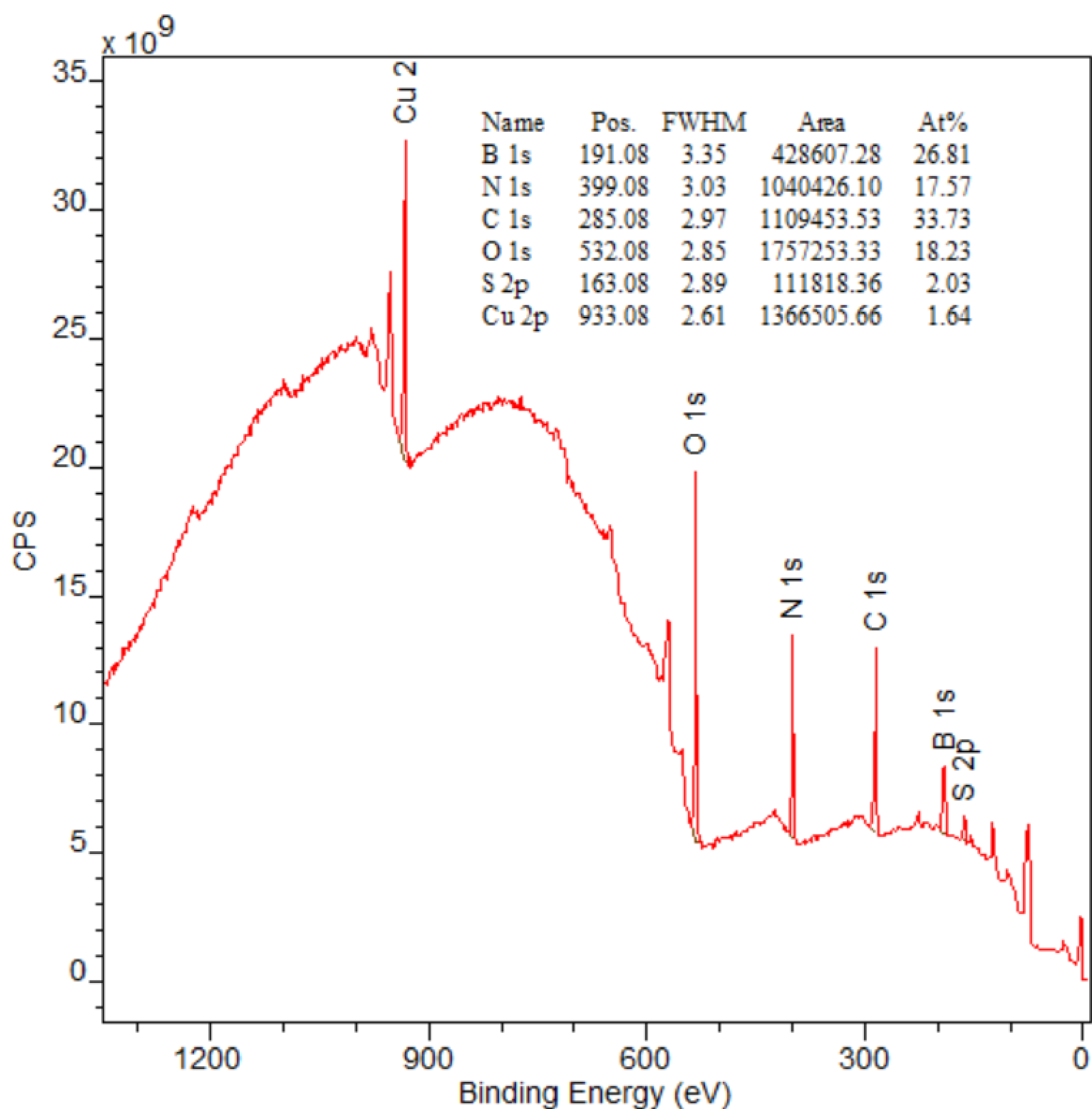

Figure 52. XPS characterization of sample F003 which had layers: copper, 1,2-dithiol-o-carborane, nitrogen plasma, and 1-COOH-o-carborane.

XPS characterization was performed on sample F003 (Figure 52), and the results are shown in Table 9. There was no significant quantitative nor qualitative change in the XPS data from A26 and F003. From the SE data, there was also no significant qualitative change in the film, so it is possible that conditions need to be further dialed in (temperature, pressure, time, etc.).

Table 9. XPS binding energy (eV), atomic percentages (%), and ratio of elements for sample F003.

Sample	Cu	O	N	C_B	B	S	B/Cu	B/C_B	B/S
	932.8	531.9	398.5	286.3	190.5	162.7	-	-	-
F003	1.64	18.23	17.57	6.07	26.81	2.03	-	-	-
	0.6	6.8	6.6	2.3	10	0.8	16.7	4.3	12.5

3.5 Multi-Layer, Multi-Cycle PEMLD

The same growth chemistry was performed in a multi-layer, multi-cycle scheme despite sample characterization not conclusively demonstrating amide condensation. Figure 53 shows the process flow for the multi-layer, multi-cycle PEMLD growth F006. Ampoule 1 corresponds with the 1,2-dithiol-o-carborane precursor source, while ampoule 2 was filled with the 1-COOH-o-carborane. Five full plasma/precursor cycles were performed on sample F006. Figure 54 and Figure 55 shows the raw *in situ* ellipsometry data for the multi-layer, multi-cycle growth F006. Prior to growth, the chamber was pumped down to $< 10^{-6}$ Torr. Table 10 describes the detailed process flow for the F006 PEMLD growth.

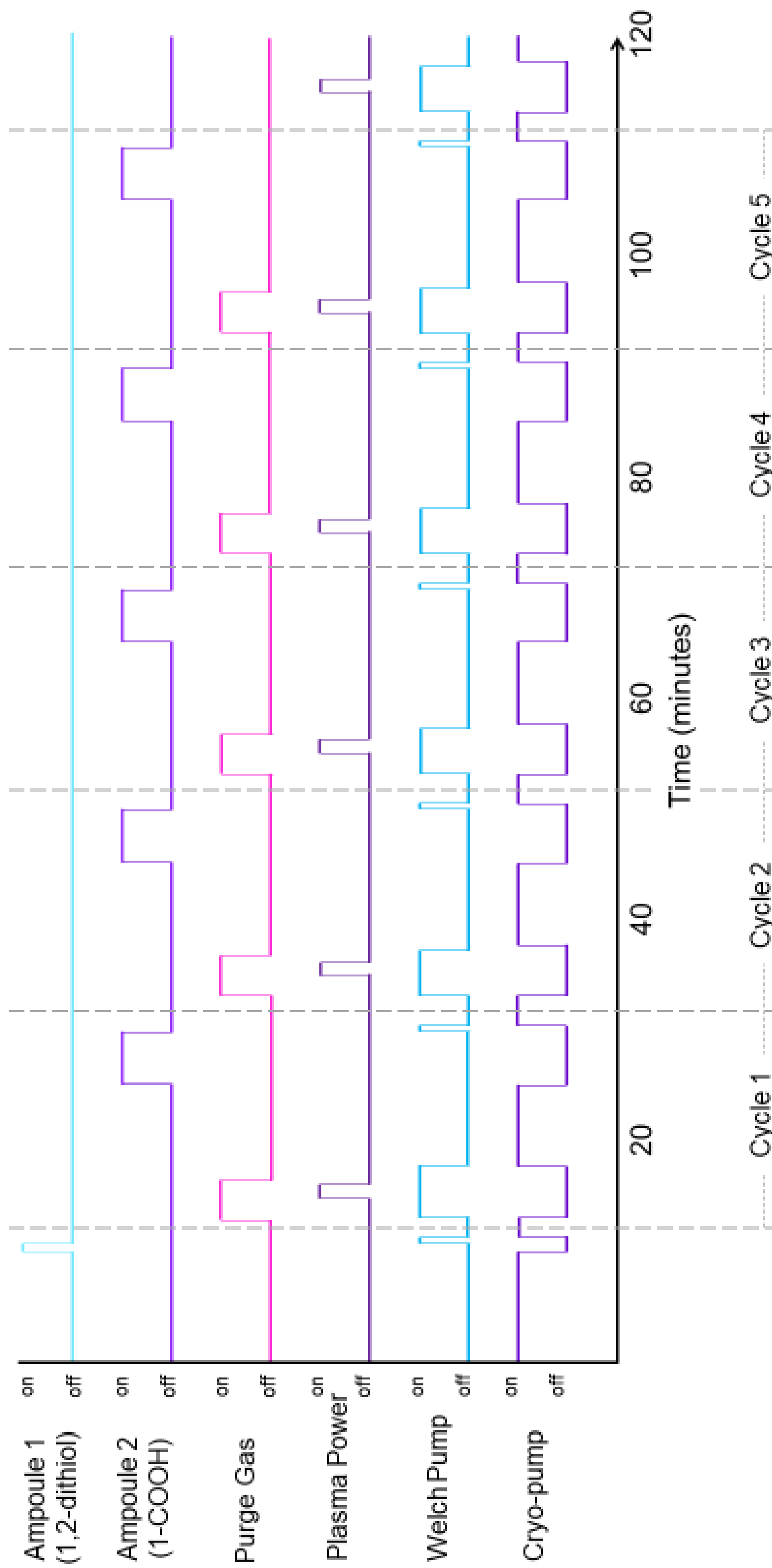

Figure 53. Multi-layer, multi-cycle growth of F006.

Table 10. F006 detailed process flow for multi-layer-multi-cycle growth.

SAM			
1,2-dithiol-o-carborane			
ampoule open		10 min, 0 s	
Dose		1 min	
Pressure		128 mTorr	
Cycle 1			
N_2 plasma		1-COOH-o-carborane	
N_2 flow start	13 min, 30 s	ampoule open	25 min, 0 s
sccm	68	dose	5 min
pressure	204 mTorr	pressure	167 mTorr
plasma on	15 min, 0 s		
dose	1 min		
Cycle 2			
N_2 plasma		1-COOH-o-carborane	
N_2 flow start	3 min, 30 s	ampoule open	45 min, 0 s
sccm	66	dose	5 min
pressure	199 mTorr	pressure	145 mTorr
plasma on	35 min, 0 s		
dose	1 min		
Cycle 3			
N_2 plasma		1-COOH-o-carborane	
N_2 flow start	53 min, 30 s	ampoule open	65 min, 0 s
sccm	67	dose	5 min
pressure	203 mTorr	pressure	177 mTorr
plasma on	55 min, 0 s		
dose	1 min		
Cycle 4			
N_2 plasma		1-COOH-o-carborane	
N_2 flow start	73 min, 30 s	ampoule open	85 min, 0 s
sccm	67	dose	5 min
pressure	203 mTorr	pressure	97 mTorr
plasma on	75 min, 0 s		
dose	1 min		
Cycle 5			
N_2 plasma		1-COOH-o-carborane	
N_2 flow start	93 min, 30 s	ampoule open	105 min, 0 s
sccm	66	dose	5 min
pressure	200 mTorr	pressure	92 mTorr
plasma on	95 min, 0 s		
dose	1 min		

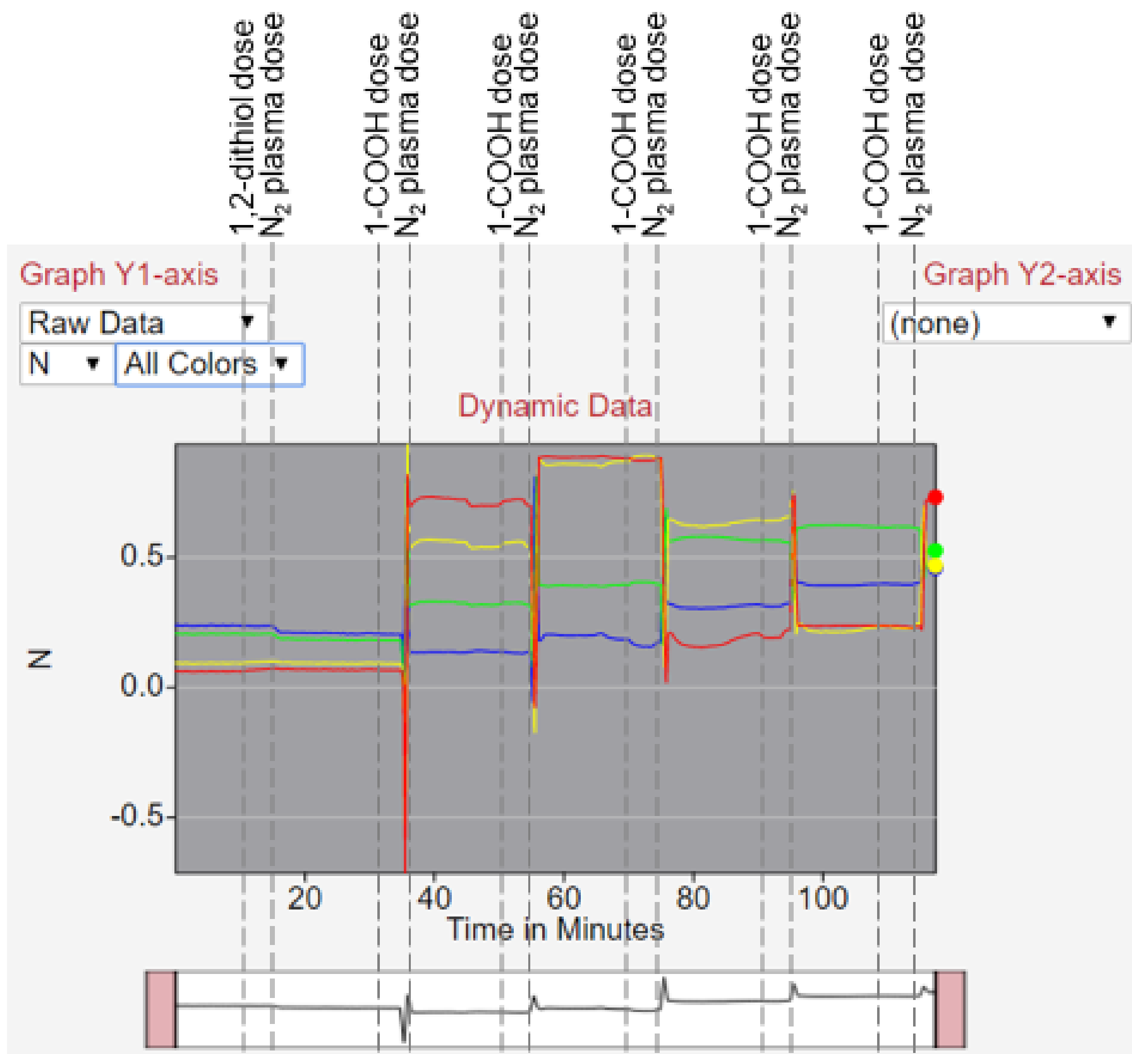

Figure 54. Raw in situ ellipsometry data for F006 multi-layer, multi-cycle growth.

Comparing the ellipsometry data from F003 and F006 it is interesting to note how the plasma acts differently when it has the 1,2-dithiol-o-carborane as the substrate as opposed to the 1-COOH-o-carborane dosed surface. In both the F003 and F006 growths, the plasma on the SAM surface does not create a large spike in the data like it does post-1-COOH-o-carborane. This could be the result of the plasma reacting differently to the different surface species. The change in the direction of growth—seen with the plasma produced in cycle 4—can be linked to possibly running out of the 1-COOH-o-carborane

during cycle 3. The rise in pressure in cycle 4 and 5 may have been a result of residual vapor coming from the 1-COOH-o-carborane ampoule plumbing.

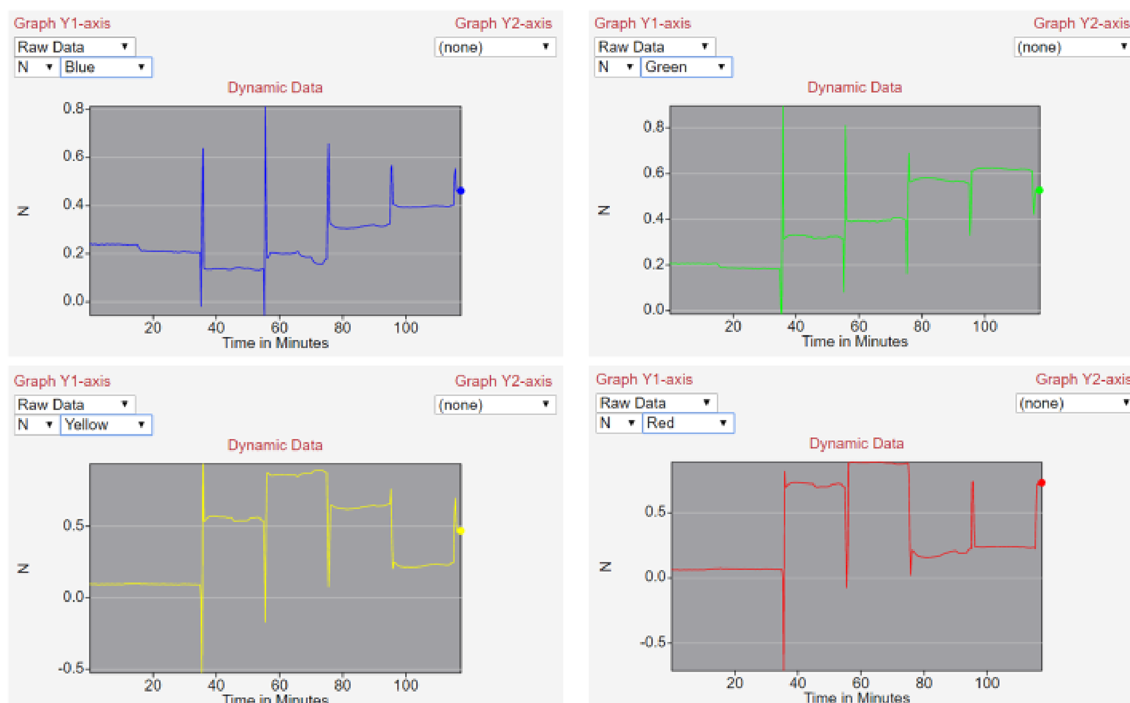

Figure 55. In situ ellipsometry raw data for F006 with wavelengths separated to allow easier viewing.

XPS characterization was performed on sample F006 (Figure 56), and the results are shown in Table 11. Hypothetically, for a five layer 1-COOH-o-carborane film with a seed layer of 1,2-dithiol-o-carborane, the B:N ratio should be about the same as that for a monolayer unless some of the nitrogen is lost along the way (or something else is happening). In sample F006, the B:N ratio ends up being 16.9 which is much higher than expected. Nitrogen should be retained between the precursor layers lowering the B:N ratio, so the lack of nitrogen after the multi-cycled growth is not as expected. For the B:C_B and B:O ratios there is no real differentiation between growths with and without the 1-COOH-o-carborane layer. Because surface contamination contributes significantly to

the values, they must be taken with a grain of salt. The $B:C_B$ ratio at 6.8 is about double the expected 3.3 and B:O ratio at 4.6 comes to about half the expected 10. However, multi-layer formation is suggested due to neither copper nor sulfur peaks being discernable for F006, indicating a thicker film.

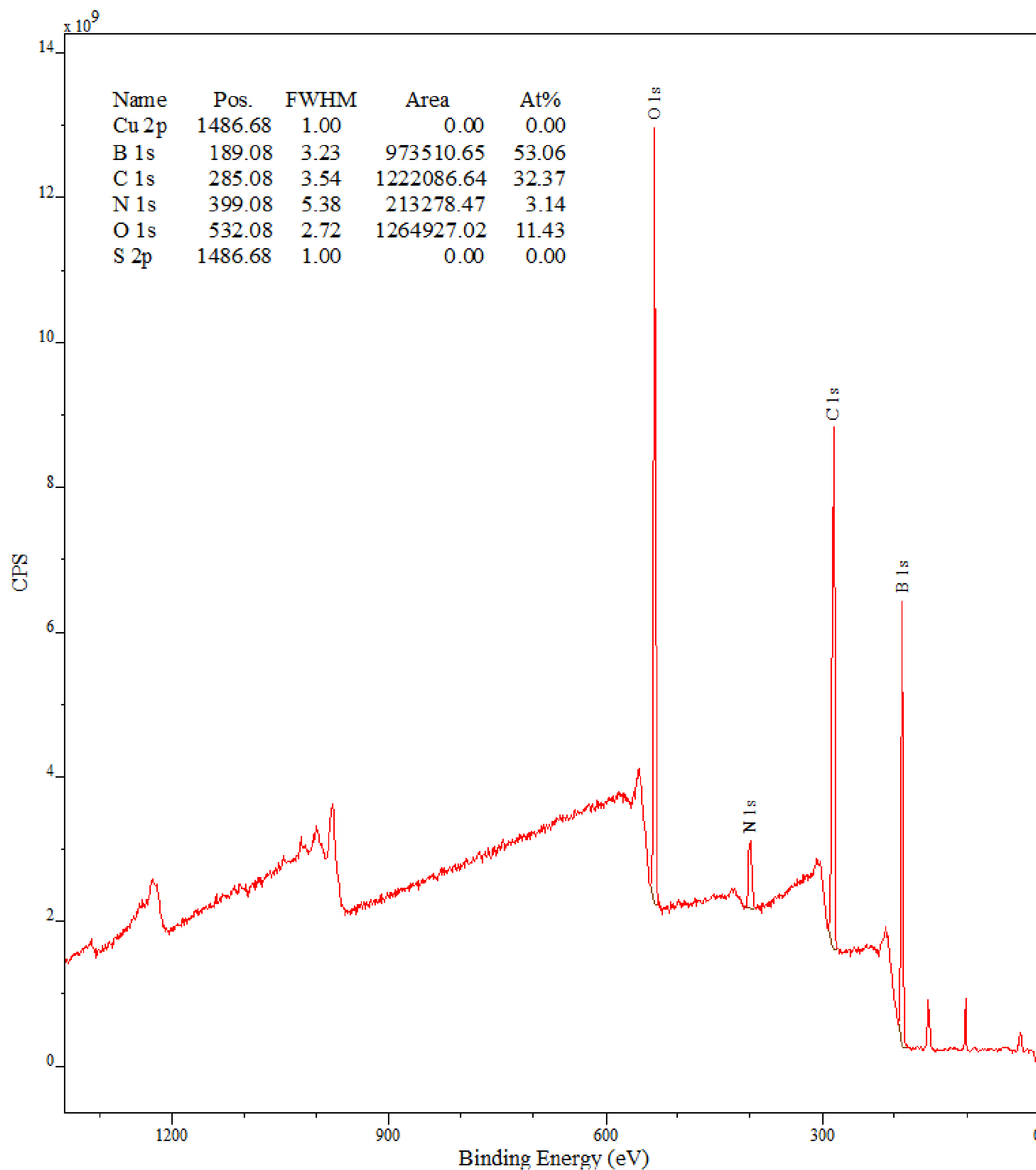

Figure 56. XPS characterization of sample F006 which had layers: copper, 1,2-dithiol-o-carborane and five PEMLD (plasma/1-COOH-o-carborane) cycles performed.

Table 11. XPS binding energy (eV), atomic percentages (%), and ratio of elements for sample A26, F003, and F006.

Sample	Cu	O	N	C	C_B	B	S	B/Cu	B/C_B	B/S
A26	932.9	531.8	399.3	284.9	286.3	189.3	162.8	-	-	-
	2.79	24.47	7.15	35.01	8.75	27.74	2.84	-	-	-
	1.0	8.8	2.6	12.6	3.2	10	1.0	10	3.1	10
F003	932.8	531.9	398.5	285.2	286.3	190.5	162.7	-	-	-
	1.64	18.23	17.57	33.73	6.07	26.81	2.03	-	-	-
	0.6	6.8	6.6	12.5	2.3	10	0.8	16.7	4.3	12.5
F006	932.9	531.8	399.3	285.1	286.3	189.3	162.8	-	-	-
	0.00	11.43	3.14	32.37	7.83	53.06	0.00	-	-	-
	0.0	2.2	0.6	6.1	1.5	10	0.0	-	6.7	-

Figure 57 shows the post-growth substrate with evident film growth on the substrate. The rings on the surface suggests the multi-layer, multi-cycle growths may have been successful, however, additional control studies would need to be performed to know for certain that film growth is the source of the rings.

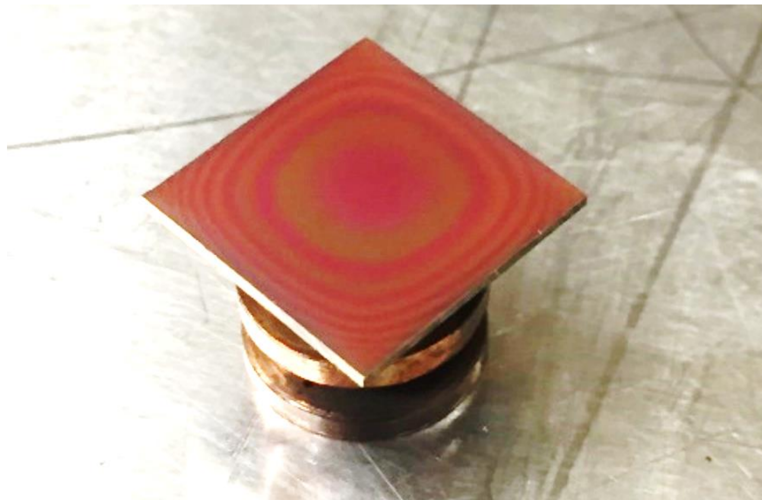

Figure 57. F006 sample post-growth showing evident film on substrate.

CHAPTER 4

CONCLUSION AND FUTURE WORK

With an increasing need for new materials and processes in the semiconductor industry, plasma-enhanced molecular layer deposition (PEMLD) of boron carbide films looks to fill the shortcomings of the currently used silicon-based materials. Boron carbide meets multiple requirements for interconnect integration including useful properties for a low-*k* dielectric, etch stop, metal diffusion barrier, hardmask, spacer layer, and a patterning assist layer. Looking for a way to achieve increasingly thinner films with the desired patterning characteristics and physical requirements, a novel deposition technique for carborane-based BC:H made by combining concepts from plasma-enhanced chemical vapor deposition and molecular layer deposition was developed in a home-built reactor chamber.

The home-built reactor chamber was designed to attach to an existing system which enabled *in situ* substrate layer deposition via thermal evaporation and post-deposition X-ray photoemission spectroscopy (XPS) characterization. The reactor chamber itself is capable of *in situ* spectroscopic ellipsometry which allowed the growth process of PEMLD films to be observed. Future work on the chamber would be the automated processing of film deposition. At the current state, films are only capable of being grown semi-automatically—valves and power are controlled manually.

Once in the reactor chamber, the samples were heated and exposed to a sublimated solid carborane precursor vapor. The first layer acted as a seed layer onto which additional layers could be grown using amide condensation. The first precursor layer deposition exploited thiol-metal chemistry through the reaction of thiol-carborane

precursors on copper substrates to form a self-assembled monolayers (SAMs). Using both 9-thiol-m-carborane and 1,2-dithiol-o-carborane, SAM assembly was observed and analyzed by means of *in situ* ellipsometry and *ex situ* contact angle and XPS analysis. Because possibly thicker-than-monolayer growths were observed for both precursors when exposed for longer times, more analysis of the copper substrate's condition prior to and post growth would be helpful in determining what is happening during the SAM formation step. This would include analysis of the surface roughness, contamination of the surface, and effect of varying exposure times more significantly. This surface analysis would allow us to know whether multiple layers were being formed or if the surface roughness was contributing to the apparent thicker-than-monolayer formation. Further testing to dial in the process parameters (exposure time, substrate temperature, pressure, etc.) with more characterization could also be helpful in finding a more reproducible SAM chemistry.

While utilizing amide condensation for the deposition of the subsequent PEMLD layers, plasma surface modification of the SAM was observed using a nitrogen plasma to create reactive species. Because the analysis of the plasma treated surface showed a distinct change from both the copper layer (in different stages of oxidation) and the SAM layer, it suggests successful surface modification/functionalization occurred. Further testing on the exact nature of the modification is needed to characterize the reactive sites on the film. This might include varying the plasma power, exposure time, more *in situ* XPS analysis, as well as different characterization techniques (e.g., Raman spectroscopy). Another interesting study might be to study the lifetime of the modification when exposed to an oxygen rich environment (rather than being stored in a nitrogen rich one).

Separately, adjusting the plasma parameters (power, pressure, dose, etc.) could allow for different reactive sites to be more or less likely than others.

The final step in the multi-layer, multi-cycle PEMLD scheme was introducing the second precursor/carboxylic acid for the amide condensation. In this work, 1-COOH-o-carborane was used as the second precursor. Although the amide condensation was not apparently in the ellipsometry data, a difference between the mono- and multi-layer growth atomic ratios via XPS characterization suggests growth of multiple layers. Interestingly, the plasma reacted differently whether the surface it was modifying was the 1,2-dithiol-o-carborane surface or surface after exposure to 1-COOH-o-carborane. Further testing and control studies will be needed to quantify the exact nature of the multi-layer, multi-cycle PEMLD films, but the reactor chamber is capable of producing multi-layer, multi-cycle PEMLD films.

REFERENCES

[1] G.E. Moore, *Cramming More Components onto Integrated Circuits (Reprinted from Electronics, Pg 114-117, April 19, 1965)*. Electronics **38**, 114 (1965). 10.1109/N-SSC.2006.4785860.

[2] J. Wu, Y.L. Shen, K. Reinhardt, H. Szu, and B. Dong, *A Nanotechnology Enhancement to Moore's Law*. Appl. Comput. Intell. Soft Comput. **2013**, 1 (2013). 10.1155/2013/426962.

[3] R.R. Schaller, *Moore's Law: Past, Present and Future*. IEEE Spectr. **34**, (1997). 10.1109/6.591665.

[4] K. Seshan, *Scaling and Its Implications for the Integration and Design of Thin Film Processes*. in *Handbook Thin Film Deposition.* (2012), pp. 19–40.

[5] S.W. King, *Dielectric Barrier, Etch Stop, and Metal Capping Materials for State of the Art and beyond Metal Interconnects*. ECS J. Solid State Sci. Technol. **4**, N3029 (2015). 10.1149/2.0051501jss.

[6] S.P. Murarka, *Multilevel Interconnections for ULSI and GSI Era*. Mater. Sci. Eng. R; Reports **19**, 87 (1997). 10.1016/S0927-796X(97)00002-8.

[7] S.P. Murarka, M. Eizenberg, and A.K. Sinha, *Interlayer Dielectrics for Semiconductor Technologies*. (Elsevier Inc., 2003).

[8] R.L. Opila and D.W. Hess, *A Century of Dielectric Science and Technology*. J. Electrochem. Soc. **150**, S1 (2003). 10.1149/1.1529671.

[9] K. Maex, M.R. Baklanov, D. Shamiryan, F. Lacopi, S.H. Brongersma, and Z.S. Yanovitskaya, *Low Dielectric Constant Materials for Microelectronics*. J. Appl. Phys. **93**, 8793 (2003). 10.1063/1.1567460.

[10] E. Altamirano-Sanchez, Z. Tao, A. Gunay-Demirkol, G. Lorusso, T. Hopf, J.L. Everaert, W. Clark, V. Constantoudis, F.S. Ou, and D. Sobieski, *Self-Aligned Quadruple Patterning to Meet Requirements for Fins with High Density*. SPIE 10 (2016). 10.1117/2.1201604.006378.

[11] R. Clark, K. Tapily, K. Yu, T. Hakamata, S. Consiglio, D.O. Meara, C. Wajda, J. Smith, and G. Leusink, *Perspective : New Process Technologies Required for Future Devices and Scaling Perspective*. APL Mater. **6**, (2018). 10.1063/1.5026805.

[12] ITRS, *International Technology Roadmap for Semiconductors*. in *ITRS* (2013), pp. 1–87.

[13] B.J. Nordell, T.D. Nguyen, C.L. Keck, S. Dhungana, A.N. Caruso, W.A. Lanford, J.T. Gaskins, P.E. Hopkins, D.R. Merrill, D.C. Johnson, L.L. Ross, P. Henry, S.W. King, and M.M. Paquette, *Conquering the Low-k Death Curve: Insulating Boron Carbide Dielectrics with Superior Mechanical Properties*. Adv. Electron. Mater. **2**, 1600073 (2016). 10.1002/aelm.201600073.

[14] D. Shamiryan, T. Abell, F. Iacopi, and K. Maex, *Low-k Dielectric Materials*. Mater. Today 34 (2004). 10.1016/S1369-7021(04)00053-7.

[15] B.J. Nordell, S. Karki, T.D. Nguyen, P. Rulis, A.N. Caruso, S.S. Purohit, H. Li, S.W. King, D. Dutta, D. Gidley, W.A. Lanford, and M.M. Paquette, *The Influence of Hydrogen on the Chemical, Mechanical, Optical/Electronic, and Electrical Transport Properties of Amorphous Hydrogenated Boron Carbide*. J. Appl. Phys. **118**, 035703 (2015). 10.1063/1.4927037.

[16] M.S.Driver, M.M.Paquette, S.King, B.J.Nordell, and A.N. Caruso, *The Electronic and Chemical Structure of the A-B3CO0.5:Hy-to-Metal Interface from Photoemission*

Spectroscopy: Implications for Schottky Barrier Heights. J. Phys. Condens. Matter **24**, 445001 (2012). 10.1088/0953-8984/24/44/445001.

[17] S. Dhungana, T.D. Nguyen, B.J. Nordell, A.N. Caruso, M.M. Paquette, G. Chollon, W.A. Lanford, K. Scharfenberger, D. Jacob, and S.W. King, *Boron and High-k Dielectrics: Possible Fourth Etch Stop Colors for Multipattern Optical Lithography Processing*. J. Vac. Sci. Technol. A Vacuum, Surfaces, Film. **35**, 021510 (2017). 10.1116/1.4974920.

[18] M.M. Paquette, B.J. Nordell, A.N. Caruso, M. Sato, H. Fujiwara, and S.W. King, *Optimization of Amorphous Semiconductors and Low-/High-k Dielectrics through Percolation and Topological Constraint Theory*. MRS Bull. **42**, 39 (2017). 10.1557/mrs.2016.297.

[19] B.J. Nordell, C.L. Keck, T.D. Nguyen, A.N. Caruso, S.S. Purohit, W.A. Lanford, D. Dutta, D. Gidley, P. Henry, S.W. King, and M.M. Paquette, *Tuning the Properties of a Complex Disordered Material: Full Factorial Investigation of PECVD-Grown Amorphous Hydrogenated Boron Carbide*. Mater. Chem. Phys. **173**, 268 (2016). 10.1016/j.matchemphys.2016.02.013.

[20] J.E. Proctor, V. Bhakhri, R. Hao, T.J. Prior, T. Scheler, E. Gregoryanz, M. Chhowalla, and F. Giulani, *Stabilization of Boron Carbide via Silicon Doping*. J. Phys. Condens. Matter **27**, 015401 (2015). 10.1088/0953-8984/27/1/015401.

[21] S. Aryal, P. Rulis, and W. Ching, *Mechanism for Amorphization of Boron Carbide B4C under Uniaxial Compression*. Phys. Rev. B **84**, 184112 (2011). 10.1103/PhysRevB.84.184112.

[22] M. Beauvy, *Stoichiometric Limits of Carbon-Rich Boron Carbide Phases*. J. Less-

Common Met. **90**, 169 (1983). 10.1016/0022-5088(83)90067-X.

[23] V. Domnich, S. Reynaud, R.A. Haber, and M. Chhowalla, *Boron Carbide: Structure, Properties, and Stability under Stress*. J. Am. Ceram. Soc. **94**, 3605 (2011). 10.1111/j.1551-2916.2011.04865.x.

[24] F. Thévenot, *Boron Carbide—A Comprehensive Review*. J. Eur. Ceram. Soc. **6**, 205 (1990). 10.1016/0955-2219(90)90048-K.

[25] Sunwoo Lee and P.A. Dowben, *The Properties of Boron Carbide/Silicon Heterojunction Diodes Fabricated by Plasma-Enhanced Chemical Vapor Deposition*. Appl. Phys. A **58**, 223 (1994). 10.1007/BF00324380.

[26] K.A. Schwetz and P. Karduck, *Investigations in the Boron-Carbon System with the Aid of Electron Probe Microanalysis*. 405 (1991). 10.1016/0022-5088(91)90345-5.

[27] M. Rosales, F. Camargo, and C.R.C. Lima, *Characterization of Boron Carbide Thermal Sprayed Coatings for High Wear Resistance Performance*. Proc. Int. Therm. Spray Conf. (2009). 10.1361/cp2009itsc1175.

[28] A. Bhatnagar, *Lightweight Ballistic Composites: Military and Law-Enforcement Applications*. 2nd ed. (Woodhead Publishing, 2016).

[29] J.E. Zorzi, C.A. Perottoni, and J.A.H. da Jornada, *Hardness and Wear Resistance of B4C Ceramics Prepared with Several Additives*. Mater. Lett. **59**, 2932 (2005). 10.1016/j.matlet.2005.04.047.

[30] I.M.A. Zaman, *Development of B_4C and MoS_2 Nanocoatings on Cutting Tools*. Development of B_4C and MoS_2 Nanocoatings on Cutting Tools, Oklahoma State University, 2000.

[31] E. Azizov, V. Barsuk, L. Begrambekov, O. Buzhinsky, A. Evsin, A. Gordeev, A.

Grunin, N. Klimov, V. Kurnaev, I. Mazul, V. Otroshchenko, A. Putric, Y. Sadovskiy, P. Shigin, S. Vergazov, and A. Zakharov, *Boron Carbide (B4C) Coating. Deposition and Testing*. J. Nucl. Mater. 1 (2015). 10.1016/j.jnucmat.2015.01.015.

[32] S. Veprek, S. Rambert, M. Heintze, F. Mattenberger, M. Jurcikrajman, W. Portmann, D. Ringer, and U. Stiefel, *Development of Plasma CVD and Feasibility Study of Boron Carbide In-Situ Coatings for Tokamaks*. J. Nucl. Mater. **162–164**, 724 (1989). 10.1016/0022-3115(89)90353-X.

[33] O. Postel and J. Heberlein, *Deposition of Boron Carbide Thin Film by Supersonic Plasma Jet CVD with Secondary Discharge*. Surf. Coatings Technol. **108–109**, 247 (1998). 10.1016/S0257-8972(98)00661-6.

[34] J. Oliveira, *Laser-Assisted CVD of Boron Carbide at Atmospheric Pressure*. Appl. Surf. Sci. **138–139**, 159 (1999). 10.1016/S0169-4332(98)00394-8.

[35] B. Zeng, Z. Feng, S. Li, Y. Liu, L. Cheng, and L. Zhang, *Microstructure and Deposition Mechanism of CVD Amorphous Boron Carbide Coatings Deposited on SiC Substrates at Low Temperature*. Ceram. Int. **35**, 1877 (2009). 10.1016/j.ceramint.2008.10.020.

[36] A.A. Ahmad, N.J. Ianno, P.G. Snyder, D. Welipitiya, D. Byun, and P.A. Dowben, *Optical Properties of Boron Carbide (B_5C) Thin Films Fabricated by Plasma-Enhanced Chemical-Vapor Deposition*. J. Appl. Phys. **79**, 8643 (1996). 10.1063/1.362487.

[37] A.O. Sezer and J.I. Brand, *Chemical Vapor Deposition of Boron Carbide*. Mater. Sci. Eng. B **79**, 191 (2001). 10.1016/S0921-5107(00)00538-9.

[38] D. Aher, *Mechanical Properties of PECVD Boron Carbide*. Mechanical Properties of PECVD Boron Carbide, University of Nebraska - Lincoln, 2011.

[39] S. Lee, J. Mazurowski, W.L. O'Brien, Q.Y. Dong, J.J. Jia, T.A. Callcott, Y. Tan, K.E. Miyano, D.L. Ederer, D.R. Mueller, and P.A. Dowben, *The Structural Homogeneity of Boron Carbide Thin Films Fabricated Plasma-Enhanced Chemical Vapor Deposition from* B_5H_9 *+*CH_4. J. Appl. Phys. **74**, 6919 (1993). .

[40] S. Lee, J. Mazurowski, G. Ramseyer, and P.A. Dowben, *Characterization of Boron Carbide Thin Films Fabricated by Plasma Enhanced Chemical Vapor Deposition from Boranes*. J. Appl. Phys. **72**, 4925 (1992). 10.1063/1.352060.

[41] D. Priyadarshini, S. Nguyen, H. Shobha, S. Cohen, T. Shaw, E. Liniger, C.K. Hu, C. Parks, E. Adams, J. Burnham, a. H. Simon, G. Bonilla, A. Grill, D. Canaperi, D. Edelstein, D. Collins, M. Balseanu, M. Stolfi, J. Ren, and K. Shah, *Advanced Metal and Dielectric Barrier Cap Films for Cu Low k Interconnects*. 2014 IEEE Int. Interconnect Technol. Conf. / Adv. Met. Conf. IITC/AMC 2014 185 (2014). 10.1109/IITC.2014.6831866.

[42] D.J. Michalak, J.M. Blackwell, J.M. Torres, A. Sengupta, L.E. Kreno, J.S. Clarke, and D. Pantuso, *Porosity Scaling Strategies for Low-k Films*. J. Mater. Res. **30**, 3363 (2015). 10.1557/jmr.2015.313.

[43] W. Zhou, S. Bailey, R. Sooryakumar, S. King, G. Xu, E. Mays, C. Ege, and J. Bielefeld, *Elastic Properties of Porous Low-k Dielectric Nano-Films*. J. Appl. Phys. **110**, 043520 (2011). 10.1063/1.3624583.

[44] M.T. Alam, R.A. Pulavarthy, J. Bielefeld, S.W. King, and M.A. Haque, *Thermal Conductivity Measurement of Low-k Dielectric Films: Effect of Porosity and Density*. J. Electron. Mater. **43**, 746 (2013). 10.1007/s11664-013-2949-5.

[45] T.A. Pomorski, B.C. Bittel, P.M. Lenahan, E. Mays, C. Ege, J. Bielefeld, D. Michalak,

and S.W. King, *Defect Structure and Electronic Properties of SiOC:H Films Used for Back End of Line Dielectrics*. J. Appl. Phys. **115**, 234508 (2014). 10.1063/1.4882023.

[46] S.W. King, D. Jacob, D. Vanleuven, B. Colvin, J. Kelly, M. French, J. Bielefeld, D. Dutta, M. Liu, and D. Gidley, *Film Property Requirements for Hermetic Low-k a-SiOxCyNz:H Dielectric Barriers*. ECS J. Solid State Sci. Technol. **1**, N115 (2012). 10.1149/2.021206jss.

[47] Y.L. Cheng, J. Wu, T.J. Chiu, S.A. Chen, and Y.L. Wang, *Comprehensive Comparison of Electrical and Reliability Characteristics of Various Copper Barrier Films*. J. Vac. Sci. Technol. B Microelectron. Nanom. Struct. **29**, 031207 (2011). 10.1116/1.3591340.

[48] B.J. Nordell, T.D. Nguyen, A.N. Caruso, S.S. Purohit, N.A. Oyler, W.A. Lanford, D.W. Gidley, J.T. Gaskins, P.E. Hopkins, P. Henry, S.W. King, and M.M. Paquette, *Carbon-Enriched Amorphous Hydrogenated Boron Carbide Films for Very-Low-k Interlayer Dielectrics*. Adv. Electron. Mater. **3**, 1700116 (2017). 10.1002/aelm.201700116.

[49] L.M. Han, Y. Xu, J.Z. Xie, M.S. Zhou, and S. Chooi, *Use of Boron Carbide as an Etch-Stop and Barrier Layer for Copper Dual Damascene Metallization*. US Patent 6,352,921 B1 (2002).

[50] L.A. Chow, *Equipment and Manufacturability Issues in CVD Processes*. in *Handbook Thin Film Deposition.* (Elsevier Inc., 2012), pp. 127–178.

[51] S. Fumio, *Semiconductor Silicon Crystal Technology*. (Elsevier Inc., 1989).

[52] J.D. Plummer, M. Deal, and P.D. Griffin, *Silicon VSLI Technology: Fundamentals, Practice and Modeling*. (Pearson Education Inc., 2009).

[53] H.B. Profijt, S.E. Potts, M.C.M. van de Sanden, and W.M.M. Kessels, *Plasma-Assisted*

Atomic Layer Deposition: Basics, Opportunities, and Challenges. J. Vac. Sci. Technol. A Vacuum, Surfaces, Film. **29**, 050801 (2011). 10.1116/1.3609974.

[54] R.W. Johnson, A. Hultqvist, and S.F. Bent, *A Brief Review of Atomic Layer Deposition: From Fundamentals to Applications*. Mater. Today **17**, 236 (2014). 10.1016/j.mattod.2014.04.026.

[55] J.J. Gooding and S. Ciampi, *The Molecular Level Modification of Surfaces: From Self-Assembled Monolayers to Complex Molecular Assemblies*. Chem. Soc. Rev. **40**, 2704 (2011). 10.1039/C0CS00139B.

[56] Y. Heights, *Design and Characterization of Materials and Processes for Area Selective Atomic Layer Deposition*. Design and Characterization of Materials and Processes for Area Selective Atomic Layer Deposition, Georgia Institute of Technology, 2006.

[57] H.B. Profijt, *Plasma-Surface Interaction in Plasma-Assisted Atomic Layer Deposition*. Plasma-Surface Interaction in Plasma-Assisted Atomic Layer Deposition, Eindhoven University of Technology, 2012.

[58] D.K. Aswal, S. Lenfant, D. Guerin, J. V. Yakhmi, and D. Vuillaume, *Self Assembled Monolayers on Silicon for Molecular Electronics*. Anal. Chim. Acta **568**, 84 (2006). 10.1016/j.aca.2005.10.027.

[59] R.L. Puurunen, *Surface Chemistry of Atomic Layer Deposition: A Case Study for the Trimethylaluminum/Water Process*. J. Appl. Phys. **97**, (2005). 10.1063/1.1940727.

[60] S.M. George, *Atomic Layer Deposition: An Overview*. Chem. Rev. **110**, 111 (2009). 10.1021/cr900056b.

[61] N.P. Dasgupta, X. Meng, J.W. Elam, and A.B.F. Martinson, *Atomic Layer Deposition of Metal Sulfide Materials*. Acc. Chem. Res. **48**, 341 (2015). 10.1021/ar500360d.

[62] X. Meng, *Atomic-Scale Surface Modifications and Novel Electrode Designs for High-Performance Sodium-Ion Batteries via Atomic Layer Deposition*. J. Mater. Chem. A **5**, 10127 (2017). 10.1039/C7TA02742G.

[63] H. Van Bui, F. Grillo, and J.R. Van Ommen, *Atomic and Molecular Layer Deposition: Off the Beaten Track*. Chem. Commun. **53**, 45 (2017). 10.1039/c6cc05568k.

[64] W.M.. Mackus, A.J.M., Bol, A.A., Kessels, *The Use of Atomic Layer Deposition in Advanced Nanopatterning*. Nanoscale **6**, 10941 (2014). 10.1039/b000000x.

[65] M. Leskelä and M. Ritala, *Atomic Layer Deposition (ALD): From Precursors to Thin Film Structures*. Thin Solid Films **409**, 138 (2002). 10.1016/S0040-6090(02)00117-7.

[66] A. Niskanen, *Radical Enhanced Atomic Layer Deposition of Metals and Oxides*. Radical Enhanced Atomic Layer Deposition of Metals and Oxides, University of Helsinki, 2006.

[67] P. Sundberg and M. Karppinen, *Organic and Inorganic-Organic Thin Film Structures by Molecular Layer Deposition: A Review*. Beilstein J. Nanotechnol. **5**, 1104 (2014). 10.3762/bjnano.5.123.

[68] X. Meng, *An Overview of Molecular Layer Deposition for Organic and Organic–inorganic Hybrid Materials: Mechanisms, Growth Characteristics, and Promising Applications*. J. Mater. Chem. A (2017). 10.1039/C7TA04449F.

[69] S.M. George, B. Yoon, and A.A. Dameron, *Surface Chemistry for Molecular Layer Deposition of Organic and Hybrid Organic - Inorganic Polymers*. Acc. Chem. Res. (2009). 10.1021/ar800105q.

[70] X. Meng, X. Wang, D. Geng, C. Ozgit-Akgun, N. Schneider, and J.W. Elam, *Atomic Layer Deposition for Nanomaterial Synthesis and Functionalization in Energy*

Technology. Mater. Horiz. **4**, 133 (2017). 10.1039/C6MH00521G.

[71] H. Kim, H.B.R. Lee, and W.J. Maeng, *Applications of Atomic Layer Deposition to Nanofabrication and Emerging Nanodevices*. Thin Solid Films **517**, 2563 (2009). 10.1016/j.tsf.2008.09.007.

[72] S.M. George, B.H. Lee, B. Yoon, A.I. Abdulagatov, and R.A. Hall, *Metalcones: Hybrid Organic–Inorganic Films Fabricated Using Atomic and Molecular Layer Deposition Techniques*. J. Nanosci. Nanotechnol. **11**, 7948 (2011). 10.1166/jnn.2011.5034.

[73] K. Gregorczyk and M. Knez, *Hybrid Nanomaterials through Molecular and Atomic Layer Deposition: Top down, Bottom up, and in-between Approaches to New Materials*. Prog. Mater. Sci. **75**, 1 (2016). 10.1016/j.pmatsci.2015.06.004.

[74] O. Nilsen, K.B. Klepper, H.O. Nielsen, and H. Fjellvag, *Deposition of Organic-Inorganic Hybrid Materials by Atomic Layer Deposition*. ECS Trans. **16**, 3 (2008). 10.1002/9780470661345.smc121.

[75] H. Zhou and S.F. Bent, *Fabrication of Organic Interfacial Layers by Molecular Layer Deposition: Present Status and Future Opportunities*. J. Vac. Sci. Technol. A Vacuum, Surfaces, Film. **31**, 040801 (2013). 10.1116/1.4804609.

[76] C. Ban and S.M. George, *Molecular Layer Deposition for Surface Modification of Lithium-Ion Battery Electrodes*. Adv. Mater. Interfaces **3**, 1 (2016). 10.1002/admi.201600762.

[77] B.H. Lee, B. Yoon, A.I. Abdulagatov, R.A. Hall, and S.M. George, *Growth and Properties of Hybrid Organic-Inorganic Metalcone Films Using Molecular Layer Deposition Techniques*. Adv. Funct. Mater. **23**, 532 (2013). 10.1002/adfm.201200370.

[78] D.M. King, X. Liang, and A.W. Weimer, *Functionalization of Fine Particles Using Atomic and Molecular Layer Deposition*. Powder Technol. **221**, 13 (2012). 10.1016/j.powtec.2011.12.020.

[79] A. Ohl, W. Besch, H. Steffen, R. Foest, M. Arens, and K. Wandel, *Surface Coating by Repeated Plasma-Assisted Grafting and Cross-Linking of Molecular Precursors*. Plasma Process. Polym. **6**, 425 (2009). 10.1002/ppap.200930006.

[80] J. Friedrich, *Mechanisms of Plasma Polymerization - Reviewed from a Chemical Point of View*. Plasma Process. Polym. **8**, 783 (2011). 10.1002/ppap.201100038.

[81] S.B.S. Heil and J.L. van Hemmen, *Deposition of TiN and HfO_2 in a Commercial 200mm Remote Plasma Atomic Layer Deposition Reactor*. J. Vac. Sci. Technol. A Vacuum, Surfaces, Film. **25**, (2007). 10.1116/1.2753846.

[82] B.H. Kim, W.S. Jeon, S.H. Jung, and B.T. Ahn, *Interstitial Oxygen Incorporation into Silicon Substrate during Plasma Enhanced Atomic Layer Deposition of Al2O3*. Electrochem. Solid-State Lett. **8**, G294 (2005). 10.1149/1.2035699.

[83] G. Dingemans, R. Seguin, P. Engelhart, M.C.M. van de Sanden, and W.M.M. Kessels, *Silicon Surface Passivation by Ultrathin Al2O3 Films Synthesized by Thermal and Plasma Atomic Layer Deposition*. Phys. Status Solidi - Rapid Res. Lett. **4**, 10 (2010). 10.1002/pssr.200903334.

[84] O.-K. Kwon, S.-H. Kwon, S.-W. Kang, and H.-S. Park, *Plasma-Enhanced Atomic Layer Deposition of Ruthenium Thin Films*. Electrochem. Solid-State Lett. **7**, C46 (2004). 10.1149/1.1648612.

[85] J.W. Lim and S.J. Yun, *Insulators with High Stability for Electroluminescent Devices*. Japanese J. Appl. Physics, Part 2 Lett. **42**, (2003). 10.1143/JJAP.42.L663.

[86] M.T. Seman, D.N. Richards, P. Rowlette, and C.A. Wolden, *An Analysis of the Deposition Mechanisms Involved during Self-Limiting Growth of Aluminum Oxide by Pulsed PECVD*. Chem. Vap. Depos. **14**, 296 (2008). 10.1002/cvde.200806701.

[87] C.W. Jeong, B. Il Lee, and S.K. Joo, *Growth and Characterization of Aluminum Oxide Films by Plasma-Assisted Atomic Layer Deposition*. Mater. Sci. Eng. C **16**, 59 (2001). 10.1016/S0928-4931(01)00299-5.

[88] J. Dendooven, D. Deduytsche, J. Musschoot, R.L. Vanmeirhaeghe, and C. Detavernier, *Conformality of Al_2O_3 and AlN Deposited by Plasma-Enhanced Atomic Layer Deposition*. J. Electrochem. Soc. **157**, G111 (2010). 10.1149/1.3301664.

[89] J.W. Lim, J.B. Koo, S.J. Yun, and H.T. Kim, *Characteristics of Pentacene Thin Film Transistor with Al_2O_3 Gate Dielectrics on Plastic Substrate*. Electrochem. Solid-State Lett. **10**, J136 (2007). 10.1149/1.2760321.

[90] S.B.S. Heil, J.L. Van Hemmen, M.C.M. Van De Sanden, and W.M.M. Kessels, *Reaction Mechanisms during Plasma-Assisted Atomic Layer Deposition of Metal Oxides: A Case Study for Al_2O_3*. J. Appl. Phys. **103**, (2008). 10.1063/1.2924406.

[91] J.W. Lim and S.J. Yun, *Electrical Properties of Alumina Films by Plasma-Enhanced Atomic Layer Deposition*. Electrochem. Solid-State Lett. **7**, F45 (2004). 10.1149/1.1756541.

[92] J.H. Lee, Y.J. Cho, Y.S. Min, D. Kim, and S.W. Rhee, *Plasma Enhanced Atomic Layer Deposition of $SrTiO_3$ Thin Films with $Sr(Tmhd)_2$ and $Ti(i\text{-}OPr)_4$*. J. Vac. Sci. Technol. A Vacuum, Surfaces, Film. **20**, 1828 (2002). 10.1116/1.1500745.

[93] O.M. Nayfeh, T. Marr, and M. Dubey, *Impact of Plasma-Assisted Atomic-Layer-Deposited Gate Dielectric on Graphene Transistors*. IEEE Electron Device Lett. **32**, 473

(2011). 10.1109/LED.2011.2108258.

[94] I. Volintiru, *Remote Plasma Deposition of Metal Oxides: Routes for Controlling the Film Growth*. Remote Plasma Deposition of Metal Oxides: Routes for Controlling the Film Growth, Eindhoven University of Technology, 200810.6100/IR631887.

[95] J.N. Hohman, P. Zhang, E.I. Morin, P. Han, M. Kim, A.R. Kurland, P.D. Mcclanahan, V.P. Balema, and P.S. Weiss, *Self-Assembly of Carboranethiol Isomers on Au{111}: Intermolecular Interactions Determined by Molecular Dipole Orientations*. ACS Nano **3**, 527 (2009). 10.1021/nn800673d.

[96] R. Foest, M. Schmidt, and H. Gargouri, *Self-Assembling and Self-Limiting Monolayer Deposition*. Eur. Phys. J. D **68**, (2014). 10.1140/epjd/e2013-40420-y.

[97] M.M. Sung, K. Sung, C.G. Kim, S.S. Lee, and Y. Kim, *Self-Assembled Monolayers of Alkanethiols on Oxidized Copper Surfaces*. J. Phys. Chem. B **104**, 2273 (2000). 10.1021/jp992995h.

[98] T. Baše, Z. Bastl, V. Havránek, J. Macháček, J. Langecker, and V. Malina, *Carboranedithiols: Building Blocks for Self-Assembled Monolayers on Copper Surfaces.* Langmuir **28**, 12518 (2012). 10.1021/la302334x.

[99] J. Bould, J. MacHáček, M.G.S. Londesborough, R. MacÍas, J.D. Kennedy, Z. Bastl, P. Rupper, and T. Baše, *Decaborane Thiols as Building Blocks for Self-Assembled Monolayers on Metal Surfaces*. Inorg. Chem. **51**, 1685 (2012). 10.1021/ic202000b.

[100] F.F. Chen, *Radiofrequency Plasma Sources for Semiconductor Processing*. in *Advanced Plasma Technology*, edited by R. D'Agostino, P. Favia, Y. Kawai, H. Ikegami, N. Sato, and F. Aref-Khonsari (Wiley-VCH, 2008), pp. 99–114.

[101] M.R. Baklanov, J.F. de Marneffe, D. Shamiryan, A.M. Urbanowicz, H. Shi, T. V.

Rakhimova, H. Huang, and P.S. Ho, *Plasma Processing of Low-k Dielectrics*. J. Appl. Phys. **113**, 041101 (2013). 10.1063/1.4765297.

[102] M. Leskelä, J. Niinistö, and M. Ritala, *Atomic Layer Deposition*. in *Comprehensive Material Processing*, edited by S. Hashmi (Elsevier, 2014), pp. 101–123.

[103] H. Zhou and S.F. Bent, *Molecular Layer Deposition of Functional Thin Films for Advanced Lithographic Patterning*. ACS Appl. Mater. Interfaces **3**, 505 (2011). 10.1021/am1010805.

[104] E. Langereis, S.B.S. Heil, M.C.M. Van De Sanden, and W.M.M. Kessels, *In Situ Spectroscopic Ellipsometry Study on the Growth of Ultrathin TiN Films by Plasma-Assisted Atomic Layer Deposition*. J. Appl. Phys. **100**, (2006). 10.1063/1.2214438.

[105] L. Lamagna, *Atomic Layer Deposition and Characterization of Rare Earth Oxides for Innovation in Microelectronics*. Atomic Layer Deposition and Characterization of Rare Earth Oxides for Innovation in Microelectronics, Università degli Studi di Milano-Bicocca, 2009.

[106] W. Chiappim, G.E. Testoni, A.C.O.C. Doria, R.S. Pessoa, M.A. Fraga, N.K.A.M. Galvão, K.G. Grigorov, L. Vieira, and H.S. Maciel, *Relationships among Growth Mechanism, Structure and Morphology of PEALD TiO_2 Films: The Influence of O_2 Plasma Power, Precursor Chemistry and Plasma Exposure Mode*. Nanotechnology **27**, 305701 (2016). 10.1088/0957-4484/27/30/305701.

[107] E. Langereis, *Plasma-Assisted Atomic Layer Deposition an in Situ Diagnostic Study*. Plasma-Assisted Atomic Layer Deposition an in Situ Diagnostic Study, Eindhoven University of Technology, 2008.

[108] R.A. Ovanesyan, N. Leick, K.M. Kelchner, D.M. Hausmann, and S. Agarwal, *Atomic*

Layer Deposition of SiC_xN_y Using Si_2Cl_6 and CH_3NH_2 Plasma. Chem. Mater. (2017). 10.1021/acs.chemmater.7b01358.

[109] M. Baklanov, M. Green, and K. Maex, *Dielectric Films for Advanced Microelectronics*. (John Wiley & Sons, Ltd, West Sussex, United Kingdom, 2007).

[110] N. Hornsveld, B. Put, W.M.M. Kessels, P.M. Vereecken, and M. Creatore, *Plasma-Assisted and Thermal Atomic Layer Deposition of Electrochemically Active Li2CO3*. RSC Adv. **7**, 41359 (2017). 10.1039/C7RA07722J.

[111] Film Sense LLC, *FS-1 In Situ Mounting : Description and Specifications*. FS-1 In Situ Mounting : Description and Specifications, 2015.

[112] J.D. H. Keller, P. Simak, W. Schrepp, *Surface Chemistry of Thiols on Copper: An Efficient Way of Producing Multilayers*. Thin Solid Films **244**, 799 (1994). 10.1016/0040-6090(94)90574-6.

[113] H. Ron, H. Cohen, S. Matlis, M. Rappaport, and I. Rubinstein, *Self-Assembled Monolayers on Oxidized Metals. 4. Superior n-Alkanethiol Monolayers on Copper*. J. Phys. Chem. B **102**, 9861 (1998). 10.1021/jp9827072.

[114] J.C. Love, L.A. Estroff, J.K. Kriebel, R.G. Nuzzo, and G.M. Whitesides, *Self-Assembled Monolayers of Thiolates on Metals as a Form of Nanotechnology.* (2005)10.1021/cr0300789.

[115] A. Yavuz, N. Sohrabnia, A. Yilmaz, and M.F. Danışman, *Mixed Carboranethiol Self-Assembled Monolayers on Gold Surfaces*. Appl. Surf. Sci. **413**, 233 (2017). 10.1016/j.apsusc.2017.03.294.

[116] M. El-Desawy, *Characterization and Application of Aromatic Self-Assembled Monolayers*. Characterization and Application of Aromatic Self-Assembled Monolayers,

University of Bielefeld, 2007.

[117] T. Base, Z. Bastl, Z. Plzak, T. Grygar, J. Plesek, M.J. Carr, V. Malina, J. Subrt, J. Bohacek, E. Vecernikova, and O. Kriz, *Carboranethiol-Modified Gold Surface. A Study and Comparison of Modified Cluster and Flat Surfaces*. Langmuir **21**, 7776 (2005). 10.1021/la051122d.

[118] T. Baše, Z. Bastl, V. Havránek, K. Lang, J. Bould, M.G.S. Londesborough, J. Macháček, and J. Plešek, *Carborane–thiol–silver Interactions. A Comparative Study of the Molecular Protection of Silver Surfaces*. Surf. Coatings Technol. **204**, 2639 (2010). 10.1016/j.surfcoat.2010.02.019.

VITA

Lauren Mikal Dorsett was born on April 23, 1990, in Lubbock, Texas. She was educated K-9 at All Saints Episcopal School where she rebelled against the church and refused to wear panty hose with her dress uniform. After the ninth grade, she attended Lubbock High School where she was captain of the women's soccer team and graduated with honors in 2008.

Upon high school graduation, Ms. Dorsett attended Austin College in Sherman, Texas where she received the Dean's scholarship. She graduated in Spring 2012 with a Bachelor of Arts in Physics.

Ms. Dorsett moved to St. Louis, Missouri where she began taking coursework in mechanical engineering, however did not receive a degree after dropping out for personal reasons. Between 2012 and 2014, she found herself floundering in life, doing odd jobs such as being an assistant manager at an oil change establishment. In 2014, Lauren married and moved to Austin, Texas. In Texas, her wife would push her towards pursuing a higher degree in physics.

In Fall 2015, Ms. Dorsett started graduate school pursuing her master's degree in material physics at Texas State University. At Texas State, she took courses and worked in a nanofabrication clean lab, but due to spousal- then self-relocation- she transferred to the University of Missouri-Kansas City. At UMKC, Lauren was a graduate teaching assistant and worked for the Caruso-Paquette Research Group as a graduate research assistant. Upon completion of her degree requirements, she plans to pursue a career in industry. Ms. Dorsett is a member of the Material Research Society and the Society of Physics Students. Ms. Dorsett hopes to one day live in a society free of discrimination

based on the color of one’s skin, gender, sexual orientation and mental or physical

capabilities.